CATALYTIC ACTIVITY OF PHYSICALLY DEPOSITED METAL CLUSTERS AND THEIR ATOMIC STRUCTURE STUDY

by

RONGSHENG CAI

蔡 鎔 声

A thesis submitted to the University of Birmingham for the Degree of

DOCTOR OF PHILOSOPHY

Nanoscale Physics Research Laboratory
School of Physics and Astronomy
The University of Birmingham
April 2019

UNIVERSITY OF
BIRMINGHAM

University of Birmingham Research Archive

e-theses repository

This unpublished thesis/dissertation is copyright of the author and/or third parties. The intellectual property rights of the author or third parties in respect of this work are as defined by The Copyright Designs and Patents Act 1988 or as modified by any successor legislation.

Any use made of information contained in this thesis/dissertation must be in accordance with that legislation and must be properly acknowledged. Further distribution or reproduction in any format is prohibited without the permission of the copyright holder.

Abstract

The deposition of preformed clusters onto suitable support materials represents a new technique for the precision synthesis of heterogeneous catalysts. Benefitting from the successful scale-up of the cluster production, this thesis directly explores the catalytic performance of physically produced metal clusters for liquid-phase and vapour-phase model reactions, particularly under realistic conditions. The catalyst powders used in the experiments were produced using two kinds of cluster beam sources: a magnetron sputtering gas condensation cluster source and a matrix assembly cluster source (MACS). The cluster atomic structure, chemical composition and size evolution due to the reaction were characterized by aberration-corrected scanning transmission electron microscopy (STEM), coupled with energy dispersive X-ray spectroscopy (EDS), and correlated with the cluster chemical activities.

In the first part, Au/Cu binary clusters with variable controlled composition were deposited onto magnesium oxide supports using a magnetron sputtering gas condensation cluster source. It was found that Au/Cu cluster catalysts are highly active for the liquid-phase 4-nitrophenol reduction. Electron microscopy revealed that the Au/Cu clusters produced have an alloy structure, which results in a random distribution of Au and Cu atoms on the cluster surface. Combined with theoretical calculations of the binding energies, the interplay between Au and Cu atoms at the cluster surface, resulting in an enhanced catalytic activity, is proposed.

In the second part, we demonstrated the catalyst preparation with a new type of cluster beam source, MACS. Pd nanoclusters were deposited onto diced carbon tape supports and used for catalyzing vapour-phase selective 1-pentyne hydrogenation. The catalysis results showed that the Pd cluster catalyst from MACS is more active (per unit weight) than the Pd reference sample synthesized by traditional wet impregnation. Cluster size evolution before and after reaction suggested that the superior activity derived from the smaller cluster size and better stability against sintering compared to the Pd reference sample. In addition, no synergetic effect was found in Pd/Au clusters. The observed similar cluster activity (per surface atom) for Pd and Pd/Au cluster catalysts may be due to the oxidation in air, which could drive Pd atoms to the cluster surface, thus leading to a Pd cluster surface as pure Pd clusters.

Finally, a new method to prepare metal colloids from the cluster beam technique is introduced, in which metal clusters made using MACS were directly deposited onto soluble polymer films, followed by dissolving the polymer films in suitable solvents. The Pd colloids produced were also used to catalyze the reduction of 4-nitrophenol to demonstrate the catalytic performance. Only a small activity was observed which was attributed to the protecting polymers blocking a high fraction of the active sites on the cluster surface.

Acknowledgements

First, I would like to thank the European Commission who financially supported this work without national boundaries. I thank Prof. Richard Palmer for giving me this opportunity to work in NPRL group and build relationships with all the members. His wisdom, ideas, inspiration and encouragement have guided me to complete this project. Many thanks should also go to Dr. Wolfgang Theis for the supervision during the thesis writing up stage. He devoted much time to the corrections and provided many valuable comments on the thesis. Without his help, I could not finish in time.

I would like to express my special thanks to Dr. Jinlong Yin (Teer Coatings Ltd, TC), Dr. Peter Ellis (Johnson Matthey Technology Center, JM), Mr. Christopher Brown (JM) and Dr. Laura Ashfield (JM) who took care of me during my secondments to the JM/TC and provided so much kind help in sample preparation, characterization and paper drafting.

I thank many students and postdocs in the group, notably Dr. Lu Cao, Dr. William Terry, Dr. Vitor Oiko and Dr. Shane Murphy, who directly or indirectly contributed to my work through experimental guidance, sharing ideas and paper discussions/corrections. I also appreciate all the members in the group, past and present, for invaluable friendship and support.

Last but not the least, I would like to thank my wife and my parents for the unconditional love, support and encouragement. They give me the power to overcome all difficulties and march forward!

Author's publications

1. **Rongsheng Cai**, Peter R. Ellis, Jinlong Yin, Jian Liu, Christopher M. Brown, Ross Griffin, Guojing Chang, Dongjiang Yang, Jun Ren, Kevin Cooke, Peter T. Bishop, Wolfgang Theis, Richard E. Palmer, Performance of Preformed Au/Cu Nanoclusters Deposited on MgO Powders in the Catalytic Reduction of 4-Nitrophenol in Solution, *Small*, 2018, 14, 1703734.

2. **Rongsheng Cai**, Nan Jian, Shane Murphy, Karl Bauer, and Richard E. Palmer, A new method to prepare colloids of size-controlled clusters from a matrix assembly cluster source, *APL Materials*, 2017, 5, 053405.

3. Richard E. Palmer, **Rongsheng Cai**, Jerome Vernieres, Synthesis without solvents: the cluster (nanoparticle) beam route to catalysts and sensors, *Accounts of Chemical Research*, 2018, 51, 2296-2304.

4. Jin Sun, Dongjiang Yang, Cuihua Sun, Long Liu, Shuanglei Yang, Yi(Alec) Jia, **Rongsheng Cai**, and Xiangdong Yao, Potassium Niobate Nanolamina: A Promising Adsorbent for Entrapment of Radioactive Cations from Water, *Scientific Reports*, 2014, 4, 7313.

5. Peng Liang, Lin Zhang, Xiaoliang Zhao, Jianjiang Li, Long Liu, **Rongsheng Cai**, Dongjiang Yang, and Ahmad Umar, Synthesis of $ZnFe_2O_4/TiO_2$ Composite Nanofibers with Enhanced Photoelectrochemical Activity, *Science of Advanced Materials*, 2015, 7, 295-300.

6. Lichao Gao, Shuai Chen, **Rongsheng Cai**, Quansheng Zhao, Xiaoliang Zhao, Dongjiang Yang, DUT-58 (Co) Derived Synthesis of Co Clusters as Efficient Oxygen Reduction Electrocatalyst for Zinc–Air Battery, *Global Challenges*, 2018, 2, 1700086.

7. Yanhua Ding, Bing Liu, **Rongsheng Cai**, Tuo Xin, Chen Li, Linhua Xia and Yiqian Wang, One-Pot Synthesis of α-Fe_2O_3 Nanospindles as High-Performance Lithium-Ion Battery Anodes, *NANO: Brief Reports and Reviews*, 2018, 13, 1850018.

8. Yihui Zou, Guojing Chang, Yi (Alec) Jia, **Rongsheng Cai**, Shuai Chen, Yanzhi Xia, Wolfgang Theis, Dongjiang Yang and Xiangdong Yao, Generating Lithium Vacancies through Delithiation of $Li(Ni_xCo_yMn_z)O_2$ towards Bifunctional Electrocatalysts for Rechargeable Zinc-air Batteries, *Energy Storage Materials*, 2018, 15, 202-208.

9. Junyuan Xu, Shane Murphy, Dehua Xiong, **Rongsheng Cai**, Xian-Kui Wei, Marc Heggen, Emanuele Barborini, Simone Vinati, Rafal E. Dunin-Borkowski, Richard E. Palmer, Lifeng Liu, Cluster Beam Deposition of Ultrafine Cobalt and Ruthenium Clusters for Efficient and Stable Oxygen Evolution Reaction, *ACS Applied Energy Materials*, 2018, 1, 3013-3018.

10. Lijie Zhang, Tongchao Liu, Ning Chen, Yi Jia, **Rongsheng Cai**, Wolfgang Theis, Xianfeng Yang, Yanzhi Xia, Dongjiang Yang and Xiangdong Yao, Scalable and Controllable Synthesis of Atomic Metal Electrocatalysts Assisted by Egg-Box in Alginate, *Journal of Materials Chemistry A*, 2018, 6, 18417-18425.

Table of Contents

CHAPTER 1

An Introduction to Cluster Science and Catalysis

This thesis studies the catalytic properties of physically produced metal clusters supported on high-surface area materials for liquid-phase and vapour-phase catalytic reactions, particularly under realistic conditions. Different techniques including high angle annular dark field (HAADF)-Scanning Transmission Electron Microscopy (STEM) were employed to investigate their atomic structures, which are linked with their catalytic performances. In this chapter, the background of this research is reviewed from the discovery of clusters with magic numbers, physical and chemical preparation methods of metal clusters, characterization techniques and progress in catalysis by physically produced clusters.

1.1 Introduction to cluster science

1.1.1 Clusters, bridge between atoms and bulk materials

Clusters are aggregates of atoms or molecules ranging from 2 or 3 to $\sim 10^7$, whose remarkable physical and chemical properties change with the number of atoms or molecules they contain. Their dimensions lie in the range of between several Angstroms to one thousand of Angstroms, which are difficult to describe either using inorganic molecules or small pieces of bulk materials. Moreover, their physical/chemical properties dramatically differ from those of individual atoms and bulk solids or liquids, and cannot be obtained simply from extending the properties of the latter two kinds of materials. Clusters can be considered as a new intermediate state of matter between atoms/molecules and macro bulk materials.[1-2]

In general, there are three central topics in cluster science. The first one is the investigation of the cluster structure evolution in the cluster formation process. For example, both experimental and theoretical studies have proven the common existence of the clusters with structures like decahedron or icosahedron during the cluster formation process.[3-6] However, these structures are five-fold symmetric and cannot form long-range ordered structures, which means that at some point, in the formation process, a structure transformation from five-fold symmetric structure to six-fold symmetric structure (face-centered cubic or hexagonal close-packed structures, the most common structures in the bulk crystal) happens. The second one is exploring the formation and evolution of the clusters' electronic structure. As we know, the electronic structure for single atoms is discrete. But with increasing number of atoms in clusters, the discrete energy levels combine to form energy bands and sometimes band gaps (energy gaps between highest occupied molecular orbital and lowest unoccupied molecular orbital). It is important to find when the transition happens and how the electronic structure evolves. The third topic is studying the critical cluster size after which cluster exhibits similar properties to bulk materials. For the small clusters, adding each atom to a cluster can cause changes in structure (re-construction), whereas for the larger clusters, the added atom only tends to lead to surface relaxation, which cannot change the structure of the whole system, so the cluster properties are not dramatically affected. Finding the critical cluster sizes for different materials and for different properties are crucial for developing their applications. On the basis of these three basic topics, cluster science builds a bridge between atoms and bulk materials and has become a multidisciplinary branch of science involving physics, chemistry and so on.

1.1.2 Magic numbers of clusters

Cluster science as an individual branch of science was born in the discovery of clusters showing magic numbers in the early 1980's.[7] Before that, clusters were simply reckoned to be small molecules, which were not expected to exhibit any size dependent properties. However, this attitude was dramatically changed when Knight's group found that sodium (Na) clusters produced in a supersonic seeded cluster source are prone to form clusters with several specific sizes as shown in the abundance spectra in **Figure 1.1**.[7] After repeating the experiment at different conditions, they recognized that the clusters conspicuously abundant in the mass spectra are more stable than those of other sizes. This is believed to be the first size-dependent property observed from clusters. Now we know that this phenomenon can be explained by the cluster electronic shell structure that clusters of these peak sizes possess a closed electronic shell and are much more stable than those with open electronic shells. The clusters showing abundance in the mass spectra are known as "magic number" clusters.

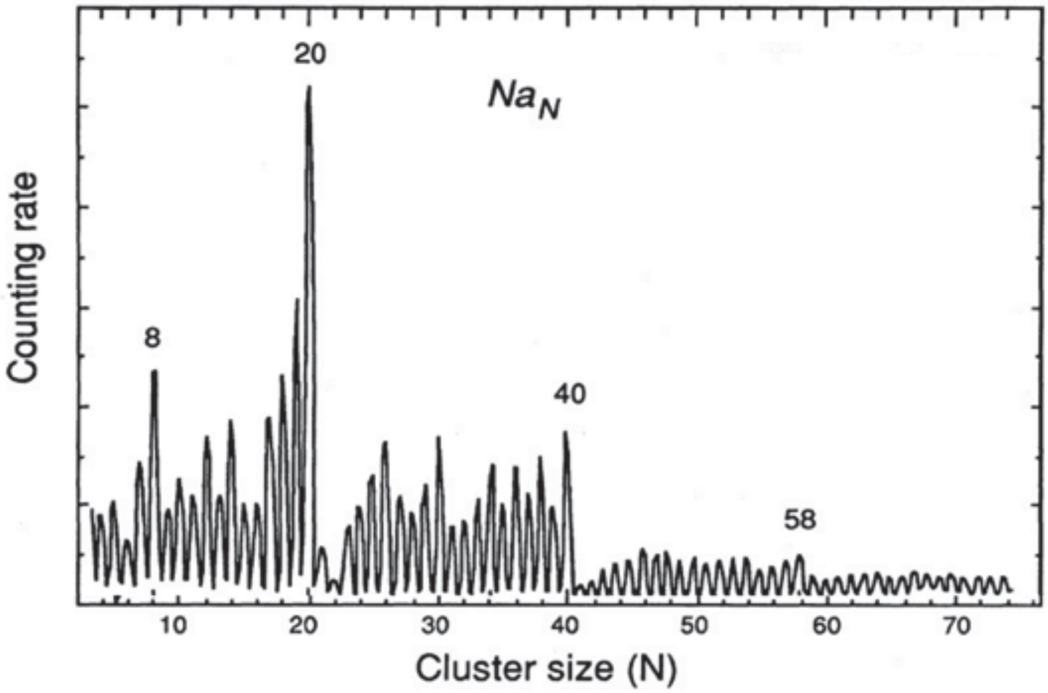

Figure 1.1 Mass spectrum of Na clusters produced in a supersonic seeded cluster source.[7] The peaks at sizes of 8, 20, 40 and 58 correspond to the magic numbers of Na clusters.

After those early studies, extensive investigations were conducted on IA metals (alkali metals), such as sodium (Na) and potassium (K).[8-9] Their magic numbers have been repeatedly and separately confirmed to be the same at 8, 20, 40, 58, although the effect is less prominent in K clusters. Besides alkali metals, this phenomenon was also observed from the clusters of IB metals such as silver (Ag)[10] and copper (Cu),[11] which are produced by a different technique. Their magic numbers are slightly different from those of alkali metals. For example, in Cu clusters produced in a sputtering source, the magic numbers are found to be 9, 21, 41 and 57[12] as shown in **Figure 1.2**. The shift in the magic numbers from even to odd is because the produced Cu clusters carry one positive charge. In general, the magic numbers for IB metals are the same as IA metals since all of them have one valence electron. In contrast, the clusters of divalent metals (such as IIB group) show different magic numbers in their mass spectra. For example, both zinc (Zn) and cadmium (Ca) clusters have magic numbers at 4, 9, 10, 17, 20, 29, 34, 35, 46, 53, 56, 69..., which is believed to be due to two valence electrons contributing to the cluster electronic shell.[12-13] As for the elements of other groups, they also have their own specific magic numbers.

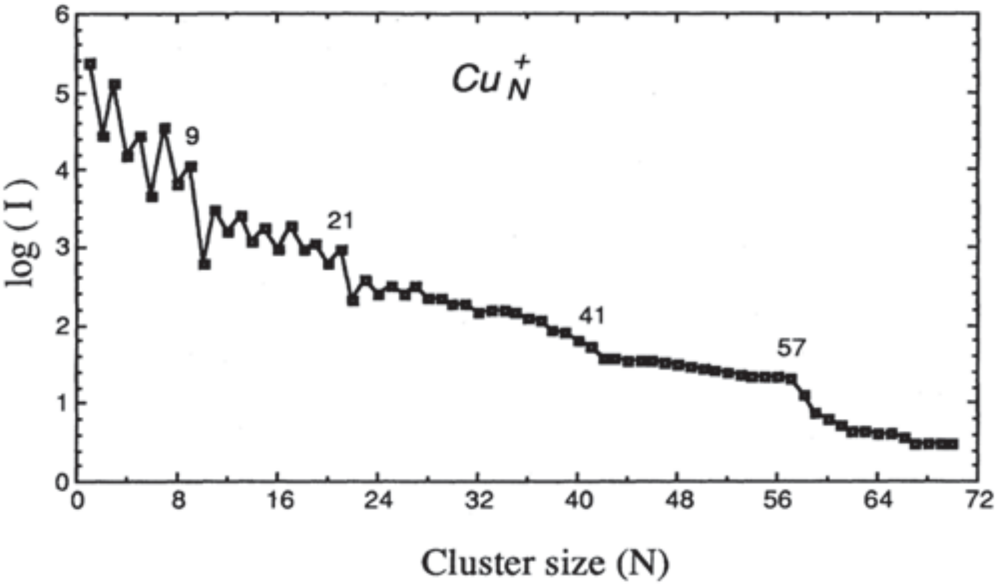

Figure 1.2 Mass spectra of the Cu clusters produced in a sputtering cluster source with the magic numbers of 9, 21, 41 and 57.[12]

Experimental studies disclose that clusters showing magic numbers can occur in a wide range of materials from IA group metals to inert gases.[14-15] To understand these "magic clusters", different theories and models have been proposed. Among them, electronic shell structure[7] and geometric shell structure[16-17] are two classical theories which successfully explain the cluster magic numbers for small clusters and larger clusters, respectively. In the following part, the origin of magic numbers will be introduced from these two aspects.

1.1.2.1 Electronic shell structure

Since similar magic numbers are observed in clusters of materials from the same groups, it is reasonable to associate this phenomenon with the electronic structure of atoms, which could influence the cluster stability during the formation process and thus affect their abundance in the mass spectra. The most famous and simplest model is the self-consistent jellium model,[18-19] which has successfully explained the main features in the cluster abundance spectra. In this model, a cluster is treated as one single atom, and all the valence electrons are successively filled in the shell which can be described by the radial quantum number n and the angular momentum l. It is well known that the atoms with a closed electron shell are stable or inert. So similarly, the clusters with the right number of electrons to complete a shell structure are also stable. Taking the alkali metal as an example, each atom contributes one valence electron to the whole cluster. When a cluster has the right number of electrons to form a closed electron shell, the cluster is stable and usually exhibits a prominent peak in the mass spectra. After adding another atom to the cluster, the extra valence electron will be filled in an orbit with higher energy. As a result, the stability of the whole cluster decreases. The reduced stability results in a reduced abundance, which explains the abundance peak drops after each magic number.

However, the obvious disadvantage of the self-consistent jellium model is that the model is only suitable for the spherical clusters, where the valence electrons are strongly delocalized. But according to the Jahn-Teller effect,[20] clusters with an open electron shell are prone to form ellipsoidal shape, which suggests this model cannot explain the fine features between magic numbers. Considering the distortion occurs in the clusters with open shell structure, Nilsson proposed a shell model for deformed "nuclei" based on an axially-deformed potential[21] and Clemenger further developed Nilsson's model to small axially-deformed clusters.[22] The Clemenger-Nilsson model has been frequently used in metal clusters and can reproduce the overall structures of the cluster abundance spectra. **Figure 1.3** shows the theoretical comparison between self-consistent jellium model and Clemenger-Nilsson model in predicting cluster abundance spectra.

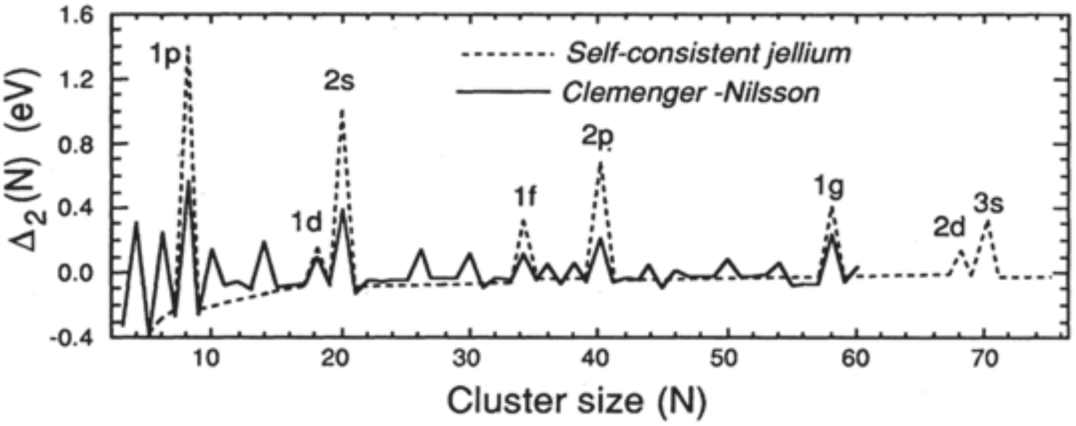

Figure 1.3 Comparison between self-jellium model and Clemenger-Nilsson mode in predicting cluster abundance spectra.[12] The fine structures between magic numbers can also been predicted by Clemenger-Nilsson mode.

1.1.2.2 Geometric shell structure

The electronic shell structure can explain the cluster abundance in the mass spectrum for small clusters. However, later studies[23] find that this effect becomes less important for the larger clusters since the energy steps of the electronic shell diminish as the cluster size increases. Instead, the cluster stability is dominated by the geometric shell effect of completing a geometric shell. An example of the mass spectra for Na clusters produced in a gas aggregation cluster source with the cluster size up to 25000 is shown in **Figure 1.4**.[23] The electronic shell effect dominates for small clusters up to 1500 atoms per cluster, which results in the magic numbers of 340, 440, 560, 700, 840, 1040, 1220 and 1430. However, in addition to these electronic magic numbers, another series of numbers for larger clusters, 1980, 2820, 5070 and 6550, continued until 21300 from other spectra, are also observed. These numbers are found to follow the equation below:

$$N=\frac{1}{3}(10K^3-15K^2+11K-3) \tag{1.1}$$

which is used to determine the number of atoms in a Mackay icosahedron with K shells. Similar geometric magic numbers have also been reported in magnesium (Mg) clusters.[24] To explain this phenomenon, a number of speculations have been proposed. Martin et al.[25] suggested the atoms in a small cluster tend to be mobile due to the lower melting point of smaller clusters. So, these atoms could form a spherical droplet as suggested in the jellium model which will show the electronic shell structure. The large clusters, by contrast, are more likely to form a crystalline structure. Their stability will be dominated by the shape of the crystallite (geometric shell structure). The evidence of the transition from geometric shell structure to electronic shell structure has been observed in Na clusters,[26] where the geometric shell structure melts down as the temperature increases and eventually vanishes from the mass spectra when the temperature reaches 34°C. Similar transition behavior was also observed in aluminum (Al) clusters.[27]

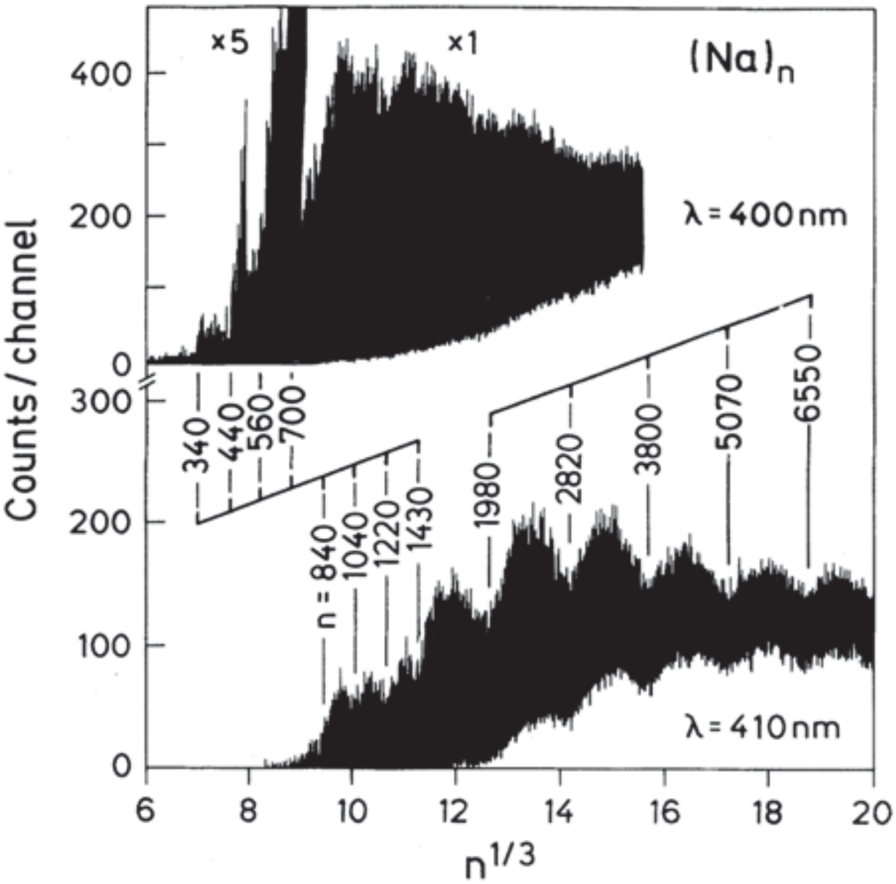

Figure 1.4 Mass spectra of Na clusters produced in a gas aggregation cluster source.[23] In addition to the magic numbers from the electric shell structure, a series of geometric magic numbers are also observed for larger clusters. In the measurement, clusters are ionized by a light with a wavelength of λ. Clusters with a complete geometric shell structure or electric shell structure are stable (difficult to ionize), which will show an evident trough in the spectra.

1.2 How to make clusters

Traditionally, there are two ways to make materials at the nano-scale, bottom-up and top-down. But only the former one is commonly used for synthesis of clusters due to the tremendous surface energy which makes clusters easy to aggregate in top-down methods. After decades of studies, physicists and chemists have both separately developed different routes to make clusters of different compositions. Chemical routes can easily realize the large-scale production, but toxic chemical reagents are sometimes used in the preparation. Also, it takes time to explore new recipes for new cluster systems. Physical methods, especially cluster beam techniques, exhibit a unique advantage in the precise control of cluster size, which has allowed fundamental studies of size-dependent properties. Also, clusters are usually formed in the gas phase without any chemical ligands, which is convenient for exploring the origin of the properties relating to the cluster's surface. However, the biggest disadvantage of physical methods is the low production rate, which limits their practical applications. This section focuses on the physical methods since they are used in this thesis, but chemical methods are also briefly introduced.

1.2.1 Gas condensation cluster sources

The gas condensation cluster sources are probably the most developed technique among the physical methods, since it offers the opportunity to make clusters in gas phase and offers precise control of the cluster size (down to single atom resolution) with the help of a mass filter. In a typical gas condensation cluster source, cluster materials are firstly vaporized by various methods and then aggregate together through the atomic collisions with noble gases in a cold environment or via adiabatic supersonic expansion. Based on the material vaporization modes, it can be classified into seeded supersonic nozzle cluster source, evaporation cluster source, laser ablation cluster source and magnetron sputtering cluster source etc.

Seeded supersonic nozzle cluster source[28] is the most powerful cluster source which can provide a continuous cluster beam with a flux higher than 10^{18} atoms/s (**Figure 1.5**).[29] This cluster source is designed for low melting point metals (< 1000 ^{o}C), especially for the alkali group. In this cluster source, a metal vapor is obtained in an oven and mixed with inert gas at a high pressure (several atmospheres with metal vapor pressure of 10-100 mbar). The gas mixture then adiabatically expands to a high vacuum through a small nozzle, which leads to the cooling of the gas mixture. The cold gas mixture becomes supersaturated and allows metal atoms to condense into clusters. The formation of clusters in this cluster source is continuous unless the metal vapor density becomes too low to form a supersaturated vapor. The cooling provided by adiabatic expansion may be enough to stabilize the clusters against re-evaporating, otherwise the clusters can be further stabilized by evaporating one or two atoms.[30] The typical cluster size formed in this source is from several atoms to thousands of atoms, which depends on three parameters, temperature of the oven, pressure of the inert gas and the dimension of the nozzle. Usually, a higher evaporating temperature, a higher inert gas pressure and a smaller nozzle are beneficial for making bigger clusters. Since the clusters are neutrally- formed by condensing metal atoms in the cluster source, a further ionization process is needed for size selection.

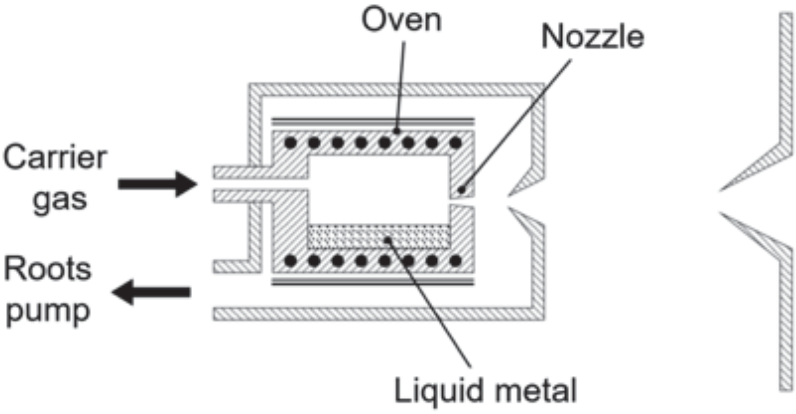

Figure 1.5 A schematic diagram of a seeded supersonic nozzle cluster source.[31] Clusters are formed by adiabatically expansion of the vaporized metal atoms in a high pressure of inert gas progressing into a high vacuum region via a small nozzle.

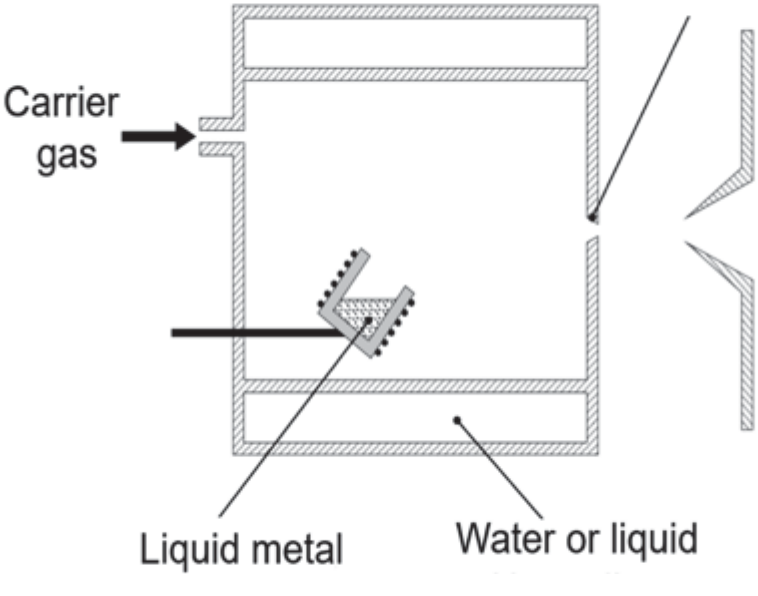

Figure 1.6 A schematic diagram of an evaporation gas condensation cluster source.[31] The evaporated metal vapor is cooled by a flow of cold inert gas to form clusters, which are then ejected through a small nozzle.

Evaporation gas condensation cluster source as shown in **Figure 1.6**, provides another way to produce continuous cluster beams with an abundant cluster flux. Similar as the seeded supersonic nozzle cluster source, the evaporated metal vapor is cooled with a flow of cold inert gas and becomes highly supersaturated. Metal atoms in the vapor condense into clusters mainly by successive single atom addition due to the low temperature of the system.[12] Then the formed clusters are ejected to another chamber to produce a cluster beam. To increase the cooling efficiency, the walls of the chamber are usually cooled by liquid nitrogen. In contrast to the seeded supersonic nozzle cluster source, the adiabatic expansion happening here is very weak and the clusters are formed before reaching the nozzle. Since the clusters are formed in a cold environment, the reverse process, re-evaporation, can be neglected. The cluster abundance is only determined by the atom collision statistics and thus usually exhibits a smooth curve in the mass spectrum (not reflecting the cluster stability). The produced cluster beam is neutral due to the nature of the cooling mechanism. As for the cluster size distribution produced in this cluster source, it highly depends on the parameters of the source (evaporation temperature, inert gas flow rate and dimension of the chamber).

Laser ablation gas condensation cluster source in **Figure 1.7** is designed for making clusters of any kind of material, from metals of high melting point (such as Pt, Co etc.) to semiconductor materials (such as Si, Ge etc.).[32] In contrast to the cluster sources discussed above, the cluster beam produced here is pulsed. In this cluster source, clusters are also formed in a condensation chamber but with much smaller dimensions.

The evaporation of cluster materials is realised by pulsed laser ablation from a target rod. The energy from the laser is focused on a small point which causes material ablation. The vaporized materials are then entrained in a pulsed cold inert gas flow (usually helium) and confined in a narrow channel which promotes the collision between the material atoms and cold carrier gas. This cooling process leads to the cluster formation as discussed above. To some extent, this source combines the evaporation gas condensation source with the hot seeded supersonic nozzle source, where the clusters are formed both in the cooling process and adiabatic expansion process. Compared with evaporation gas condensation source and seeded supersonic nozzle cluster source, the material consumption of this source is much lower (estimated 10^{-3} mole/hour, depending on the material and laser power). Cluster size distribution from this source is the same as the seeded supersonic nozzle cluster source, from several atoms to hundreds of atoms per cluster, which depends on the laser power, the pulse duration for the laser and gas flow.

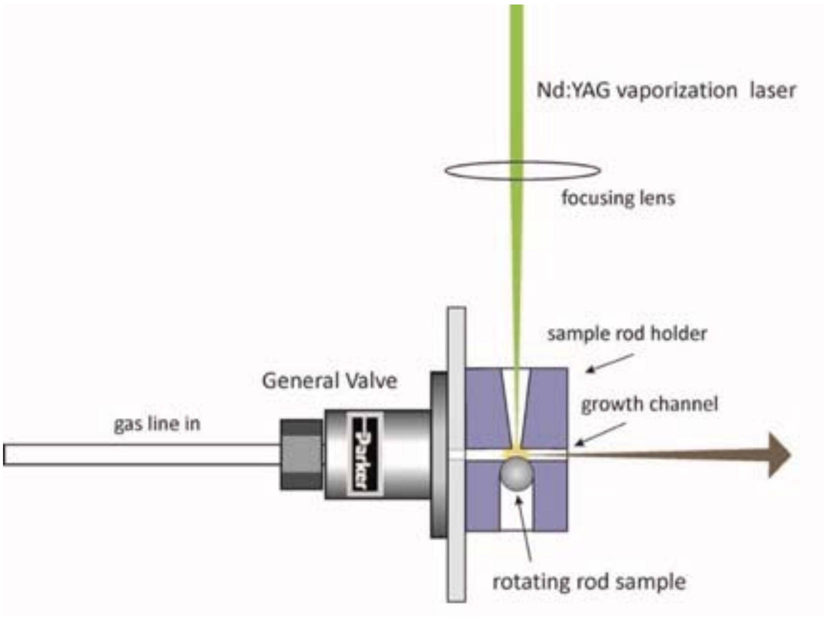

Figure 1.7 A schematic diagram of a laser ablation cluster source.[33] Instead of thermal evaporation, a focused laser beam is used to vaporise material. Clusters are formed by adiabatically expansion of the atom vapour.

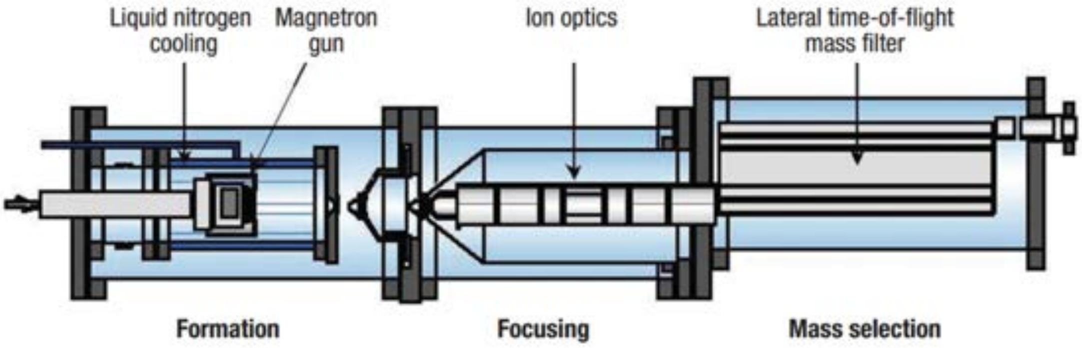

Figure 1.8 A schematic design of the magnetron sputtering, gas condensation cluster source in Nanoscale Physics Research Lab at University of Birminhgam,[27] which consists of three parts, cluster generation chamber, ion optics chamber, and mass selection chamber. A vapour of material atoms is generated by magnetron sputtering and condenses together to form clusters with the help of cooling agents. The positively charged clusters are extracted, accelerated and focused by nozzle, skimmer and a series of ion optics before entering a time-of-flight mass filter. The mass filter can select clusters with a particular mass/charge ratio for deposition.

Magnetron sputtering gas condensation cluster source, first reported in 1992 by H. Haberland,[34] combines plasma sputtering and gas condensation techniques. It was designed to produce a continuous cluster beam of any kinds of materials. After several years of improvements, the magnetron sputtering gas condensation cluster source combined with a mass filter was developed to produce size-selected clusters, which became popular in the research community. The clusters produced in this source have a wide distribution from several atoms to tens of thousands of atoms per cluster. **Figure 1.8** shows the schematic diagram of a magnetron sputtering cluster source in our group. In this cluster source, the sputtering gas (usually Ar) is ignited by a high voltage (DC for conductive targets and RF for both conductive and insulating targets) and accelerated to sputter atoms out of the target. A strong magnetic field is applied to the sputtering region to promote the sputtering efficiency and form a dense vapour of material atoms inside the condensation chamber. The sputtered atoms and small clusters condense together with help of cooling agents (He gas and Ar gas). The whole condensation chamber is cooled by liquid nitrogen to accelerate the formation of clusters. The magnetron target is mounted on the head of a moveable magnetron gun, so the condensation length can be changed during sputtering process, which affects cluster size and structure.[35] It is more likely to form bigger clusters with longer condensation length and higher pressure since clusters and atoms have more chances to collide with each other. About 60% of the produced clusters are charged due to the nature of the magnetron sputtering,[34] so no additional ionization equipment is needed for size selection. Generally, the clusters from cluster beam sources are spherical, but recently significant progress in cluster morphology control has been made with magnetron sputtering cluster source. By controlling the sputtering parameters carefully (condensation temperature and sputtering rate), iron clusters of different shapes (spherical and cubic) can be produced, as shown in **Figure 1.9**.[36-37]

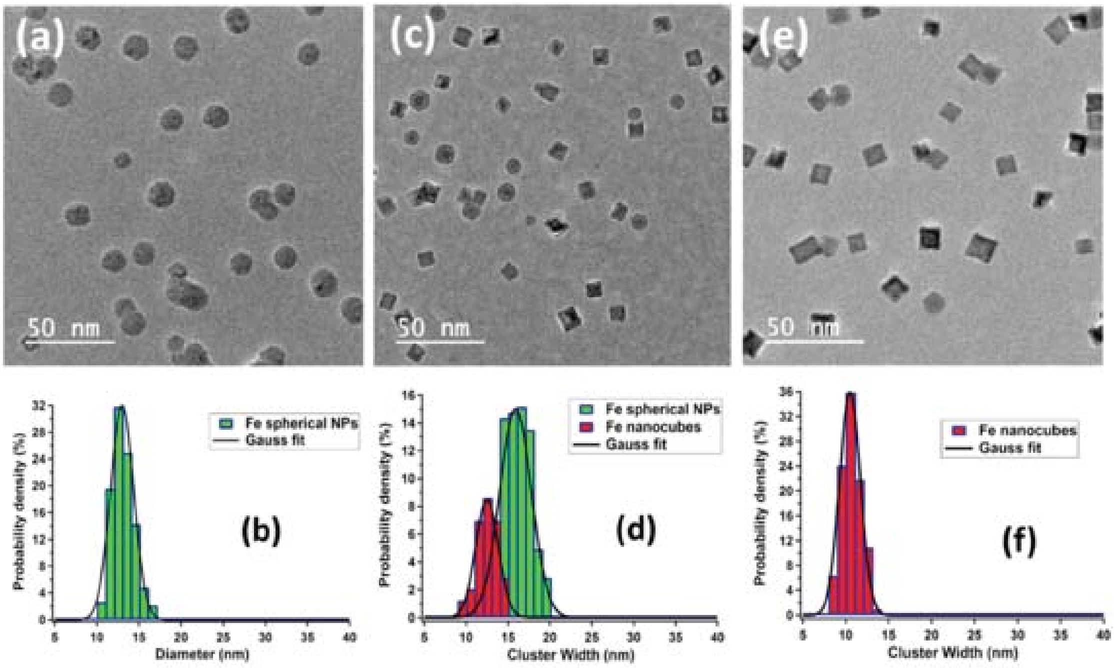

Figure 1.9 Transmission electron microscopy (TEM) images and cluster size distribution histograms of iron clusters with different shapes produced with a magnetron sputtering cluster source.[36] The morphology control is realized by regulating the condensation temperature and sputtering rate.

It should be noted that since clusters used for deposition are charged, this cluster source provides another possibility to control the cluster/support interaction by tuning the cluster deposition energy. Previous studies conducted in our group demonstrate that Ag_{147} clusters can be pinned into graphite supports when deposited with an energy above a critical threshold (10 eV per Ag atom).[38-39] Molecular dynamic simulations of

Ag_{147} clusters deposited on graphite support (in **Figure 1.10**) clearly show that with the deposition energy of 1750 eV, some Ag atoms of the cluster start to implant underneath the support, which will lead to a stronger cluster/support interaction compared with the clusters soft-landing on supports. This technique has been successfully used to immobilize protein molecules by pinned Au clusters[40] and improve Pd cluster stability against sintering for catalytic reactions.[41]

In addition, another new type of cluster beam source, matrix assembly cluster source, is recently invented in our group to address the problem of the low cluster production rate. In this thesis, part of work is performed on this system. Detailed information will be discussed in section 2.12.

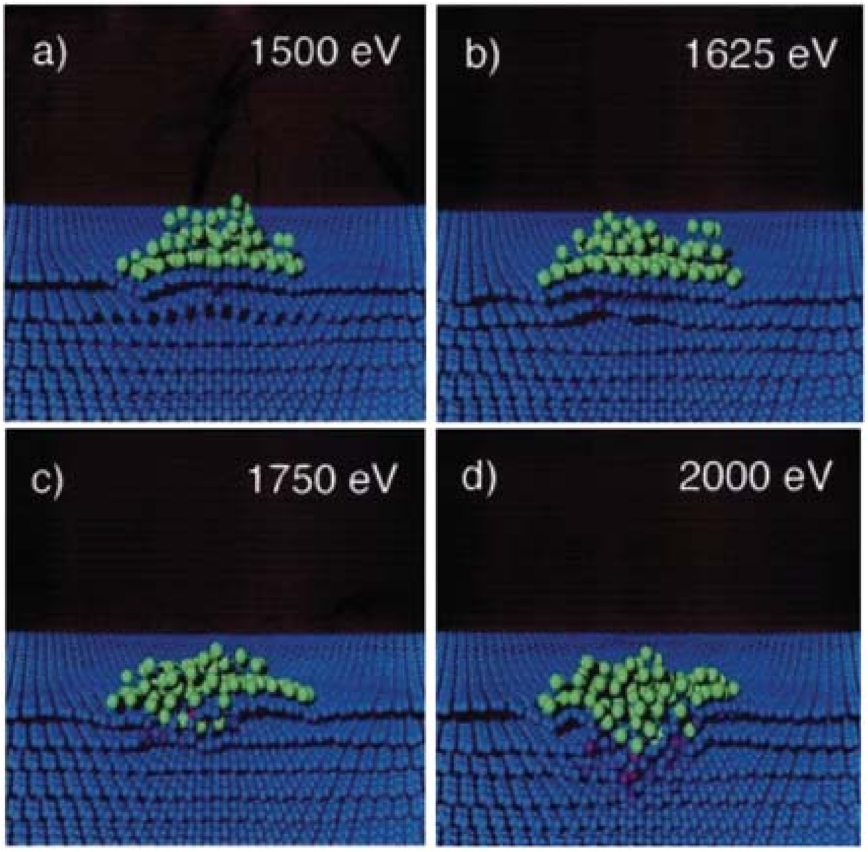

Figure 1.10 Molecular dynamics simulations of Ag_{147} clusters deposited on graphite supports with the deposition energy of 1500 eV (a), 1625 eV (b), 1750 eV (c) and 2000 eV (d).[38] With a low deposition energy (below 1750 eV), Ag cluster sits on the support without penetrating the surface. When the deposition energy exceeding 1750 eV, some Ag atoms of the cluster can implant underneath the support, which suggests cluster/support interaction can be controlled by the deposition energy.

1.2.2 Physical vapor deposition

In contrast to gas condensation cluster sources in which clusters are formed in the gas phase and can be deposited on the supports later, physical vapor deposition is a method to make clusters directly on the supports. In this method, metal atoms or metal vapors are generated by thermal evaporation or plasma sputtering (or laser ablation) and atoms then aggregate on the support by surface diffusion. Clusters made by this method usually have a wide size distribution and a droplet shape, which depend on the deposition rate, time, support nature and support surface temperature, since these can affect the surface diffusion of the atoms. For example, in **Figure 1.11**, with increase of the deposition time, Au clusters on graphene oxide become bigger and the shape of the clusters changes from hemispherical to island-shaped, which indicates coalescence happens when the distance between clusters is small enough. Physical vapor deposition has been widely used in the surface coating field, and by careful control of the preparation parameters, it may be the most efficient way to make clusters on the supports.

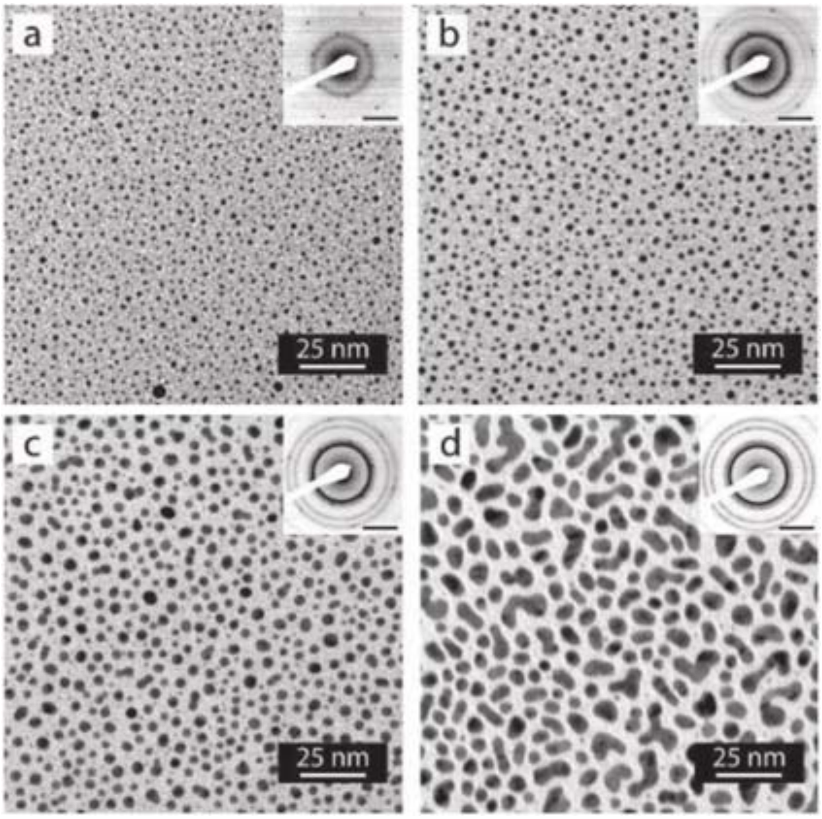

Figure 1.11 TEM bright-field images of gold (Au) nanoparticles with increasing the deposition time.[42] The shape of the deposited Au particles evolves from spherical to island-shaped.

1.2.3 Chemical preparation methods

Chemical methods provide a simple and inexpensive way to make clusters, which are quite different from the physical methods requiring complicated vacuum systems. The synthesis can occur in a beaker by simply mixing different solutions. The traditional chemical synthesis routes are wet impregnation, colloid method, deposition-precipitation, chemical vapor impregnation and so on.[43] Here, we just briefly introduce the wet impregnation and colloid method since they have been used to make reference samples in this thesis.

The impregnation method is suitable for making metal clusters/nanoparticles on porous support and has been widely used in the synthesis of catalysts. In this method, a precursor, usually a metal salt, is dissolved in an appropriate solvent. Then, the obtained solution is added to the porous support to form a thick slurry followed by drying and calcination at high temperature (200 - 500 ^{o}C). The calcination process plays two roles in this method. One is to remove the anion group from the metal salt and the other one is to promote aggregation of the metal ions to form clusters. Due to the bad control of the cluster growth process, the metal clusters produced usually have a wide size distribution, highly depending on the material, support, calcination temperature and metal loading. By successive impregnation of different metal salts, this method can also be used to synthesize binary clusters. **Figure 1.12** shows a schematic diagram of making palladium (Pd) decorated iron (Fe) nanoparticles on granular active carbon by impregnation of $Fe(NO_3)_3$ and $Pd(CH_3CO_2)_2$, sequentially.[44]

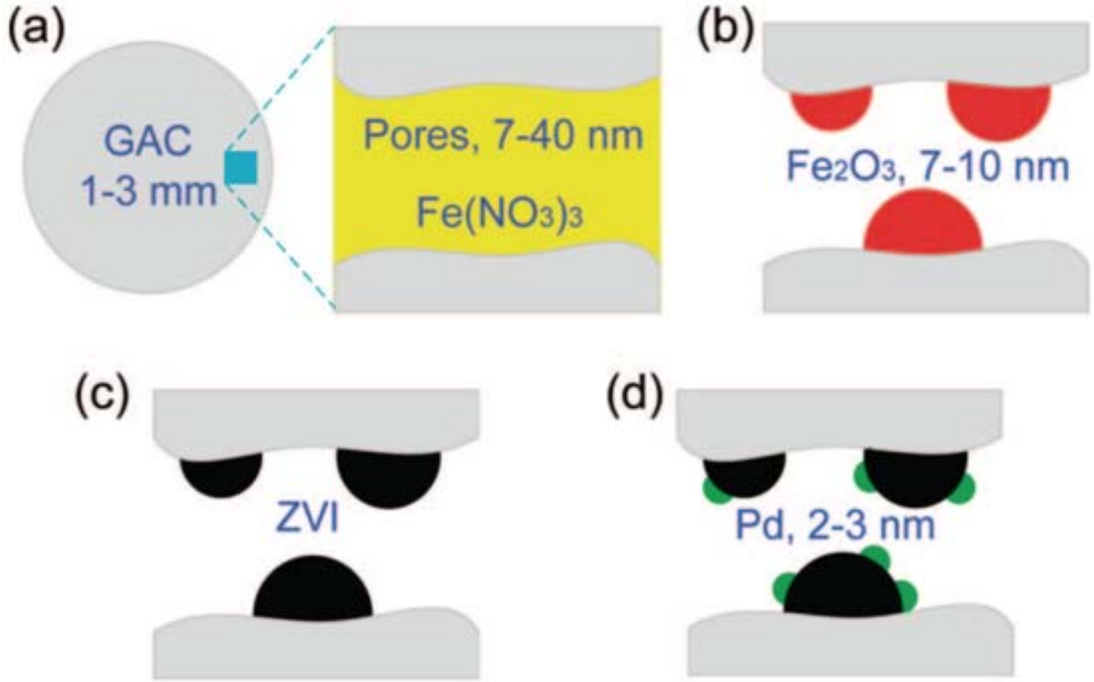

Figure 1.12 Schematic diagrams of making Pd-decorated zerovalent iron (ZVI) nanoparticles on granular active carbon (GAC) support by successive impregnation of $Fe(NO_3)_3$ and $Pd(CH_3CO_2)_2$.[44]

Compared with the impregnation method, the colloidal synthesis offers good control over size and morphology of the nanoparticles, since surfactants are used to regulate the growth process without calcination. In this method, the metal salt in solution is reduced by specific reducing agents such as sodium borohydride ($NaBH_4$) and polyols in the presence of surfactants (such as poly-vinylpyrrolidone, PVP). The surfactants act as the stabilizers which are adsorbed on the cluster surface to prevent cluster aggregation. At the same time, the existence of these surfactants also realizes the morphology control by promoting reduction onto specific crystal planes, and prohibiting growth on the others. For example, in the synthesis of colloidal Ag nanoparticles (**Figure 1.13**),[45] PVP is found to bind preferentially to the low energy crystal planes of FCC structured Ag particles, such as {111} and {100} planes. During the reaction, the synthesized Ag nanoparticles are always bounded by {100} or {111} crystal planes due to the protection of PVP. With increased reaction time, the shape of the nanoparticles evolves from cubes to truncated cubes, to cuoctahedra, then to octahedra, which indicates the growth rate of {100} crystal planes is faster than {111} crystal planes. By controlling the reaction time, Ag nanoparticles with different shapes can be obtained. In the colloidal route, it is also found that the length of the surfactant chains significantly influences the shape and size distribution of the synthesized nanoparticles. To date, the morphology control through the surfactant has been reported in many materials such as Ag,[46-47] Au,[46, 48] Pt[49] and their alloy systems. After obtaining the colloidal solutions, the produced metal colloids can be easily deposited onto porous supports by the impregnation method but without calculation.

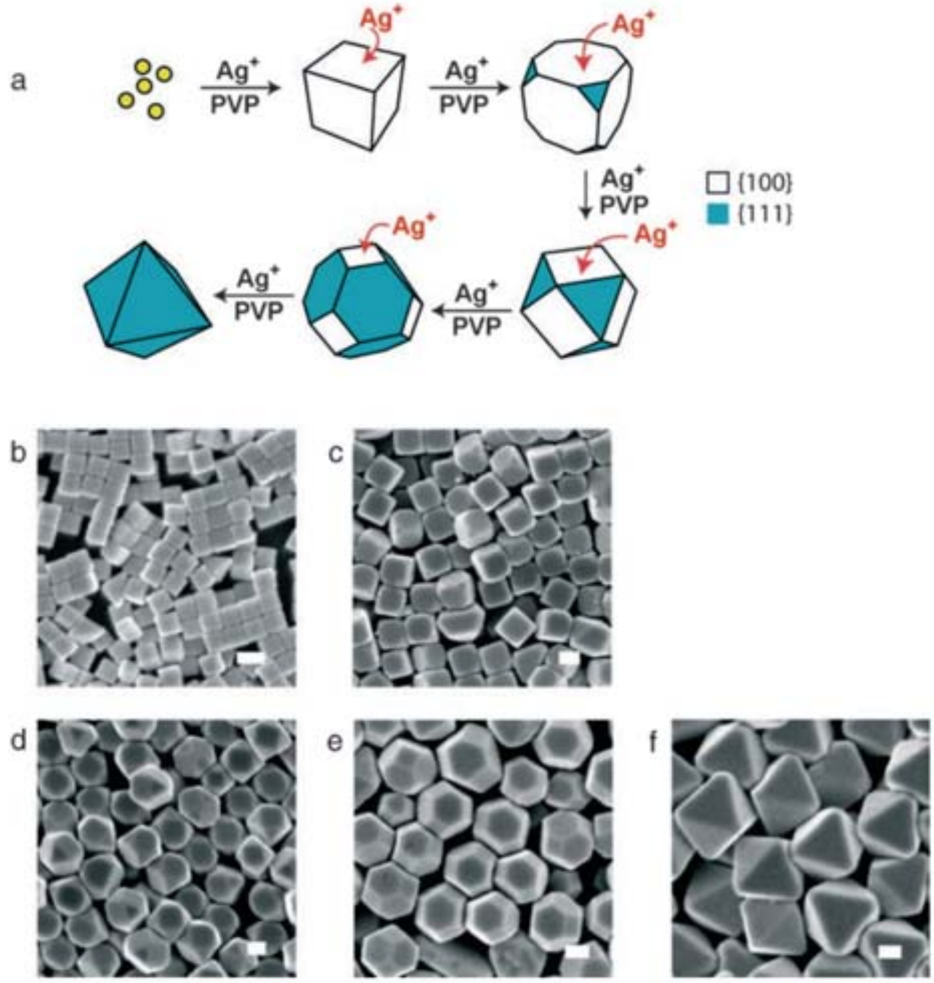

Figure 1.13 (a) A schematic diagram of the growth process for Ag nanoparticles by colloidal route in the presence of PVP. (b)-(f) SEM images of the synthesized Ag particles at different reaction times.[45] (Scale bar is 100 nm.) The added PVP molecules regulate the growth rate of different crystal planes, which cause Ag nanoparticles to have different morphologies at different growth stages.

1.3 How to measure clusters

Although early in the Middle Ages, Roman craftsmen have mastered the skill to use small noble metal particles to change the colour of glasses for decoration, clusters are only recognized in recent decades with the help of advanced characterization instruments. The analysis of the produced clusters provides fundamental understanding of the nature of clusters and impels their applications in various fields. How to measure clusters of different forms and in different environments is always crucial for the development of cluster science. In this section, the techniques to measure clusters are briefly described, ranging from their mass distribution, size distribution and atomic structures. Although other properties, for example magnetic moments, have also been extensively investigated in literatures, they are not relevant to the topic of this thesis, thus are not discussed here.

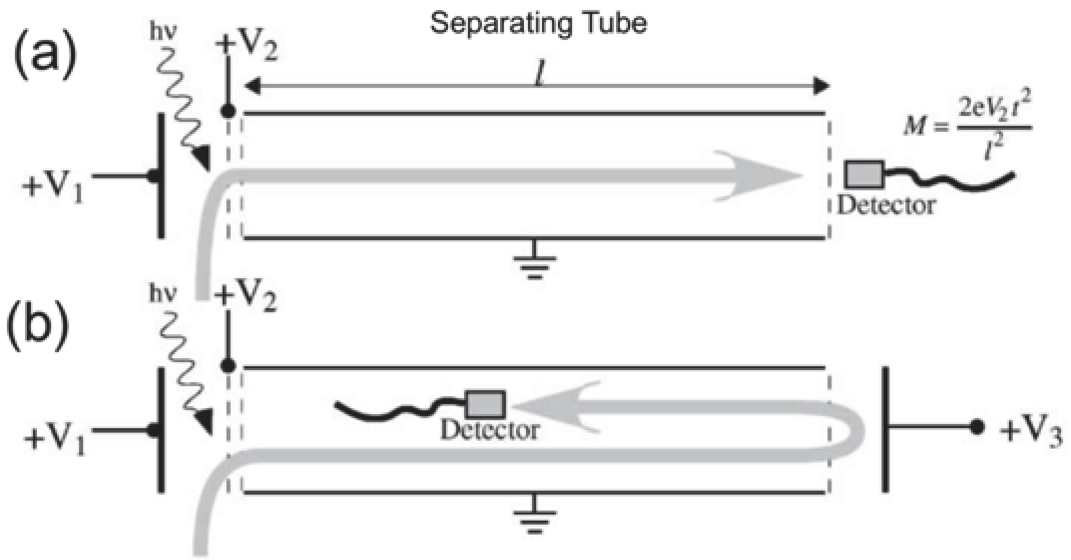

Figure 1.14 Principle of a typical TOF mass filter, (a) transmission configuration, (b) reflection configuration.[40] The charged clusters with different masses are separated by the time taken to reach the detector after obtaining same kinetic energy. Compared with transmission configuration, the reflection configuration increases the flight distance, thus improves the mass resolution.

1.3.1 Mass distribution

When it comes to the clusters, the most important information is the mass distribution. It provides the abundance of clusters of different masses in all the produced clusters. To some extent it can also reflect the cluster stability as clusters with a more stable structure usually show a higher abundance in the mass distribution. A mass distribution is usually reflected in a mass spectrum which is a plot of intensity *versus* m/z (mass to charge ratio). So, the mass spectrum is only taken from charged clusters, whereas for the neutral clusters, further ionization is needed. The setup to collect mass spectra is called a mass filter (can also select clusters for deposition). Several types of mass filters have been developed till now such as the Wien filter,[50] quadrupole mass filter[51] and time of flight (TOF) mass filter.[12] Their principles are similar: charged particles can be selected according to the flight trajectory in an electric field or in a magnetic field which is associated with certain particle charge-mass ratio. The current can be recorded which is proportional to the number of selected clusters. For example, in a conventional TOF mass filter in **Figure 1.14 (a)**, the ionized clusters are accelerated into a field-free region separating tube with the same initial kinetic energy. According to the equation of the kinetic energy and velocity ($E=\frac{1}{2}mv^2$), the initial velocity varies for clusters with different masses. Based on the time taken to reach the detector, particles with different masses can be separated. The resolution can be improved significantly by the reflection configuration as shown in **Figure 1.14 (b)**, since the flight time is increased. Similarly, the tube length and accelerating energy can also affect the resolution. Recently, a new type of lateral TOF mass filter[52] that can separate clusters laterally, was invented and successfully combined with a magnetron sputtering cluster source, thus realizing the deposition of size selected clusters. Detailed information of this new setup can be found in section 2.1.1.

1.3.2 Cluster size distribution and atomic structure

Size distribution and atomic structure are another two important features which are associated with cluster physical and chemical properties. For example, in catalysis, the clusters of different sizes are found to exhibit different activities for CO oxidation,[53-54] alkyne hydrogenation[55-57] and other reactions.[58-60] Also, the catalytic activities vary with cluster structure[61] which can affect the adsorption energy of reagents.

1.3.2.1 Size distribution

Up to now, many methods have been applied to obtain the cluster size distributions including Atomic Force Microscope (AFM),[62] Scanning Tunneling Microscope (STM),[63] Scanning Electron Microscope (SEM),[64] Transmission Electron Microscope (TEM)[65] etc. Compared with AFM and STM, which use a sharp tip to scan the sample surface and obtain the signals (AFM: interaction force signal; STM: tunneling current signal), SEM and TEM provide much faster ways to characterize cluster size distribution, in which an electron beam is used as a probe to deliver cluster information. In SEM, the surface information is delivered through the secondary electrons, whereas in TEM cluster structure information is stored in the transmitted electrons forming a projected image. Since the resolution of SEM is much lower than TEM, it is usually used for big particles. All four techniques can offer images displaying certain contrast where the cluster size can be directly measured. Instead of using visualized images, the cluster size distributions can also be obtained by dynamic light scattering (DLS) based on the photon correlation spectroscopy.[66] However, in this method, clusters must be dissolved in a suitable solvent with ligands, which limits its application in practice.

1.3.2.2 Atomic structure

The cluster atomic structure is commonly characterized by the HAADF technique of an aberration-corrected STEM, where the resolution is pushed down to sub-Angstrom level, allowing single atoms (the lattice constant of most materials is around several Angstroms) to be resolved. In STEM, a focused high-energy (80-300 keV) electron beam (spot size: ~0.1 nm) is employed to scan the sample. Some of the electrons are scattered due to the interaction with the atom nucleus. The scattered angle largely depends on the atomic number. The heavier the atom, the higher the scattered angle.[67-69] The HAADF detector is designed to collect highly scattered electrons, so the composition information is also provided in HAADF images. Detailed information can be found in Chapter 2.

For the elemental clusters, generally there are three kinds of high symmetry structures, FCC, icosahedron and decahedron. All of these structures have been observed in HAADF images of many kinds of clusters, such as Au, Ag and Pt. One example of Au_{923} clusters is shown in **Figure 1.15**.[70] The observed images match well with the simulated images calculated by the multi-slice method. Clusters with FCC structure can be regarded as a small piece of bulk material. In the cubic unit cell, eight atoms occupy each of eight corners with another six atoms located in the center of the six faces. Different from FCC structure, the icosahedron structure consists of 12 five-fold axes and 20 tetrahedral units (can be cut from FCC structure) sharing the same vertex in the center.[71] In icosahedron structure, multi-twinning is usually formed between adjacent tetrahedral units by sharing {111} crystal planes. It should be noted that the three sides of the tetrahedral unit towards the crystal center are about 5% shorter than the sides on the surface which leads to the internal strain inside the cluster.[71] The decahedron structure is another five-fold symmetry structure which is commonly observed in clusters. In contrast to the icosahedron, the common decahedral structure consists of five tetrahedral units sharing one edge in the five-fold axis. The exposed 10 crystal planes are close-packed {111} planes. Similar to the icosahedron structure, internal strain also exists inside the crystal. Clusters with these three kinds of structures usually exhibit different features in the HAADF image. For example, the ring-dot pattern usually comes from icosahedron, straight line pattern comes from FCC structure and multi-twinning structures are from decahedron. By careful observation of these features, these three structures could be distinguished.

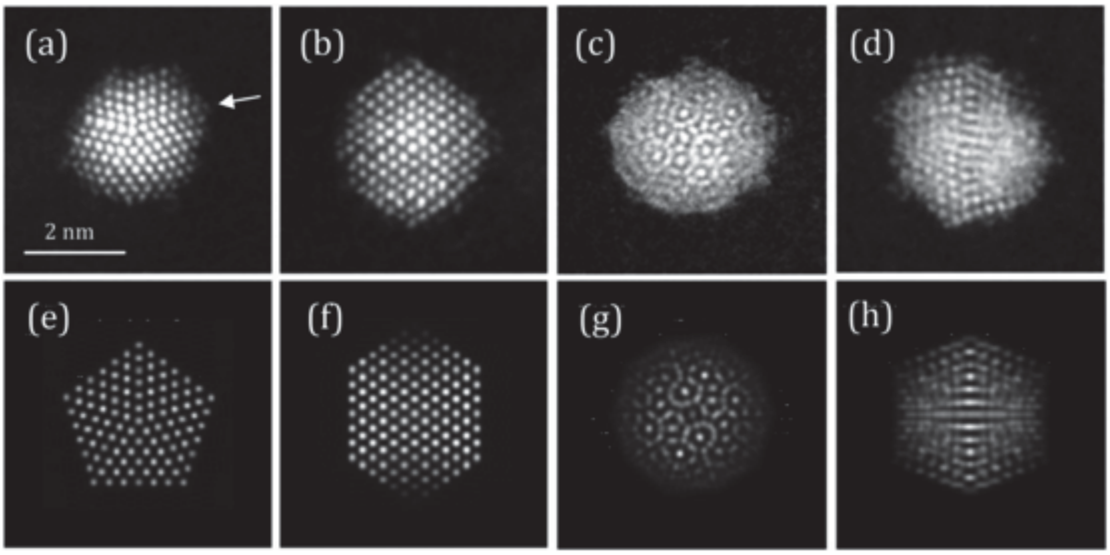

Figure 1.15 Typical HAADF images of Au_{923} with three kinds of structures (a, decahedron; b, FCC; c, icosahedron along a fivefold axis; and d, icosahedron along a twofold axis) and corresponding simulated images.[70]

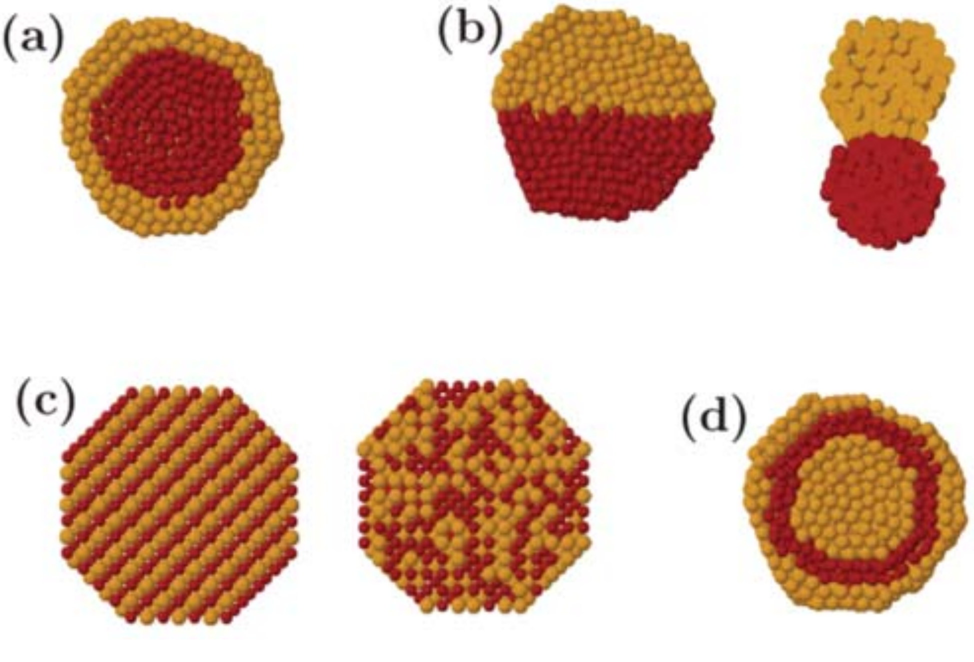

Figure 1.16 Schematics of four types of structures in bimetallic clusters. (a) core/shell structure, (b) Janus structure, (c) mixed structure, (d) three shell structure.[72]

For bimetallic clusters, in addition to the crystallographical structure, the arrangement of these two kinds of atoms is another important aspect. Basically, there are four main mixing patterns, core/shell structure, Janus structure, mixed structure, and multi-shell structure, when an element alloys with another element as shown in **Figure 1.16**. All these mixing patterns have been observed in bimetallic systems, for example core/shell structure in Pd/Pt system,[73] mixed structure in Au/Cu system,[74] multishell structure in Au/Pd system [75] and Janus structure in Au/AgO_2 system.[76] Since HAADF technique can also provide composition information, recently it has also become a very powerful tool in distinction of structure of bimetallic clusters. In HAADF images, a brighter intensity in an atomic column usually means more atoms or more heavier atoms are in the column. The HAADF intensity line profile across a cluster with a core/shell structure, for example, usually displays a parabolic curve with a hump in the middle for a heavier core or with a trough in the middle for a lighter core. **Figure 1.17** shows typical HAADF images and simulated HAADF intensity profiles across Au/Cu clusters with different metal cores. The intensity profile for a pure cluster is a simple smooth curve, whereas for an Au/Cu core/shell or Cu/Au core/shell cluster, a hump or a trough can be found in the middle of the curve, respectively.

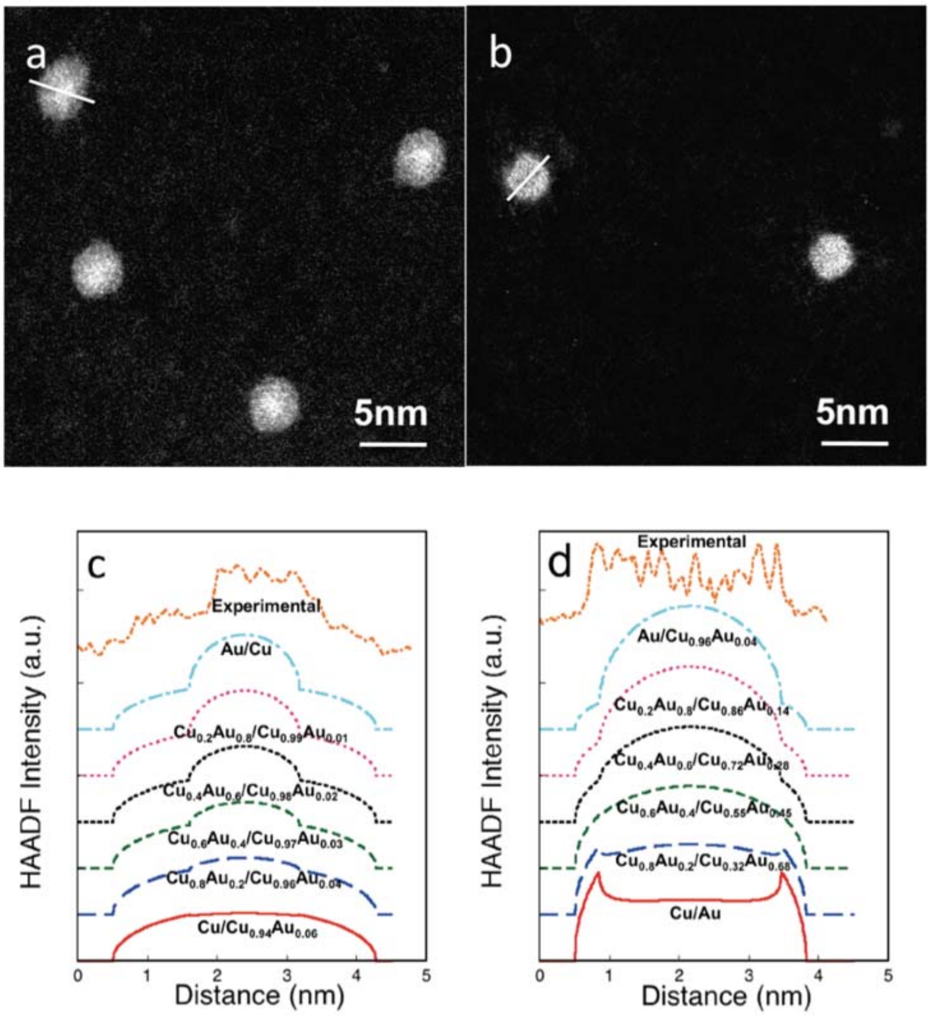

Figure 1.17 Typical HAADF images and simulated HAADF intensity profiles for two kinds of Au/Cu binary clusters. (a), (c) Au/Cu core-shell clusters. (b), (d) Cu/Au core/shell clusters.[77] The HADDF images exhibit brighter cores for Au/Cu core/shell clusters and darker cores for Cu/Au core/shell clusters, which are consistent with the simulated HAADF intensity profiles for Au/Cu and Cu/Au core/shell clusters.

1.4 Catalysis by physically prepared metal clusters

Although metal clusters have potential applications as catalytic particles,[78-79] as binding sites for biomolecules,[80-81] as sensitizers for enhancing energy harvest[82-83] etc etc., in reality the most active and thorough exploitation is still in catalysis. The first discovery of small metal particles as catalysts can be dated back to 200 years ago. Jöns

Jacob Berzelius found Pt particles can catalyze oxidation of alcohol to ethylic acid by accident. After two hundred years of development, chemical methods have realized the large-scale production of metal clusters on different supports, which have been widely used in industrial catalysts. However, clusters made from chemical methods usually have a wide size distribution, which indicates only a small proportion of material contribute significantly in the catalytic reaction. In addition, the wide usage of chemical ligands to prevent cluster aggregation largely decreases the cluster activity in some cases. Considering only limited metal sources exist in the earth, especially for some noble metals, the optimal utilization of this material is an important direction for scientific research.

In contrast to chemical methods, physical methods (cluster beam technique) can produce ligand-free clusters with specific sizes, which allows the investigation of the size-dependent catalytic activity. Also, in this method, the interaction between clusters and supports can be tuned by selecting the landing impact energy, which makes it possible to study the influence of the interface to the activity. It can be imagined, in the long run, that we can select the most active clusters as the catalysts and tune their interaction with the supports, which will increase the utilization of materials. To this end, enormous effort has been made to improve the performance and application of the cluster beam technique.

In this section, I will briefly review the current experimental studies of catalysis using physically produced clusters from three aspects: i) catalysis by free clusters, ii) catalysis by supported clusters in ultra-high vacuum and iii) catalysis by supported clusters in specially-designed reactors under realistic conditions.

1.4.1 Catalysis by free clusters

To understand the origin of the catalytic activity happening on the metal-cluster-based catalysts, the first step is always to investigate the activity directly on the free metal clusters, since the involvement of the support can complicate the situation by charge transfer[84-85] etc. Clusters made by cluster beam techniques are produced in the gas phase without any protecting ligands, which makes the catalysis measurement direct on the free clusters possible. This measurement is usually conducted in a UHV setup which combines a cluster source with an analytical section, such as TOF mass filter. In between there is a reactor tube allowing the introduction of reagent gases.[86]

In general, the catalytic reaction starts from the adsorption of the reagents on the cluster surface. The initial adsorption study can provide fundamental information required to understand the reaction process. So, the early studies on the cluster catalysis are mainly focused on the adsorption study, such as CO on Au clusters[87] and transition metal clusters;[86] O_2 on Ag[88] and Au clusters;[89] H_2 on transition metal clusters[90-91] etc. Taking CO oxidation as an example, the first step of the reaction is associated with CO adsorption on the metal clusters. Cox et al.[86] investigated the CO adsorption process on small transition metal clusters (V, Fe, Co, Ni, Cu, Nb, Mo, Ru, Pd, W, Ir, Pt and Al) containing up to 14 atoms. By comparing the bare metal cluster peak intensity in the mass spectra detected with and without CO gas, the accurate cluster size exhibiting reactivity can be found. As shown in **Figure 1.18**, the injection of CO gas causes a decrease in the bare metal cluster peak, which indicates CO molecules are adsorbed on the clusters. The peaks numbered 7.1, 7.2 etc. correspond to the product of $V_x(CO)_y$. It is shown that for all the transition metals, the CO chemisorption can readily occur on the clusters with the number of atoms more than 4 (3 for vanadium clusters). The strength of the metal-CO bond affects the minimum cluster size where the adsorption occurs. A similar CO adsorption study has also been conducted on Au clusters, but there even the small Au_2 clusters can exhibit CO chemisorption.[87]

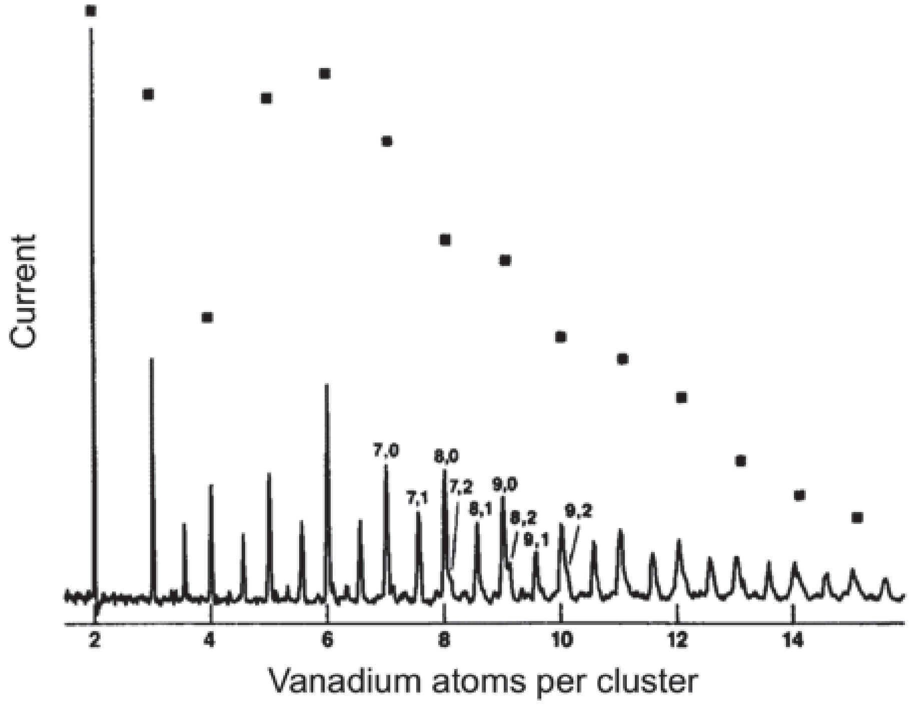

Figure 1.18 TOF mass spectra of the vanadium clusters with (solid line) and without CO (dots).[86] The peaks numbered 7.1, 7.2 etc. correspond to the product of $V_x(CO)_y$. Vanadium clusters start to show activities when their size reaches 3 atoms per cluster.

Adsorption studies can quickly determine which cluster size is active, but obviously it also has its own limitations: (i) usually only one reactant gas is investigated at one time, but the adsorption properties might change when another reactant is introduced;[92] (ii) the residence time of clusters in the reactor tube is very short, only around 100-200 μs, which is long enough for the chemisorption but not so for kinetic studies. In the past few years, the cluster ions have been successfully trapped in an octupole ion trap for several seconds which allows performing kinetic studies of the real catalytic reaction on the free clusters. Socaciu et al. investigated the CO oxidation on size selected Au_2^- clusters.[93] In their research, both O_2 and CO gases were introduced into the ion trap. All the intermediates for each step of the reaction were detected as the reaction time. By changing the reaction temperature and pressure, the kinetics of the reaction was systematically studied. Combined with theoretical calculations on the stability of all the possible intermediates, a reaction mechanism was proposed as shown in **Figure 1.19 (a)**, where a metastable intermediate, $Au_2CO_3^-$, was found crucial for this reaction. In addition to the CO oxidation, the ethylene formation from methane catalyzed by Au_2^- clusters was also investigated by a similar method,[94] where a new methane activation and C-C bond formation mechanism was proposed as shown in **Figure 1.19 (b)**. A recent study also shows that this type of catalysis study can be performed on neutral clusters by ionizing and analyzing the reacted products, for example CO oxidation on neutral Au clusters.[95] Although the kinetics of the reaction cannot be obtained, combined with theoretical calculations some possible reaction mechanisms could also be deduced.

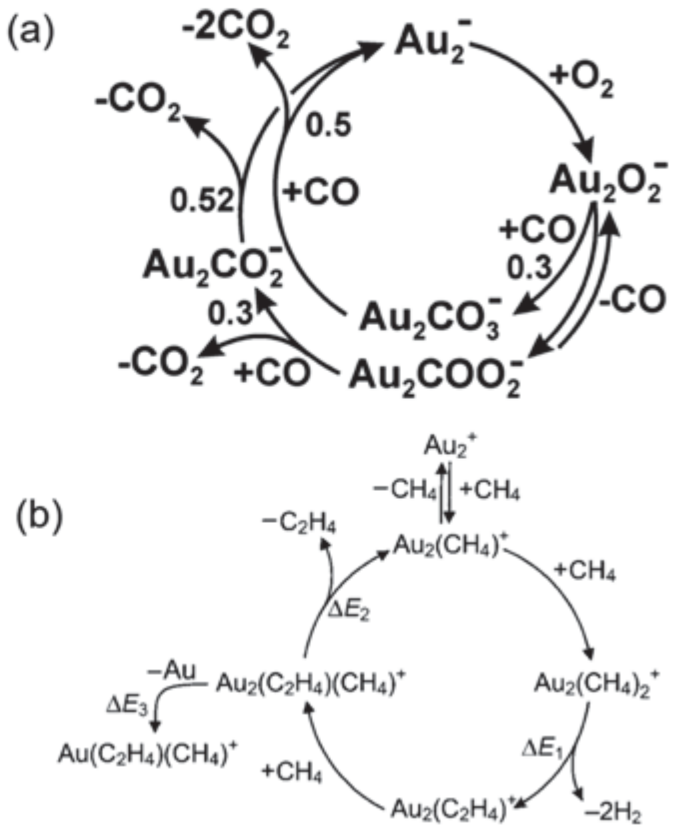

Figure 1.19 Schematic diagram of the reaction mechanism for CO oxidation (a) and ethylene formation (b) occurring on size-selected Au_2^- clusters in the gas phase.[93-94] The intermediates formed during the reactions are determined by the combination of mass spectra and stability calculations.

It should be noted that catalysis on free clusters is usually tested on small clusters, since the cluster flux dramatically decreases with an increasing cluster size. Given the reaction only happens in a small reactor within a short time, a reasonably high cluster flux is needed to obtain a sufficient catalytic signal. Although the reaction conditions are far away from realistic reaction conditions, these studies can still give us some insights into the catalytic properties. In particular, it can provide information on the intermediate formed during the reaction, which can help us clarify the reaction mechanism.

1.4.2 Catalysis by supported clusters in ultra-high vacuum

Catalysis studies on free clusters can clarify the cluster intrinsic activities, but in practice, clusters themselves cannot be used as catalysts alone due to the severe aggregation resulting from the enormous surface energy. Usually, clusters are deposited on different supports when they are used as catalysts. Therefore, studies of the support effect become crucial to understand and improve catalytic activities. However, the cluster production rate from cluster beam techniques is very low, especially for size selected clusters. Therefore, catalysis measurements on supported clusters are usually conducted in an ultra-high vacuum chamber which allows to detect the products from the reaction.

Since the cluster beam technique can deposit size-selected clusters, Sanchez et al. first investigated the size-dependent catalytic properties of magnesium oxide (MgO) supported Au clusters for CO oxidation.[96] In their research, Au clusters with different number of atoms (from 2 to 20) were separately deposited on defect-poor and defect-rich MgO (100) films. It was found that the Au_8 clusters deposited on the defect-rich MgO film were the smallest clusters which can catalyze CO oxidation at low temperature (~140 K), whereas the Au_8 clusters supported on the defect-poor MgO film were inactive to this reaction, as shown in **Figure 1.20**. The oxygen-vacancy defects and the electron transfer from MgO surface to Au clusters were found to play an important role in activating Au clusters. Further Fourier-transform infrared spectroscopy (FTIR) study[84] showed that during the reaction there was also an electron back donation from Au clusters bound to the oxygen-vacancy defects to CO molecules adsorbed on the clusters. The charge transfer from the support to the clusters was also observed on the MgO supported Pd clusters for acetylene cyclotrimerization,[97] where even single Pd atoms were found to be sufficient to catalyze the reaction at room temperature (300 K).

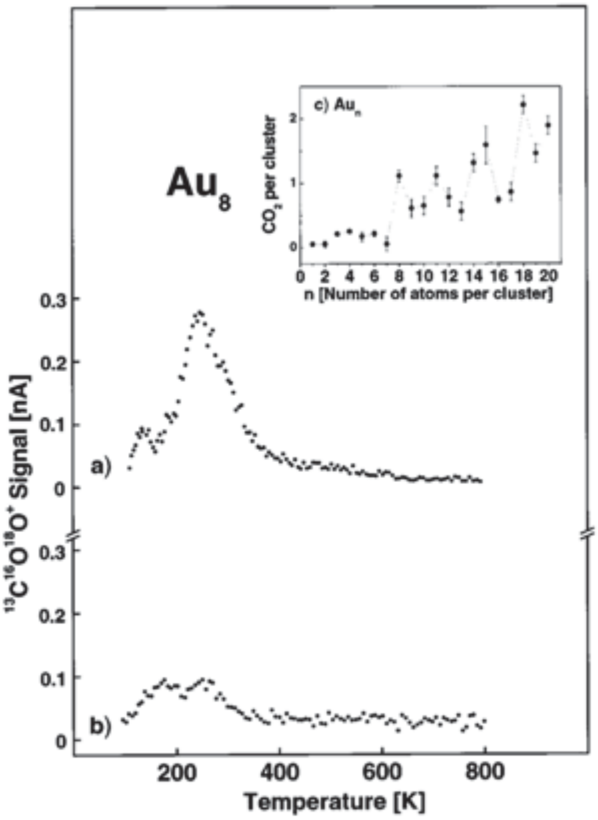

Figure 1.20 CO oxidation catalysed by Au_8 clusters supported on MgO (100) film with oxygen defects (a) and without oxygen defects (b). (c) Activities of CO oxidation on MgO supported Au clusters with different number of atoms ($n \leq 20$) as the expression of CO_2 per cluster.[96]

In addition to charge transfer, the support reduction state can also influence the cluster activity. It is found that the CO oxidation activity of size-selected Pt clusters on a strongly reduced TiO_2 support is much lower than that on a slightly reduced support. The quenching effect that the adsorbed oxygens spill over to the support and react with the Ti^{3+} interstitials formed in the strongly reduced TiO_2 support, is believed to account for the decreased activity, as shown in **Figure 1.21**.

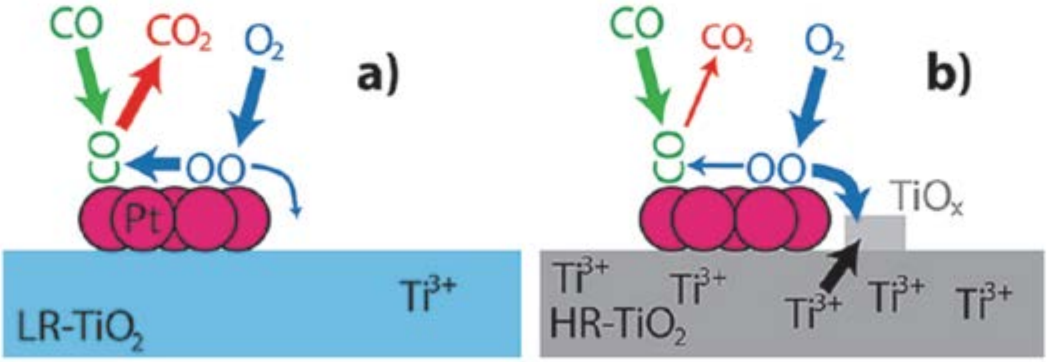

Figure 1.21 Schematic diagram of the quenching effect of the substrate. On the slightly reduced TiO_2 support (LR-TiO_2), the adsorbed oxygen can only react with the adsorbed CO (a), whereas on the strongly reduced TiO_2 support (HR-TiO_2), the absorbed O_2 can also depleted by reacting with the Ti^{3+} interstitials.[98]

1.4.3 Catalysis by supported clusters in reactors

For a long time, catalysis studies on physically produced clusters were limited to ultrahigh vacuum experiments due to the extremely low production rate. However, clusters as catalysts must be used under realistic reaction conditions, since the cluster structures and activities might change with the reaction conditions. This indicates the final evaluation of their activities must be carried out under realistic reaction conditions.

The early exploration of the catalytic activities of the physically deposited clusters under realistic reaction conditions was conducted by Stefan Vajda and his colleagues.[99] They combined the cluster source with mass spectrometry and grazing incidence small angle x-ray scattering (GISAXS) which realized the in-situ monitoring of the cluster size and shape evolution during the reaction. Size-selected clusters were deposited on the wafer substrate coated with a thin layer of amorphous alumina, and the wafer was placed in a home-made reaction cell (~25 mL) where the reaction proceeded in a continuous flow mode at pressure of ~1 bar. The reacted products were analyzed with the mass spectrometer as a function of the reaction time and reaction temperature. By using this method, they investigated the shape evolution of Ag clusters in the epoxidation of propene in situ and found that the shape of Ag clusters reversibly changed during the reaction and the distinct changes in the formation of the acrolein and propylene oxide were corrected to the shape evolution. The same method was also used in investigating the size and support composition effects of the Pd clusters for oxidative decomposition of methanol [100] and the suppression of sintering of Pd clusters supported on graphite surfaces for catalysis.[41]

In addition, Hansen et al.[101] proposed another method to test the physically produced clusters under realistic reaction conditions. The idea is to perform the catalytic reaction on a silicon chip as shown in **Figure 1.22**. A reaction micro-chamber (100 mm^3) and some gas channels are prepared by reactive ion etching. The reagent gases are mixed together and guided into the reaction chambers where metal clusters are deposited for the reaction. Since only a small gas flow (~4×10^{16} molecules/s) is introduced into the reaction chamber, the reagent gases can fully react and be analyzed, which provides a high sensitivity to the catalytic reaction at pressure ranging from 0.1 to 5.0 bar. This reactor has been successfully tested for CO oxidation[101] and ammonia oxidation[102] on low coverage platinum thin films. However due to sealing problems at high temperatures and the time-consuming fabrication, it has not been widely used in cluster catalysis yet.

In addition to the two methods discussed above, in this thesis we introduced another method to test the cluster activity under realistic reaction conditions, which combines dicing techniques and the MACS. Detailed information can be found in Chapter 2.

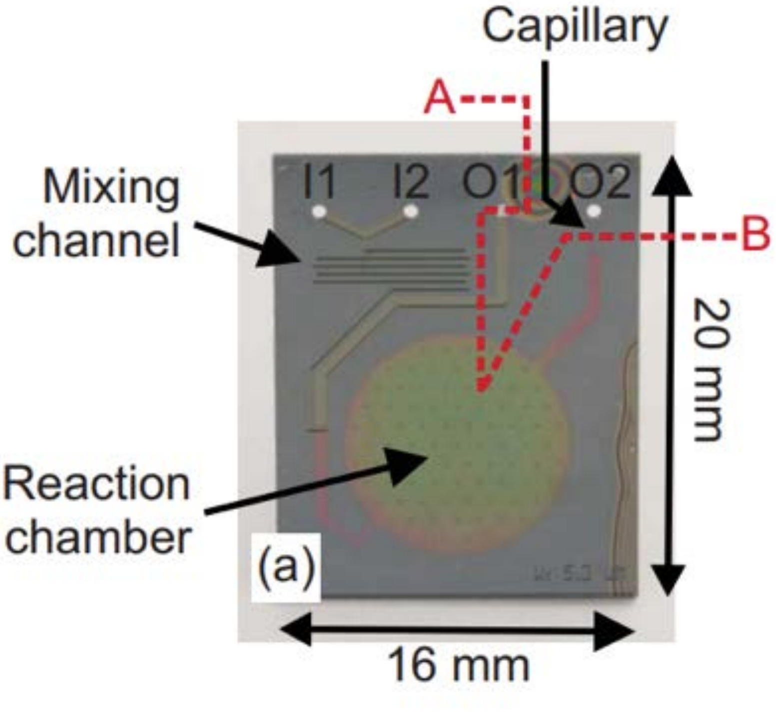

Figure 1.22 Photograph of a silicon microreactor which consists of a reaction chamber, mixing channels, gas inlets and outlets.[101] The reagent gases are introduced through the gas inlets and mixed together in the mixing channel. A small portion of the mixed gasses are then guided into the reaction chambers where metal clusters are deposited to

catalyse the reaction. After the reaction, the reacted mixture can exit the reactor through the gas outlets for composition analysis.

1.5 Challenges for the cluster beam technique in catalysis

Cluster beam techniques have been well developed in the past 30 years. By combinations of different mass filters, metal clusters with precise number of atoms can be deposited on different supports, which led to the discovery of size-dependent catalytic activities. However, these techniques are still confronted with two challenges which hamper their further application in catalysis.

The first challenge is the low cluster production rate. For example, industrial R&D typically needs 1 gram of catalyst with 10 milligrams of clusters (1wt% loading) for catalytic measurements, whereas the conventional cluster source typically only produces a size-selected cluster beam current of about ~0.1 nA, equivalent to 1.5 μg Au_{100} clusters per day. This production rate is perfectly adequate for surface science studies in ultra-high vacuum, but far from sufficient for industrial R&D experiments. Considering a production rate of 10 mg clusters per hour is required for the industrial test, a scale up of at least 5 orders of magnitude is needed.

The second challenge is how to transform the clusters into real catalysts. Even if we can produce enough clusters for the catalysis, providing enough surface area under the beam to anchor clusters evenly on the support without surface aggregation is another problem. Experiments have shown that when clusters are deposited on the stirred or agitated powder supports, surface agglomeration occurs severely even at the loading of

0.1%.[103] Only after addressing these two challenges, can the cluster beam technique be widely used in producing practical catalysts.

References

(1) Castleman JR., A. W.; Keesee, R. G. Gas-phase clusters: spanning the states of matter. *Science* **1988,** *241*, 36.

(2) Castleman, J. A. W.; Bowen, J. K. H. Clusters: structure, energetics, and dynamics of intermediate states of matter. *J. Phys. Chem.* **1996,** *100*, 12911.

(3) Cleveland, C. L.; Landman, U. The energetics and structure of nickel clusters: Size dependence. *J. Chem. Phys.* **1991,** *94* (11), 7376.

(4) Yacamán, M. J.; Ascencio, J. A.; Liu, H. B.; Gardea-Torresdey, J. Structure shape and stability of nanometric sized particles. *J. Vac. Sci. Technol. B* **2001,** *19* (4), 1091.

(5) Doyea, J. P. K.; Wales, D. J. Global minima for transition metal clusters described by Sutton–Chen potentials. *New J. Chem.* **1988,** *22*, 733.

(6) Doye, J. P. K.; Wales, D. J.; Berry, R. S. The effect of the range of the potential on the structures of clusters. *J. Chem. Phys.* **1995,** *103* (10), 4234.

(7) Knight, W. D.; Clemenger, K.; de Heer, W. A.; Saunders, W. A.; Chou, M. Y.; Cohen, M. L. Electronic shell structure and abundances of sodium clusters. *Phys. Rev. Lett.* **1984,** *52* (24), 2141.

(8) Harbola, M. K. Magic numbers for metallic clusters and the principle of maximum hardness. *PNAS* **1992,** *89*, 1036.

(9) Martin, T. P.; Bergmann, T.; Gohlich, H.; Lange, T. Shell structur of clusters. *J. Phys. Chem.* **1991,** *95*, 6421.

(10) Katakuse, I.; Ichihara, T.; Fujita, Y.; MAtsuo, T.; Sakurai, T.; Matsuda, H. Mass distributions of negative cluster ions of copper, silver, and gold. *Int. J. Mass Spectrom. Ion*

Processes **1986,** *74*, 33.

(11) Winter, B. J.; Parks, E. K.; Riley, S. J. Copper clusters: The interplay between electronic and geometrical structure. *J. Chem. Phys.* **1991,** *94* (12), 8618.

(12) de Heer, W. A. The physics of simple metal clusters: experimental aspects and simple models. *Rev. Mod. Phys.* **1993,** *65* (3), 611.

(13) Katakuse, I.; Ichihara, T.; Fujita, Y.; Matsuo, T.; Sakurai, T.; Matsuda, H. Correlation between mass distributions of zinc, cadmium clusters and electronic shell structure. *Int. J. Mass Spectrom. Ion Processes* **1986,** *69*, 109.

(14) Polymeropoulos, E. E.; Brickmann, J. Magic numbers in ionized rare-gas clusters. *Surf. Sci.* **1985,** *156*, 563.

(15) Echt, O.; Reyes Flotte, A.; Knapp, M.; Sattler, K.; Recknagel, E. Magic numbers in mass spectra of Xe, $C_2F_4Cl_2$ and SF_6 Clusters. *Berichte der Bunsengesellschaft für physikalische Chemie* **1982,** *86*, 860.

(16) Pellarin, M.; Baguenard, B.; Vialle, J. L.; Lermé, J.; Broyer, M.; Miller, J.; Perezc, A. Evidence for icosahedral atomic shell structure in nickel and cobalt clusters. Comparison with iron clusters. *Chem. Phys. Lett.* **1994,** *217*, 349.

(17) Haberland, H.; Hippler, T.; Donges, J.; Kostko, O.; Schmidt, M.; von Issendorff, B. Melting of sodium clusters: where do the magic numbers come from? *Phys. Rev. Lett.* **2005,** *94* (3), 035701.

(18) Brack, M. The physics of simple metal clusters: self-consistent jellium model and semiclassical approaches. *Rev. Mod. Phys.* **1993,** *65* (3), 677.

(19) Lang, N. D.; Kohn, W. Theory of metal surfaces: charge density and surface energy. *Phys.*

Rev. B **1970,** *1* (12), 4555.

(20) Jahn, H. A.; Teller, E. Stability of polyatomic molecules in degenerate electronic states-I-Orbital degeneracy. *Proceedings of the Royal Society of London. Series A, Mathematical and Physical Sciences* **1937,** *164*, 117.

(21) Nilsson, S. G.; Tsang, C. F.; Sobiczewski, A.; Szymański, Z.; Wycech, S.; Gustafson, C.; Lamm, I. L.; Möller, P.; Nilsson, B. On the nuclear structure and stability of heavy and superheavy elements. *Nucl. Phys. A* **1969,** *131*, 1.

(22) Clemenger, K. Ellipsoidal shell structure in free-electron metal clusters. *Phys. Rev. B* **1985,** *32* (2), 1359.

(23) Martin, T. P.; Bergmann, T.; Göhlich, H.; Lange, T. Observation of electronic shells and shells of atoms in large Na clusters. *Chem. Phys. Lett.* **1990,** *172*, 209.

(24) Martin, T. P.; Bergmann, T.; Gohlich, H.; Lange, T. Evidence for icosahedral shell structure in large magnesium clusters. *Chem. Phys. Lett.* **1991,** *176*, 343.

(25) Martin, T. P.; Näher, U.; Schaber, H.; Zimmermann, U. Evidence for a size-dependent melting of sodium clusters. *J. Chem. Phys.* **1994,** *100* (3), 2322.

(26) P., M. T. Shell of atoms. *Phys. Rep.* **1996,** *273*, 199.

(27) Baguenard, B.; Pellarin, M.; Lermé, J.; Vialle, J. L.; Broyer, M. Competition between atomic shell and electronic shell structures in aluminum clusters. *J. Chem. Phys.* **1994,** *100* (1), 754.

(28) Bewig, L.; Buck, U.; Mehlmann, C.; Winter, M. Seeded supersonic alkali cluster beam source with refilling system. *Rev. Sci. Instrum.* **1992,** *63* (8), 3936.

(29) Binns, C. Nanoclusters deposited on surfaces. *Surf. Sci. Rep.* **2001,** *44*, 1.

(30) Bjornholm, S.; Borggreen, J.; Echt, O.; Hansen, K.; Pedersen, J.; D., R. H. The influence of shells, electron thermodynamics, and evaporation on the abundance spectra of large sodium metal clusters. *Z. Phys. D-Atoms, Molecules and Clusters* **1991,** *19*, 47.

(31) Goldby, I. M. Dynamics of molecules and clusters at surfaces. University of Cambridge, 1996.

(32) Milani, P.; deHeer, W. A. Improved pulsed laser vaporization source for production of intense beams of neutral and ionized clusters. *Rev. Sci. Instrum.* **1990,** *61* (7), 1835.

(33) Duncan, M. A. Invited review article: laser vaporization cluster sources. *Rev. Sci. Instrum.* **2012,** *83* (4), 041101.

(34) Haberland, H.; Karrais, M.; Mall, M.; Thurner, Y. Thin films from energetic cluster impact: A feasibility study. *J. Vac. Sci. Technol. A* **1992,** *10* (5), 3266.

(35) Plant, S. R.; Cao, L.; Palmer, R. E. Atomic structure control of size-selected gold nanoclusters during formation. *J. Am. Chem. Soc.* **2014,** *136* (21), 7559.

(36) Zhao, J.; Baibuz, E.; Vernieres, J.; Grammatikopoulos, P.; Jansson, V.; Nagel, M.; Steinhauer, S.; Sowwan, M.; Kuronen, A.; Nordlund, K.; Djurabekova, F. Formation mechanism of Fe nanocubes by magnetron sputtering inert gas condensation. *ACS Nano* **2016,** *10* (4), 4684.

(37) Wang, C. M.; Baer, D. R.; Amonette, J. E.; Engelhard, M. H.; Qiang, Y.; Antony, J. Morphology and oxide shell structure of iron nanoparticles grown by sputter-gas-aggregation. *Nanotechnology* **2007,** *18* (25), 255603.

(38) Carroll, S. J.; Pratontep, S.; Streun, M.; Palmer, R. E.; Hobday, S.; Smith, R. Pinning of size-selected Ag clusters on graphite surfaces. *The Journal of Chemical Physics* **2000,** *113* (18),

7723.

(39) Palmer, R. E.; Pratontep, S.; Boyen, H.-G. Nanostructured surfaces from size-selected clusters. *Nat. Mater.* **2003,** *2*, 443.

(40) Leung, C.; Xirouchaki, C.; Berovic, N.; Palmer, R. E. Immobilization of Protein Molecules by Size-Selected Metal Clusters on Surfaces. *Adv. Mater.* **2004,** *16* (3), 223.

(41) Yin, F.; Lee, S.; Abdela, A.; Vajda, S.; Palmer, R. E. Communication: Suppression of sintering of size-selected Pd clusters under realistic reaction conditions for catalysis. *J. Chem. Phys.* **2011,** *134*, 141101.

(42) Pandey, P. A.; Bell, G. R.; Rourke, J. P.; Sanchez, A. M.; Elkin, M. D.; Hickey, B. J.; Wilson, N. R. Physical vapor deposition of metal nanoparticles on chemically modified graphene: observations on metal-graphene interactions. *Small* **2011,** *7* (22), 3202.

(43) White, R. J.; Luque, R.; Budarin, V. L.; Clark, J. H.; Macquarrie, D. J. Supported metal nanoparticles on porous materials. Methods and applications. *Chem. Soc. Rev.* **2009,** *38* (2), 481.

(44) Choi, H.; Al-Abed, S. R.; Agarwal, S.; Dionysiou, D. D. Synthesis of reactive nano-Fe/Pd bimetallic system-impregnated activated carbon for the simultaneous adsorption and dechlorination of PCBs. *Chem. Mater.* **2008,** *20*, 3649.

(45) Tao, A.; Sinsermsuksakul, P.; Yang, P. Polyhedral silver nanocrystals with distinct scattering signatures. *Angew. Chem. Int. Ed.* **2006,** *45* (28), 4597.

(46) Wiley, B.; Sun, Y.; Xia, Y. Synthesis of silver nanostructures with controlled shapes and properties. *Acc. Chem. Res.* **2007,** *40*, 1067.

(47) Sun, Y.; Xia, Y. Shape-controlled synthesis of gold and silver nanoparticles. *Science* **2002,**

298, 2176.

(48) Kim, F.; Connor, S.; Song, H.; Kuykendall, T.; Yang, P. Platonic gold nanocrystals. *Angew. Chem. Int. Ed.* **2004,** *43* (28), 3673.

(49) Song, H.; Kim, F.; Connor, S.; Somorjai, G. A.; Yang, P. Pt nanocrystals: shape control and Langmuir-Blodgett monolayer formation. *J. Phys. Chem. B* **2005,** *109*, 188.

(50) Hazewindus, N. W. f.

(51) Yost, R. A.; Enke, C. G. Triple quadrupole mass spectrometry for direct mixture analysis and structure elucidation. *Anal. Chem.* **1979,** *51* (12), 1251.

(52) von Issendorff, B.; Palmer, R. E. A new high transmission infinite range mass selector for cluster and nanoparticle beams. *Rev. Sci. Instrum.* **1999,** *70* (12), 4497.

(53) Lee, S.; Fan, C.; Wu, T.; Anderson, S. L. CO Oxidation on Au_n/TiO_2 Catalysts Produced by Size-Selected Cluster Deposition. *J. Am. Chem. Soc.* **2004,** *126* (18), 5682.

(54) Lopez-Acevedo, O.; Kacprzak, K. A.; Akola, J.; Hakkinen, H. Quantum size effects in ambient CO oxidation catalysed by ligand-protected gold clusters. *Nat. Chem.* **2010,** *2* (4), 329.

(55) Nikolaev, S. A.; Smirnov, V. V. Synergistic and size effects in selective hydrogenation of alkynes on gold nanocomposites. *Catal. Today* **2009,** *147*, S336.

(56) Niu, Y.; Yeung, L. K.; Crooks, R. M. Size-selective hydrogenation of olefins by dendrimer-encapsulated palladium nanoparticles. *J. Am. Chem. Soc.* **2001,** *123*, 6840.

(57) Semagina, N.; Renken, A.; Kiwi-Minsker, L. Palladium nanoparticle size effect in 1-hexyne selective hydrogenation. *J. Phys. Chem. C* **2007,** *111*, 13933.

(58) Reske, R.; Mistry, H.; Behafarid, F.; Roldan Cuenya, B.; Strasser, P. Particle size effects in the catalytic electroreduction of CO_2 on Cu nanoparticles. *J. Am. Chem. Soc.* **2014,** *136* (19),

6978.

(59) Taketoshi, A.; Haruta, M. Size- and structure-specificity in catalysis by gold clusters. *Chem. Lett.* **2014,** *43* (4), 380.

(60) Mistry, H.; Reske, R.; Zeng, Z.; Zhao, Z. J.; Greeley, J.; Strasser, P.; Cuenya, B. R. Exceptional size-dependent activity enhancement in the electroreduction of CO_2 over Au nanoparticles. *J. Am. Chem. Soc.* **2014,** *136* (47), 16473.

(61) Zaleska-Medynska, A.; Marchelek, M.; Diak, M.; Grabowska, E. Noble metal-based bimetallic nanoparticles: the effect of the structure on the optical, catalytic and photocatalytic properties. *Adv. Colloid Interface Sci.* **2016,** *229*, 80.

(62) Binnig, G.; Quate, C. F.; Gerber, C. Atomic force microscope. *Phys. Rev. Lett.* **1986,** *56* (9), 930.

(63) Binnig, G.; Rohrer, H. Scanning tunneling microscopy. *Surf. Sci.* **1983,** *126*, 236.

(64) Mcmullan, D. Scanning electron microscopy 1928–1965. *Scanning* **1994,** *17*, 175.

(65) Williams, D. B.; Carter, C. B., *Transmission electron microscopy: A textbook for materials science*. Springer US: 2009.

(66) Dierker, S. B.; Pindak, R.; Fleming, R. M.; Robinson, I. K.; Berman, L. X-Ray photon correlation spectroscopy study of Brownian motion of gold colloids in glycerol. *Phys. Rev. Lett.* **1995,** *75* (3), 449.

(67) Wang, Z. W.; Palmer, R. E. Intensity calibration and atomic imaging of size-selected Au and Pd clusters in aberration-corrected HAADF-STEM. *J. Phys: Conf. Ser.* **2012,** *371*, 012010.

(68) Pennycook, S. J.; Jesson, D. E. High-resolution Z-contrast imaging of crystals. *Ultramicroscopy* **1991,** *37*, 14.

(69) Pennycook, S. J. Z-contrast STEM for materials science. *Ultramicroscopy* **1989,** *30*, 58.

(70) Wang, Z. W.; Palmer, R. E. Determination of the ground-state atomic structures of size-selected au nanoclusters by electron-beam-induced transformation. *Phys. Rev. Lett.* **2012,** *108* (24), 245502.

(71) Mackay, A. L. A dense non-crystallographic packing of equal spheres. *Acta Cryst.* **1962,** *15*, 916.

(72) Ferrando, R.; Jellinek, J.; Johnston, R. L. Nanoalloys: From theory to applications of alloy clusters and nanoparticles. *Chem. Rev.* **2008,** *108*, 845.

(73) Wang, J. X.; Inada, H.; Wu, L.; Zhu, Y.; Choi, Y.; Liu, P.; Zhou, W. P.; Adzic, R. R. Oxygen reduction on well-defined core-shell nanocatalysts: particle size, facet, and Pt shell thickness effects. *J. Am. Chem. Soc.* **2009,** *131*, 17298.

(74) Najafishirtari, S.; Brescia, R.; Guardia, P.; Marras, S.; Manna, L.; Colombo, M. Nanoscale transformations of alumina-supported AuCu ordered phase nanocrystals and their activity in CO oxidation. *ACS Catal.* **2015,** *5* (4), 2154.

(75) Ferrer, D.; Torres-Castro, A.; Gao, X.; Sepulveda-Guzman, S.; Ortiz-Mendez, U.; Jose-Yacaman, M. Three-layer core/shell structure in Au-Pd bimetallic nanoparticles. *Nano Lett.* **2017,** *7*, 1701.

(76) Belić, D.; Chantry, R. L.; Li, Z. Y.; Brown, S. A. Ag-Au nanoclusters: Structure and phase segregation. *Appl. Phys. Lett.* **2011,** *99* (17), 171914.

(77) Yin, F.; Wang, Z. W.; Palmer, R. E. Controlled formation of mass-selected Cu-Au core-shell cluster beams. *J. Am. Chem. Soc.* **2011,** *133* (27), 10325.

(78) Deng, J.; Ren, P.; Deng, D.; Yu, L.; Yang, F.; Bao, X. Highly active and durable non-

precious-metal catalysts encapsulated in carbon nanotubes for hydrogen evolution reaction. *Energy Environ. Sci.* **2014,** *7* (6), 1919.

(79) Wang, N.; Sun, Q.; Bai, R.; Li, X.; Guo, G.; Yu, J. In situ confinement of ultrasmall Pd clusters within nanosized silicalite-1 zeolite for highly efficient catalysis of hydrogen generation. *J. Am. Chem. Soc.* **2016,** *138* (24), 7484.

(80) Collins, J. A.; Xirouchaki, C.; Palmer, R. E.; Heath, J. K.; Jones, C. H. Clusters for biology: immobilization of proteins by size-selected metal clusters. *Appl. Surf. Sci.* **2004,** *226* (1-3), 197.

(81) Palmer, R. E.; Leung, C. Immobilisation of proteins by atomic clusters on surfaces. *Trends Biotechnol.* **2007,** *25* (2), 48.

(82) Shahzad, N.; Chen, F.; He, L.; Li, W.; Wang, H. Silver–copper nanoalloys-an efficient sensitizer for metal-cluster-sensitized solar cells delivering stable current and high open circuit voltage. *J. Power Sources* **2015,** *294*, 609.

(83) Chakraborty, I.; Pradeep, T. Atomically precise clusters of noble metals: emerging link between atoms and nanoparticles. *Chem. Rev.* **2017,** *117* (12), 8208.

(84) Yoon, B.; Hakkinen, H.; Landman, U.; Worz, A. S.; Antonietti, J. M.; Abbet, S.; Judai, K.; Heiz, U. Charging effects on bonding and catalyzed oxidation of CO on Au_8 clusters on MgO. *Science* **2005,** *307*, 403.

(85) Molina, L.; Hammer, B. The activity of the tetrahedral Au_{20} cluster: charging and impurity effects. *J. Catal.* **2005,** *233* (2), 399.

(86) Cox, D. M.; Reichmann, K. C.; Trevor, D. J.; Kaldor, A. CO chemisorption on free gas phase metal clusters. *J. Chem. Phys.* **1988,** *88* (1), 111.

(87) Zhai, H. J.; Wang, L. S. Chemisorption sites of CO on small gold clusters and transitions

from chemisorption to physisorption. *J. Chem. Phys.* **2005,** *122* (5), 51101.

(88) Schmidt, M.; Masson, A.; Brechignac, C. Oxygen and silver clusters: transition from chemisorption to oxidation. *Phys. Rev. Lett.* **2003,** *91* (24), 243401.

(89) Molina, L. M.; Hammer, B. Oxygen adsorption at anionic free and supported Au clusters. *J. Chem. Phys.* **2005,** *123* (16), 161104.

(90) Kaldor, A.; Cox, D. M. Hydrogen chemisorption on gas-phase transition-metal clusters. *J. Chem. Soc., Faraday Trans.* **1900,** *86* (13), 2459.

(91) Richtsmeier, S. C.; Parks, E. K.; Liu, K.; Pobo, L. G.; Riley, S. J. Gas phase reactions of iron clusters with hydrogen. I. Kinetics. *J. Chem. Phys.* **1985,** *82* (8), 3659.

(92) Wallace, W. T.; Whetten, R. L. Coadsorption of CO and O_2 on selected gold clusters: evidence for efficient room-temperature CO_2 generation. *J. Am. Chem. Soc.* **2002,** *124*, 7499.

(93) Socaciu, L. D.; Hagen, J.; Bernhardt, T. M.; Woste, L.; Heiz, U.; Hakkinen, H.; Landman, U. Catalytic CO oxidation by free Au_2^-: experiment and theory. *J. Am. Chem. Soc.* **2003,** *125*, 10437.

(94) Lang, S. M.; Bernhardt, T. M.; Barnett, R. N.; Landman, U. Methane activation and catalytic ethylene formation on free Au_2^+. *Angew. Chem. Int. Ed.* **2010,** *49* (5), 980.

(95) Xie, Y.; Dong, F.; Bernstein, E. R. Experimental and theory studies of the oxidation reaction of neutral gold carbonyl clusters in the gas phase. *Catal. Today* **2011,** *177* (1), 64.

(96) Sanchez, A.; Abbet, S.; Heiz, U.; Schneider, W.-D.; Hakkinen, H.; Barnett, R. N.; Landman, U. When gold is not noble: Nanoscale gold catalysts. *J. Phys. Chem. A* **1999,** *103* 9573.

(97) Abbet, S.; Sanchez, A.; Heiz, U.; Schneider, W.-D.; Ferrari, A. M.; Pacchioni, G.; Rosch, N. Acetylene cyclotrimerization on supported size-selected Pd_n clusters ($1 \leqslant n \leqslant 30$): One atom

is enough! *J. Am. Chem. Soc.* **2000,** *122*, 3453.

(98) Bonanni, S.; Ait-Mansour, K.; Harbich, W.; Brune, H. Effect of the TiO_2 reduction state on the catalytic CO oxidation on deposited size-selected Pt clusters. *J. Am. Chem. Soc.* **2012,** *134* (7), 3445.

(99) Vajda, S.; Lee, S.; Sell, K.; Barke, I.; Kleibert, A.; von Oeynhausen, V.; Meiwes-Broer, K. H.; Rodriguez, A. F.; Elam, J. W.; Pellin, M. M.; Lee, B.; Seifert, S.; Winans, R. E. Combined temperature-programmed reaction and in situ x-ray scattering studies of size-selected silver clusters under realistic reaction conditions in the epoxidation of propene. *J. Chem. Phys.* **2009,** *131* (12), 121104.

(100) J. Zhao; L. Cao; R. E. Palmer; K. Nordlund; Djurabekova, F. Formation and emission mechanisms of Ag nanoclusters in the Ar matrix assembly cluster source. *Phys. Rev. Materials* **2017,** *1*, 066002.

(101) Henriksen, T. R.; Olsen, J. L.; Vesborg, P.; Chorkendorff, I.; Hansen, O. Highly sensitive silicon microreactor for catalyst testing. *Rev. Sci. Instrum.* **2009,** *80* (12), 124101.

(102) Andersen, T.; Jensen, R.; Christensen, M. K.; Pedersen, T.; Hansen, O.; Chorkendorff, I. High mass resolution time of flight mass spectrometer for measuring products in heterogeneous catalysis in highly sensitive microreactors. *Rev. Sci. Instrum.* **2012,** *83* (7), 075105.

(103) Sadakiyo, M.; Heima, M.; Yamamoto, T.; Matsumura, S.; Matsuura, M.; Sugimoto, S.; Kato, K.; Takata, M.; Yamauchi, M. Preparation of solid-solution type Fe-Co nanoalloys by synchronous deposition of Fe and Co using dual arc plasma guns. *Dalton Trans.* **2015,** *44* (36), 15764.

CHAPTER 2

Experimental Methods

In this chapter, all the experimental methods, instruments and techniques that were used in this research are introduced. Two types of cluster beam source were employed to deposit cluster catalysts (clusters on powder supports) in vacuum. Their catalytic activities were investigated by a liquid-phase reaction (4-nitrophenol reduction to 4-aminophenol by sodium borohydride) and a vapour-phase reaction (1-pentyne selective hydrogenation to 1-pentene). The atomic structure of the synthesized catalysts, and the cluster size evolution due to the reactions were explored by Spherical Aberration-Corrected Scanning Transmission Electron Microscopy (C_s-STEM) coupled with Energy Dispersive X-ray Spectroscopy (EDS), and corelated with their catalytic behaviours. The conception of the MACS was proposed by Richard Palmer and the cluster source used was modified by William Terry and Shane Murphy. I was involved in the instrument installation, calibration and development. Jian Liu provided training on the STEM and EDS. Peter Ellis and Christopher Brown gave instructions on the catalysis measurements.

2.1 Cluster production

The cluster beam technique is becoming an important method to deposit clusters on supports in vacuum. In contrast to the traditional chemical methods, clusters are formed in the gas phase in a high-vacuum chamber before deposition, which allows the production of naked (non-ligated) and clean (largely uncontaminated) clusters. For most of the catalytic reactions, the active sites are associated with the atoms on the cluster's surface. So clusters produced in vacuum may be expected to exhibit different catalytic behaviours due to the extremely clean surface compared with the clusters made by chemical methods.

2.1.1 Magnetron sputtering gas condensation cluster source

In this research, one type of cluster beam source, a magnetron sputtering, gas condensation cluster source, was used to produce and deposit Au/Cu nanoalloy cluster catalysts. The system was developed in a joint project between the University of Birmingham, Teer Coatings Ltd and Inanovate Ltd and embodied the design of the cluster source and mass filter developed in Birmingham.[1] The typical cluster flux coming from this system is around several ten nano amperes measured from the deposition cup without size-selection (most of the clusters are singly charged), equivalent to several ten micrograms of Au_{100} clusters per hour. The configuration of the system is similar to that of the Birmingham source, but the cluster flux is ~100 times higher, since the time of flight mass filter is only used to monitor the cluster size distribution instead of selecting clusters with particular sizes. The enhanced cluster flux makes it possible to directly measure the catalytic properties of the produced cluster catalysts under realistic reaction conditions.

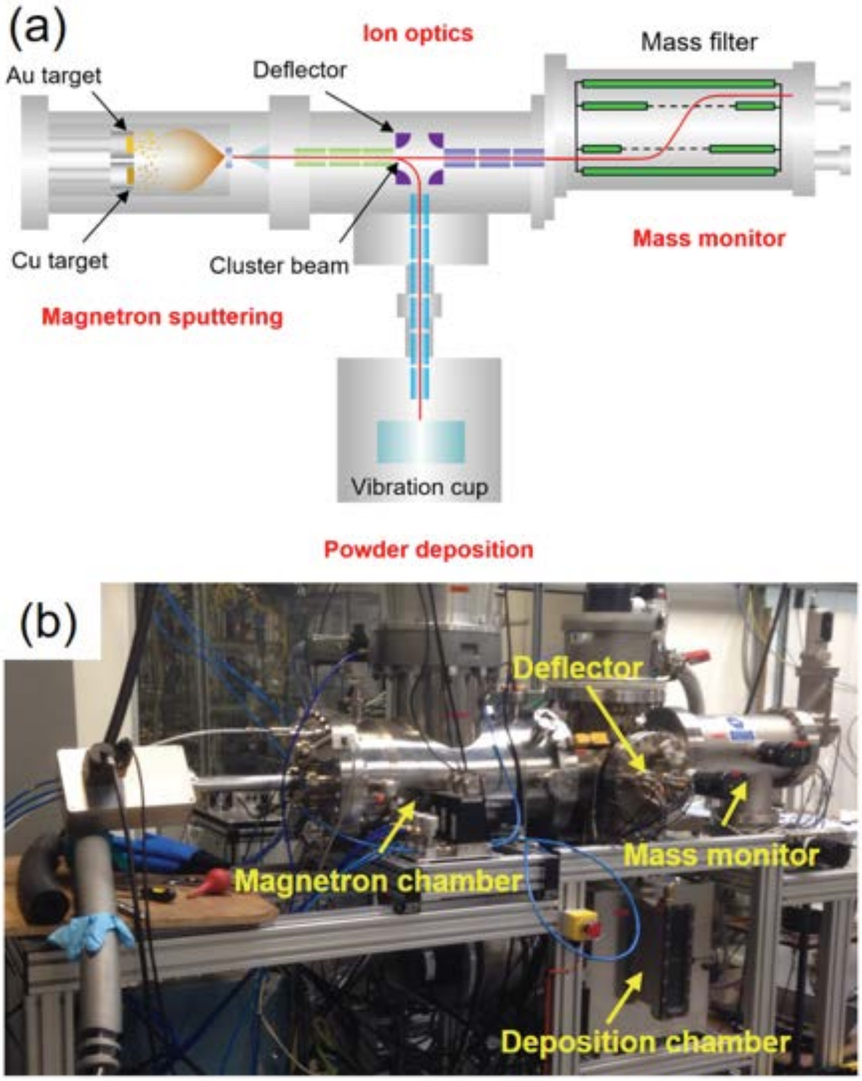

Figure 2.1 (a) Schematic diagram of the magnetron sputtering gas condensation cluster source with dual targets. The system consists of four parts: magnetron sputtering, ion optics, mass monitor and powder deposition. The sputtered single atoms condensed together to form clusters (~60% are charged) with the help of cooling agents (Ar and He gas) in the condensation chamber. The positively charged clusters are then extracted and further focused by a series of ion optics. An "octosphere" deflector is employed to control the flight direction of the focused cluster beam, which can be either transmitted to the mass filter for mass measurements or be bent 90 degrees towards the bottom chamber for deposition. The powder supports are agitated in a vibration cup to maximize the exposure under the cluster beam. (b) Photograph of the magnetron sputtering cluster source at Teer Coatings Ltd.

The schematic diagram and photograph of the system in Teer Coatings Ltd are shown in **Figure 2.1** (a) and (b), respectively. The system consists of four parts: magnetron sputtering, ion optics (with a beam deflector), mass monitor and powder deposition, which are usually maintained with a base pressure in the middle range of 10^{-7} mbar. In the magnetron sputtering chamber a thermally-isolated condensation chamber is mounted which can be cooled by liquid nitrogen. Within this condensation chamber, two magnetrons are mounted in parallel and controlled separately to tune the cluster composition. Magnetron sputtering is used to vaporize cluster materials from the sputtering target. Behind the target, two permanent magnets (one circular and one cylindrical) are arranged in the configuration shown in **Figure 2.2** (a).[2] The sputtering agent (usually Ar gas) is fed through a small gap between the shield and the target. A direct current (DC) or radio frequency (RF) power is applied to the magnetron to provide a high voltage (~ 300 V) across the gap, which ignites the plasma. The minimum gap distance is determined by the electron mean free path (l_e) through the equation below:[3]

$$l_e = \frac{k_B T}{\sigma_C P} \tag{2.1}$$

where the k_B is the Boltzmann constant, T is the temperature, P is the pressure inside the chamber and σ_C is the collision cross section. Due to the magnetron field, the formed plasma is confined on the top of the target and keeps bombarding the surface. Consequently, numerous single atoms and small clusters are sputtered out. The sputtering rate depends on the sputtering power, the Ar gas pressure and the intrinsic sputtering yield of the target materials.

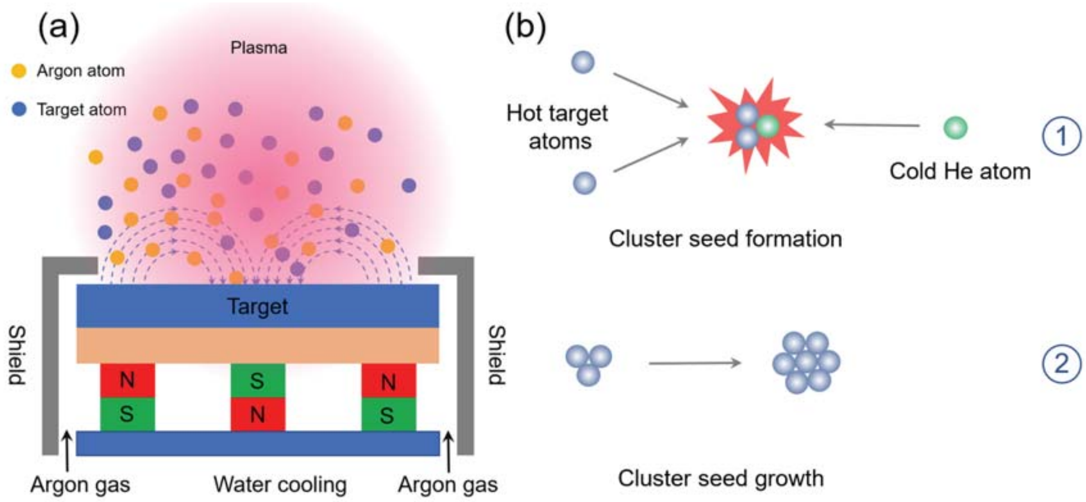

Figure 2.2 Principle of the magnetron sputtering (a), and cluster formation process (b). Reproduced from the reference [4].

After the magnetron sputtering process, the sputtered single atoms are sequentially cooled down and aggregated to form clusters with the help of cooling gases in the cold condensation chamber. In a previous study,[3] He gas was found to be more efficient at condensing clusters, whereas Ar gas was mainly responsible for sputtering. This conclusion was confirmed by the experiment that by adding 0.2 mbar He to 0.4 mbar Ar in the condensation chamber, the cluster size increased by 1000 times. Generally, the cluster growth process can be summarized in two steps as shown in **Figure 2.2** (b), formation of cluster "seeds" and growth of the seeds into large clusters.[5] Cluster seeds are formed by three-body collisions between two sputtered atoms and one He atom, where the He atom removes the excess kinetic energy from the sputtered hot atoms. It should be noted that the three-body collision happens more frequently with a high sputtering rate at a high Ar pressure, which provides a dense (supersaturated) vapor.[3]

After forming the cluster seeds, the seeds can further grow while moving toward the nozzle (exit of the condensation chamber) by two-body collisions, such as seed-seed collisions[6] and condensing vaporized atoms onto cluster seeds.[7] Therefore, the condensation length (distance between the magnetron target to the exit of the condensation chamber), size of the nozzle and He partial pressure can be used to control the cluster size distribution.

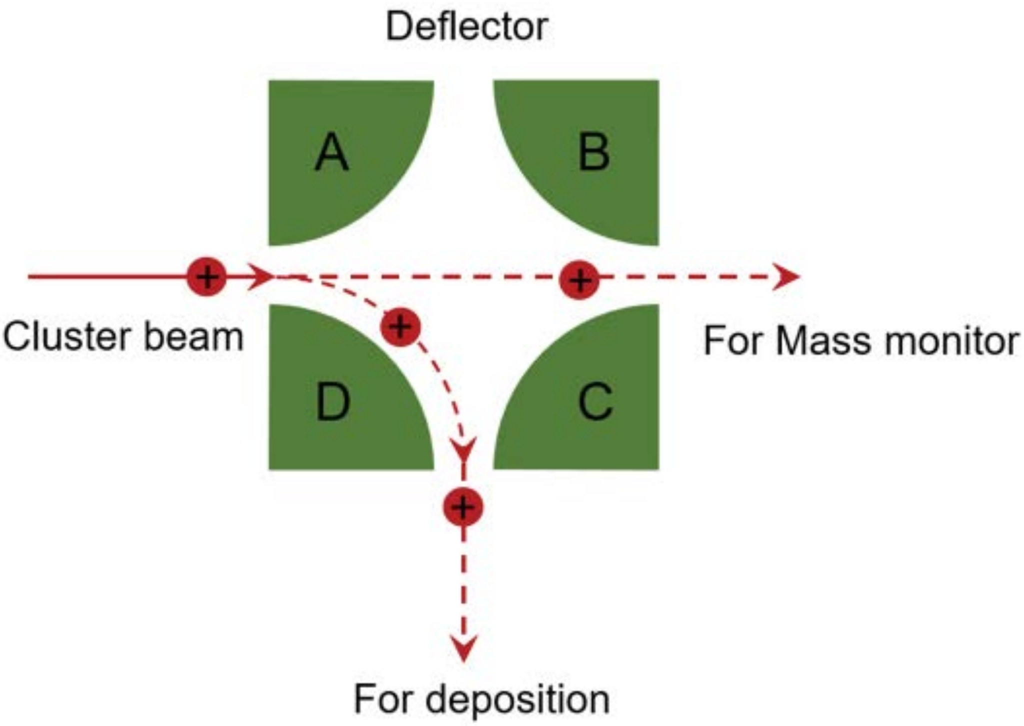

Figure 2.3 Schematic diagram of the "octosphere" deflector in side view, which consists of eight metal spheres. The flight direction of the cluster beam is controlled by the potential applied to the metal spheres.

Within the condensation chamber, a significant proportion (~ 30 %)[8] of the sputtering clusters are positively ionized due to the nature of the plasma sputtering, so no further ionization is needed. A negative potential (-500 to -1000 V) is usually applied to the skimmer in order to extract and accelerate the charged clusters coming from the nozzle. Only the central part of the cluster beam can pass through the skimmer to the ion optics chamber. In the ion optics chamber, the cluster beam is further focused by a set of ion optics lenses. After that, the cluster flight direction is controlled by a deflector known as the "octosphere" (invented in Birmingham), which consists of eight metal balls (could be simplified as four rods for demonstration, since the cluster beam is only deflected to one direction for deposition) as shown in **Figure 2.3**. The cluster beam can either fly directly to the mass filter to measure the cluster size distribution (no potential applied to the four "octospere" balls) or be bent 90 degrees towards the bottom for deposition (same negative potential applied to B/D and same positive potential applied to A/C).

The cluster size distribution is monitored in real time by a lateral time-of-flight mass filter.[9] **Figure 2.4** shows the schematic diagram, which consists of four metal plates forming two pairs of electrodes inside the chamber. From the bottom to the top, it can be divided into three sections: acceleration area, free fly area and deceleration area. In the acceleration area, a short electrical pulse is applied to the bottom plate to give an upward kinetic energy to the clusters. The clusters with different sizes gain the same upward kinetic energy and fly into the free flight area. When the clusters leave the free fly area to the deceleration area, a second electrical pulse with the same potential and duration but opposite direction is applied to the top plate to cancel the vertical movement of clusters. Because the time of the clusters travelling from acceleration area to deceleration area depends on their mass, cluster size selection can be eventually realized by changing the frequency of the applied electrical pulse (at given mass filter parameters). The mass of the exited clusters is given by equation[9] below:

$$m=\frac{eU_{\alpha}\alpha}{d_{1}hf^{2}} \tag{2.2}$$

Here, e is the elementary charge, U_α is the voltage on the bottom and top plates for acceleration and deceleration, α is a parameter to describe the pulse, d_1 is the vertical distance of the acceleration part, h is the cluster total vertical displacement, and f is the pulse frequency applied on the bottom and top plates. The resolution of the mass filter is determined by:

$$R=\frac{m}{\Delta m}=\frac{h}{\Delta h} \tag{2.3}$$

where the Δh is the dimension of the exit aperture. For our system, the vertical displacement h is 120 mm and the dimension of the exit aperture Δh is 5 mm, which give the mass resolution of 24. It should be noted that to achieve the theoretical resolution, the cluster beam should be focused very well.

Figure 2.5 shows typical mass spectra obtained during deposition of Au/Cu bimetallic clusters. It can be seen that without cooling the condensation chamber to liquid nitrogen temperature, large clusters cannot be obtained. Only single atoms and small clusters (dimer, trimer etc.) are observed when applying sputtering power to the Au and/or Cu targets. However, after cooling the system to liquid nitrogen temperature, the condensation rate is significantly enhanced. A broad mass distribution is observed both in making elemental clusters and binary clusters. The typical sputtering parameters are summarized in **Table 2.1**.

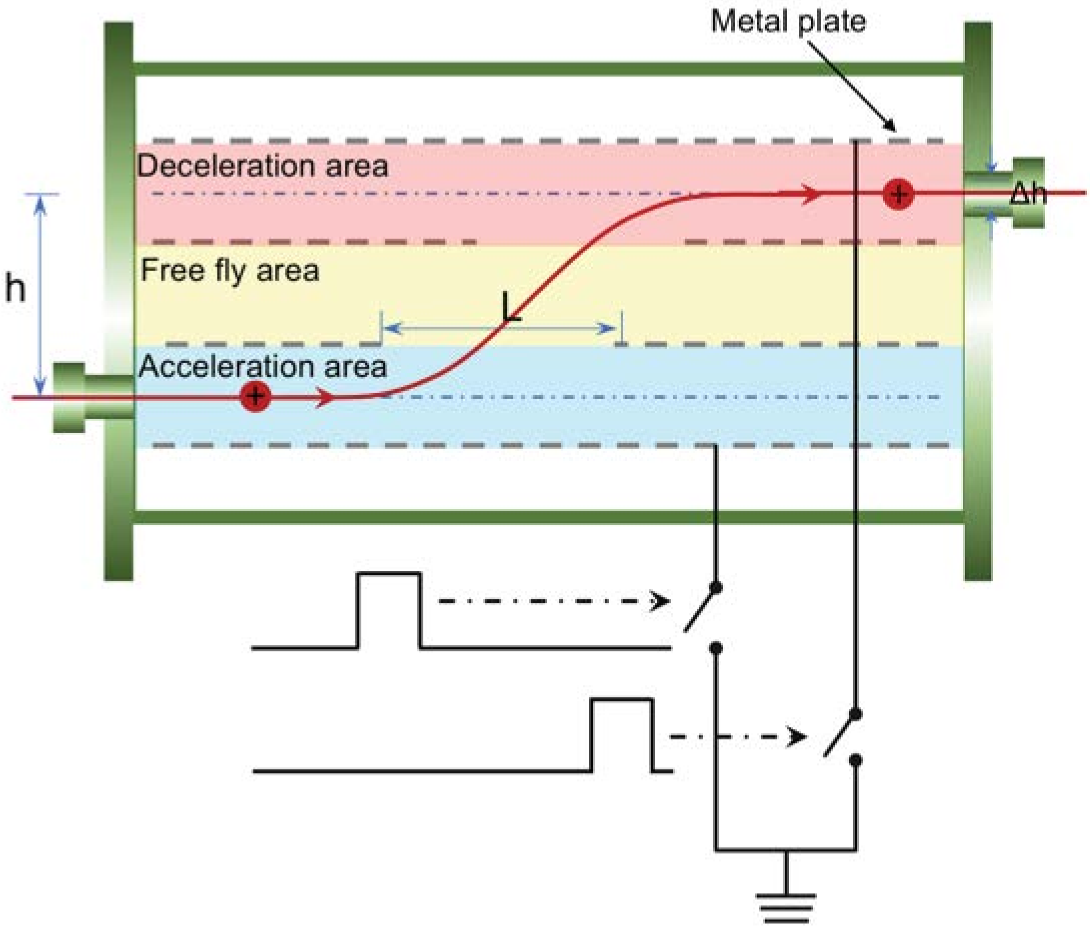

Figure 2.4 Schematic details of the lateral time-of-flight mass filter, which mainly consists of four metal plates forming two pairs of electrodes.[10] The whole chamber thus can be divided into three sections: acceleration area, free fly area and deceleration area. The size selection is realized by a series of voltage pulses applied to the bottom and top plates, which could cause a time delay for clusters traveling from the bottom to the top depending on the cluster mass. The resolution of the mass filter R is determined by the value of $\frac{h}{\Delta h}$. For the mass filter used in this research, the theoretical resolution is 24.

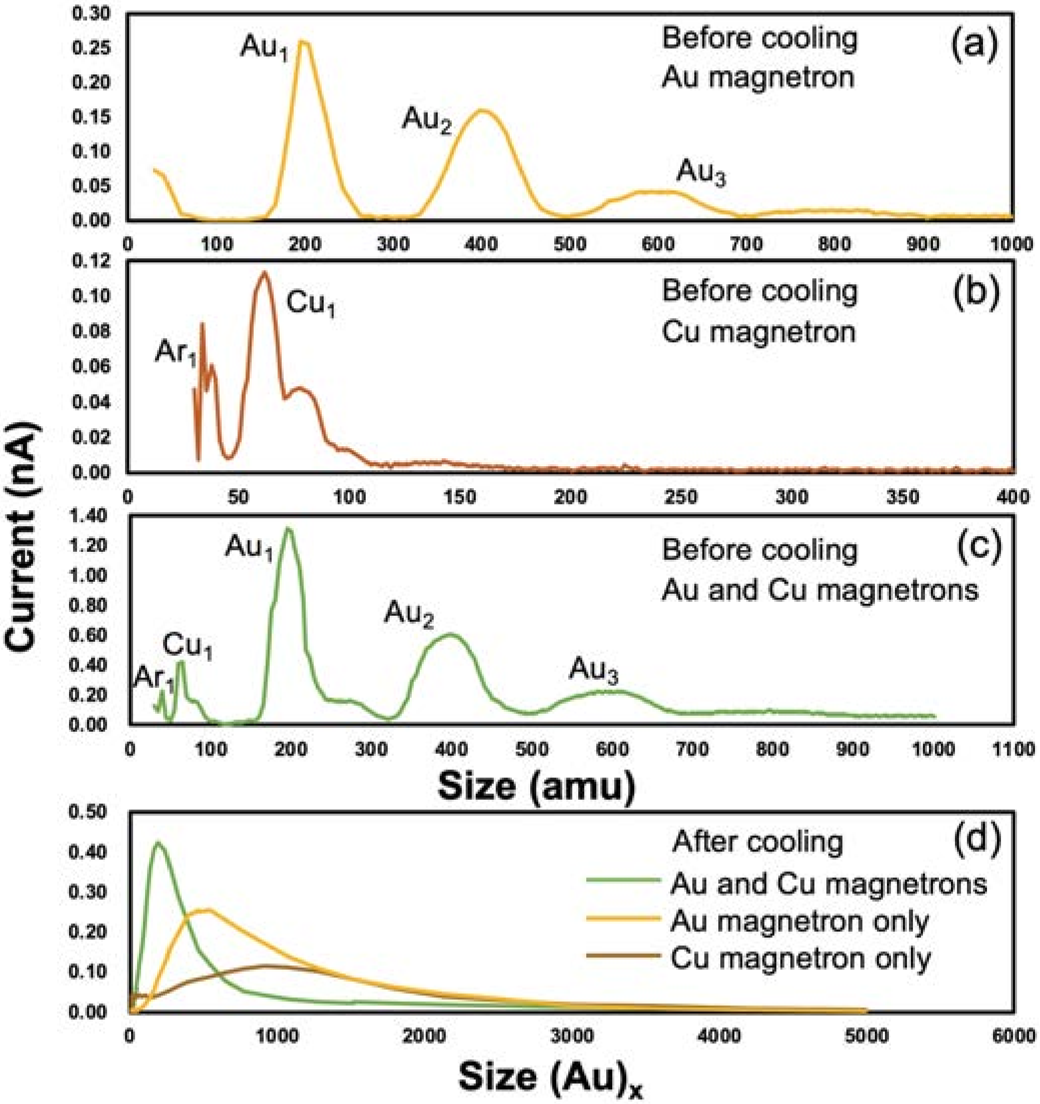

Figure 2.5 Typical mass spectra obtained during the cluster deposition. The condensation efficiency of the sputtered atoms is enhanced significantly by cooling the condensation chamber with liquid nitrogen.

After obtaining the desired cluster size distribution by properly tuning the sputtering and condensing parameters, the cluster beam is bent 90 degrees by the deflector towards bottom chamber for deposition. In this research, Au/Cu binary clusters were deposited onto MgO powders, which were contained in a vibration cup as shown in **Figure 2.6 (b)**. An unbalanced motor was attached on the bottom of the cup to agitate the powders during the deposition. To immobilize the clusters on the powder support, a high negative voltage (typically -1 kV) is applied to the vibration cup. However, it is still a big challenge to make sure all the powders are rolling evenly during the deposition, especially when they are charged by clusters. The typical deposition time for this experiment is about 8 hours per sample (0.8 g support powder), which gives a metal loading around 0.1wt% - 0.2wt% by inductively coupled plasma mass spectrometry (ICP-MS), depending on the cluster beam current.

Table 2.1 Typical sputtering parameters for preparation of Au/Cu clusters from magnetron sputtering cluster source

Sample	**Au/Cu binary cluster**	
Sputtering power	Au magnetron	6 W DC
	Cu magnetron	6 W DC
Condensation length	24 cm	
Nozzle size	3 - 5 mm	
Pressure in the condensation chamber	0.21 mbar	
Ar gas flow	100 sccm	
He gas flow	20 sccm	
Vibration cup potential	- 1 kV	
Skimmer potential	200 V	
Extractor Potential	500 V	
Beam Potential	600 V	
Cluster Beam Current	40-60 nA	

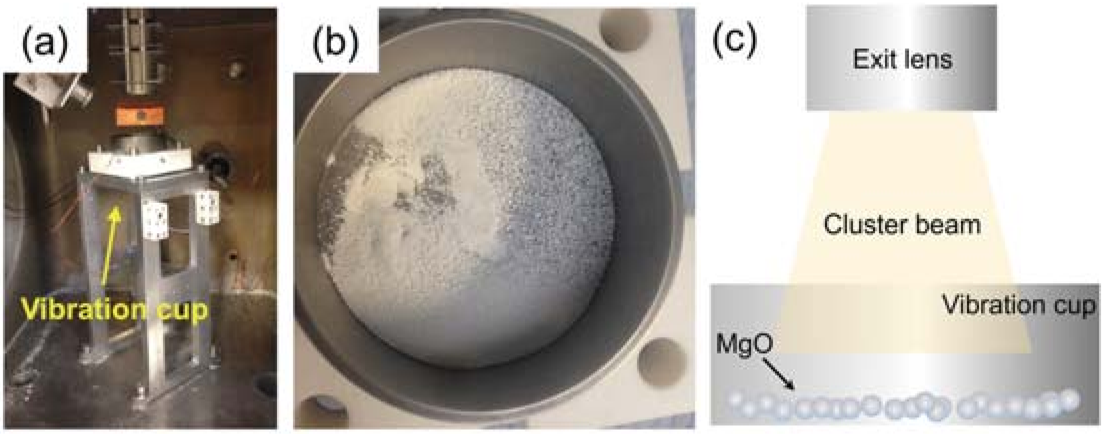

Figure 2.6 (a) and (b) Photograph of the deposition chamber inside and top view of the vibration cup with MgO powders loaded. (c) Schematic diagram of cluster deposition process. Powder supports are loaded in a vibration cup, which is agitated during the deposition to decorate clusters on the supports evenly.

2.1.2 Matrix Assembly Cluster Source

Although a magnetron sputtering gas condensation cluster source combined with a lateral time-of-flight mass filter can realize the deposition of size-selected clusters, its application in catalysis is limited by the low cluster flux. To overcome this bottleneck, a matrix assembly cluster source[11] was recently invented in our group, which has been demonstrated[1] to have the potential of increasing the cluster production rate by 5 orders of magnitude and can be further scaled up by using a more powerful sputtering source.

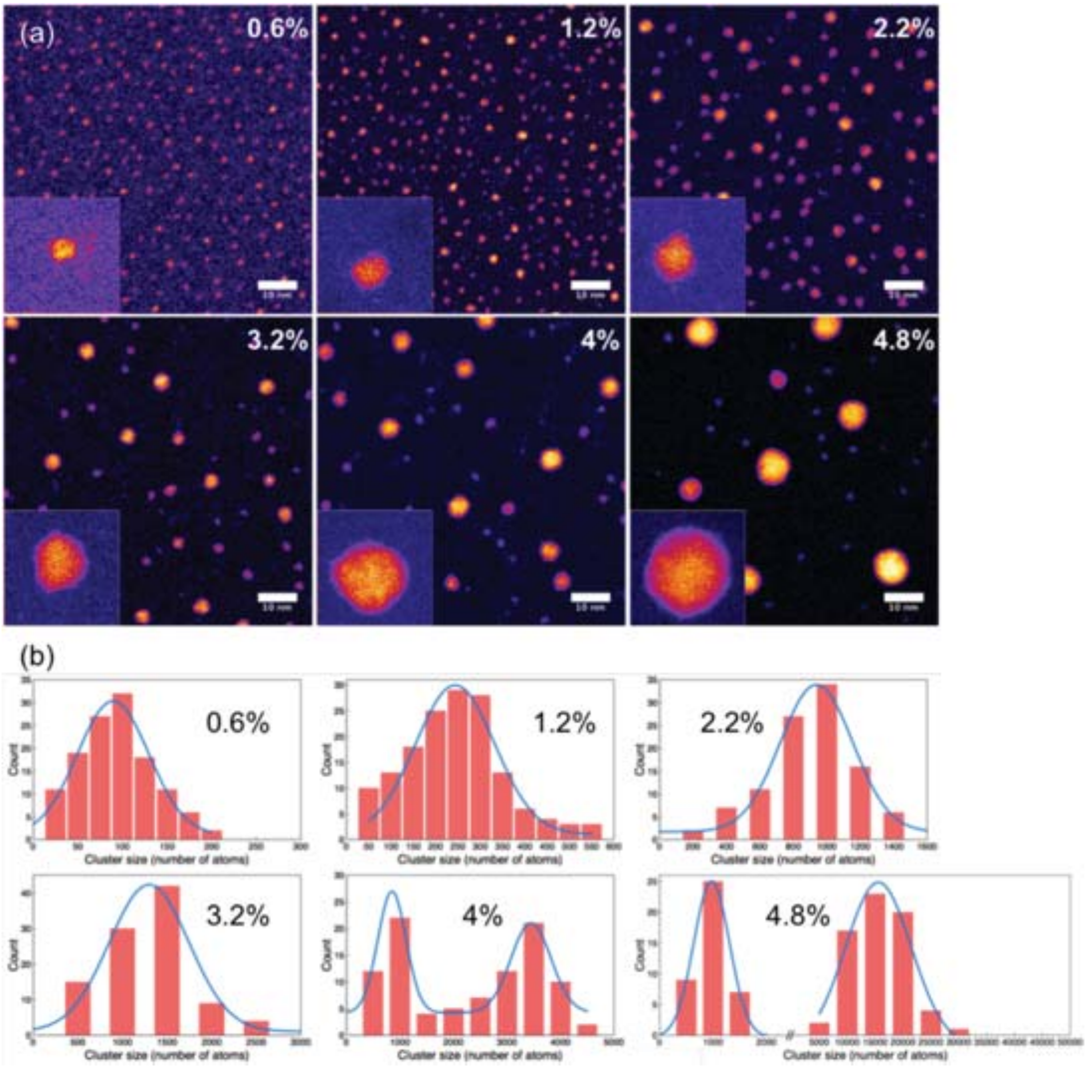

Figure 2.7 Cluster size control by tuning the metal concentration inside the matrix. (a) Typical HAADF images of the Ag clusters produced with metal concentration (atomic ratio) of 0.6%, 1.2%, 2.2%, 3.2% 4%, 4.8%, respectively. (b) Cluster size distribution histograms of the produced Ag clusters in (a).[12]

The traditional cluster beam techniques usually contain two types of mechanisms: (i) directly sputtering the target by ion beam; (ii) condensing the hot atoms generated from the sputtering,[13] thermal evaporation,[14] or laser ablation[15] etc. via inert gases. For the MACS, the mechanism is different, in that a cold solid matrix is firstly prepared on a cryogenically-cooled matrix support by co-condensing material atoms and noble gas atoms (Ar). The solid matrix can also be described as a solid Ar crystal film doped with metal atoms. Then an Ar ion beam is employed to generate a cascade of ion impacts in this solid matrix. During the ion sputtering process, the energy of the ions is transferred to the matrix. As a consequence, the metal atoms inside the matrix collide with each other, stick together, and aggregate to form clusters, which are eventually ejected by subsequent ion sputtering. A recent molecular dynamics study[16] found that the larger clusters are formed by successive ion collisions with the matrix. The clusters ripened in a dynamic environment in which each collision cascade causes a cluster already created by previous collisions to grow further. But eventually, the ripened cluster will be sputtered out of the matrix by an ion collision. Based on this idea, bimetallic or even trimetallic clusters can be easily produced by constructing a corresponding matrix. In addition, another advantage of the MACS over other traditional cluster sources is that the size of the clusters made with a MACS system can be controlled by the metal loading inside the matrix and the sputtering parameters such as ion energy, matrix temperature etc. An example of Ag cluster size control through regulating Ag metal loading in the matrix from a transmission mode is shown in **Figure 2.7**.[12]

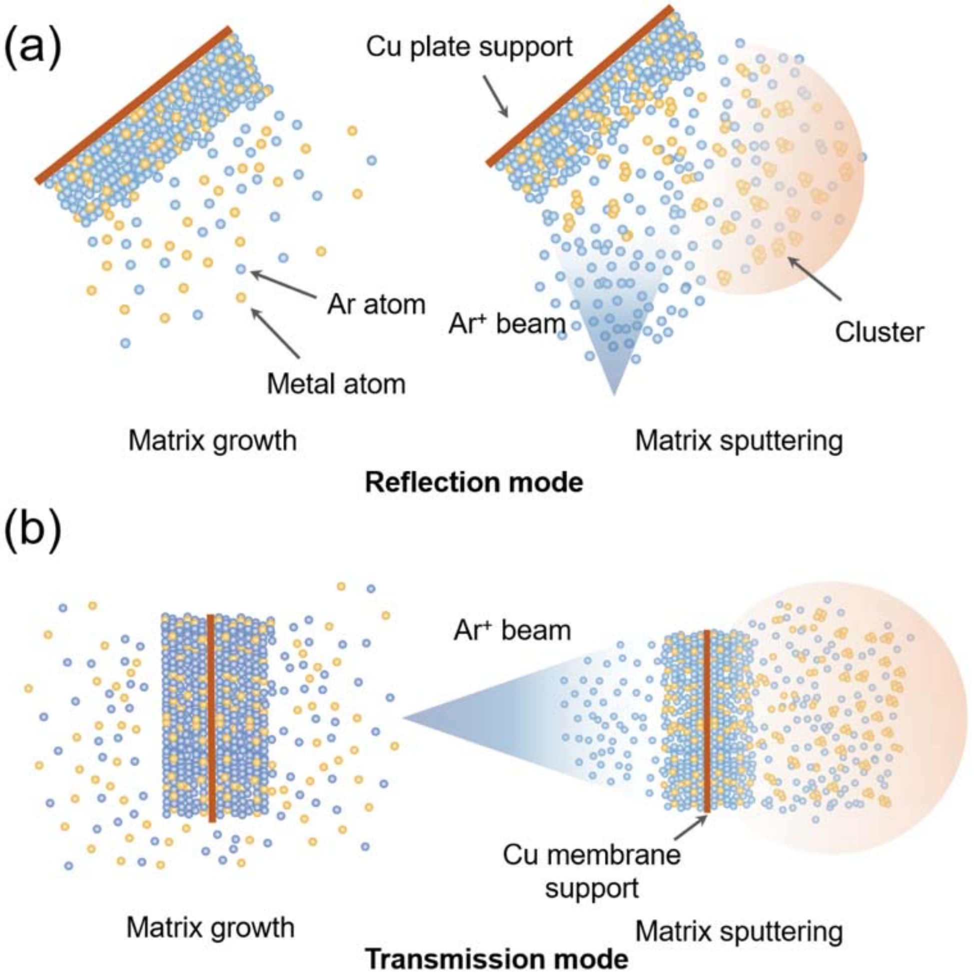

Figure 2.8 Schematic diagram of the principle for MACS. (a) reflection mode and (b) transmission mode. Metal atoms and Ar gas are first co-condensed on a support to form a solid matrix, which is then sputtered by an Ar ion beam. The impact of the ion beam initiates a cascade of collisions inside the matrix, causing clusters to nucleate, ripen and eventually be ejected from the matrix. In reflection mode, the matrix support is an oxygen-free copper plate, whereas in transmission mode, it is a copper membrane with dense holes (transparence: 17%).

At present, two different sputtering geometries, reflection mode and transmission mode, have been developed as shown in **Figure 2.8**. In reflection mode, an oxygen-free copper plate is used as the matrix support to condense the matrix, and the incident ion beam is perpendicular to the cluster beam emitted from the matrix. For transmission mode, a thin copper membrane with dense holes (hole dimension: 10 × 10 μm^2, transparency: 17%) is the matrix support. The clusters are collected at the back of the matrix support. However, considering the ion impact efficiency in reflection mode is much higher than that in transmission mode, the system used in this research to produce catalyst is operated in reflection mode. **Figure 2.9** shows the schematic diagram of the MACS system. The system consists of two chambers, matrix generation chamber and deposition chamber, which are maintained at a pressure in the mid-range of 10^{-8} mbar by two turbomolecular pumps backed by a rotary pump. In the matrix generation chamber, the matrix support is mounted on a cold finger cooled to below 20 K by a continuous liquid He flow. The matrix is prepared by depositing metal atoms onto the support from a thermal effusion cell and/or an e-beam evaporator (from both for making bimetallic clusters) while simultaneously introducing Ar gas into the chamber. After the matrix grows thick enough, the matrix support is moved into the deposition chamber for sputtering, where a sample carousel holds up to 21 glass slides (2.5 cm × 7.5 cm, each). The typical sputtering current used for this experiment is 15 - 30 μA with a beam energy of 1.5 keV. The cluster deposition time is 5-8 min per slide, which results in a cluster coverage of 10% - 20% on the support.

Since the MACS system I used is designed for depositing clusters onto planar surfaces, a dicing technique[17] was adopted to generate catalyst powders from cluster decorated planar support as shown in **Figure 2.10**. The lamellar carbon tapes (Mineral Seal Corporation) are chosen as the support since they are chemically inert for the reaction and easy to scratch off after dicing. Firstly, the carbon tape was cut mechanically by a diamond saw (DAD321 Automatic Dicer) with a cutting depth of 0.1 mm and cutting pitch of 1 mm to generate groves on the surface. The diced carbon tapes (on a glass slide) then stuck to the glass slides and were mounted in the carousel and pre-sputtered with an Ar^+ beam (current: ~10 µA, time: ~ 30 s) to generate defects on the surface to anchor clusters. After that, the clusters were deposited onto these diced carbon tapes with a typical deposition time of 8 min/slide, which ensured an appropriate cluster coverage of 10%-20%. After the deposition, the catalyst powders were obtained by scratching the topmost diced layer of the carbon tapes (see in **Figure 2.10**), which can be used for catalysis measurement directly.

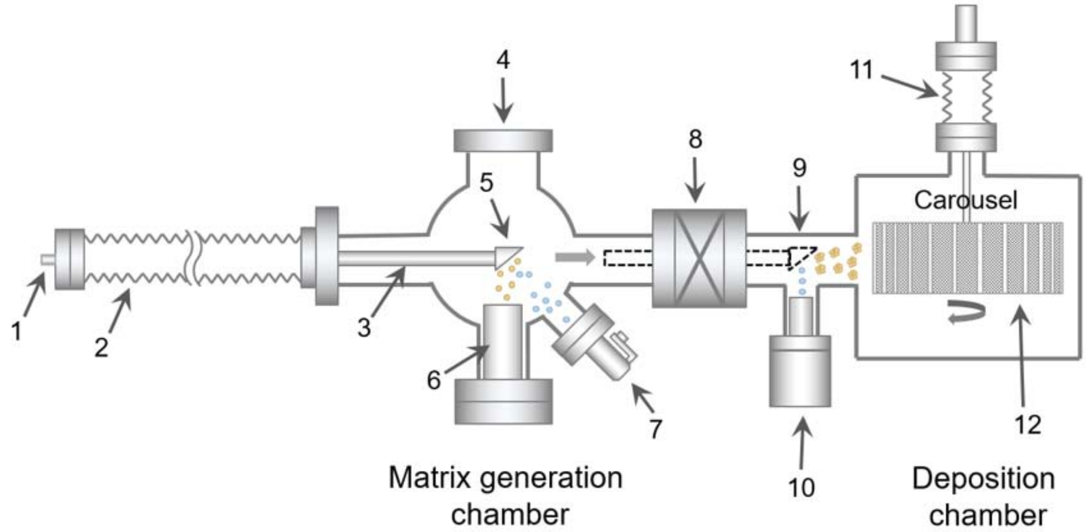

Figure 2.9 Schematic diagram of the MACS system with (1) liquid He and electrical feedthrough for coldfinger, (2) linear translator for (3) coldfinger, (4) pumping port for matrix chamber, (5) matrix support, (6) evaporator (another evaporator is shadowed by the port for gas leak valve), (7) Ar leak valve, (8) gate valve, (9) position of matrix during sputtering to produce nanoclusters, (10) ion source, (11) linear translator and rotary drive for (12) sample carousel.

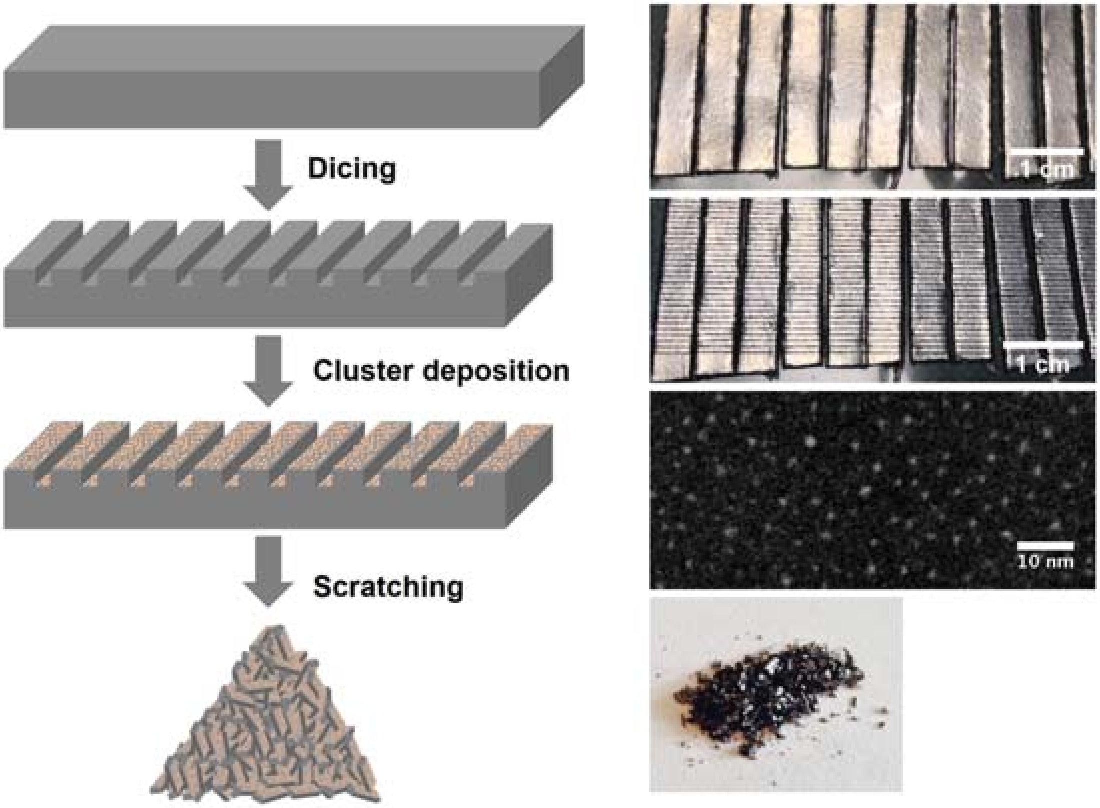

Figure 2.10 Schematic diagram of the dicing technique, which realizes the preparation of cluster catalysts from cluster decorated carbon tapes. The carbon tape supports are first diced mechanically to generate grooves on the surface. Then they are loaded on the carousel in MACS for cluster deposition. After the deposition, the topmost layer of the carbon tape is scratched off. The collected powders can be used as catalysts directly.

2.2 Scanning Transmission Electron Microscopy Characterization

2.2.1 Configuration of STEM

The atomic structure of all the cluster catalysts in this research were characterized by an Aberration Corrected STEM (JEOL 2100F) installed in Nanoscale Physics Research Laboratory, University of Birmingham as shown in **Figure 2.11**. It is composed of four most important parts, electron emission gun, electron optics (electromagnetic lenses), aberration correction and image collection.

The electron beam, used to resolve atomic structure is generated from a Schottky field emission gun (FEG), which consists of a sharp tungsten tip coated with a ZrO layer to reduce the work function barrier.[18] The emitted electrons are extracted and accelerated by another two anodes with total accelerating voltage of 200 kV. The whole electron gun is maintained in a high vacuum chamber (10^{-6} Pa) in order to avoid contamination and oxidation of the tip. After generating high energy electrons, the electrons are focused by a series of electromagnetic lenses to form an electron beam. In contrast to optical lenses, the strength of magnetic field for an electromagnetic lens can be easily controlled by the current in the lens coils, which is convenient for changing the magnification and imaging mode. Since the resolution of the STEM relates to the electron probe size, the focused electron beam is further adjusted by an aberration corrector (CEOS, GmbH) prior to reaching the sample. The aberration correction is achieved by constructing a “concave magnetic field” with the help of combination of hexapole lenses. The aberration corrected electron beam (spot size: ~0.1 nm) is used to scan and interact with the sample atoms, and eventually the atomic structure information is exhibited in the obtained images. For the transmitted electrons, the unscattered proportion is collected by a bright field (BF) detector or CCD camera to form BF images, whereas the electrons scattered by a large angle (e.g. > 50 mrad) are collected by an annular HAADF detector to form a HAADF-STEM image. In addition, the unscattered electrons can also be used to obtain electron energy loss spectra (EELS), which can provide composition information etc.

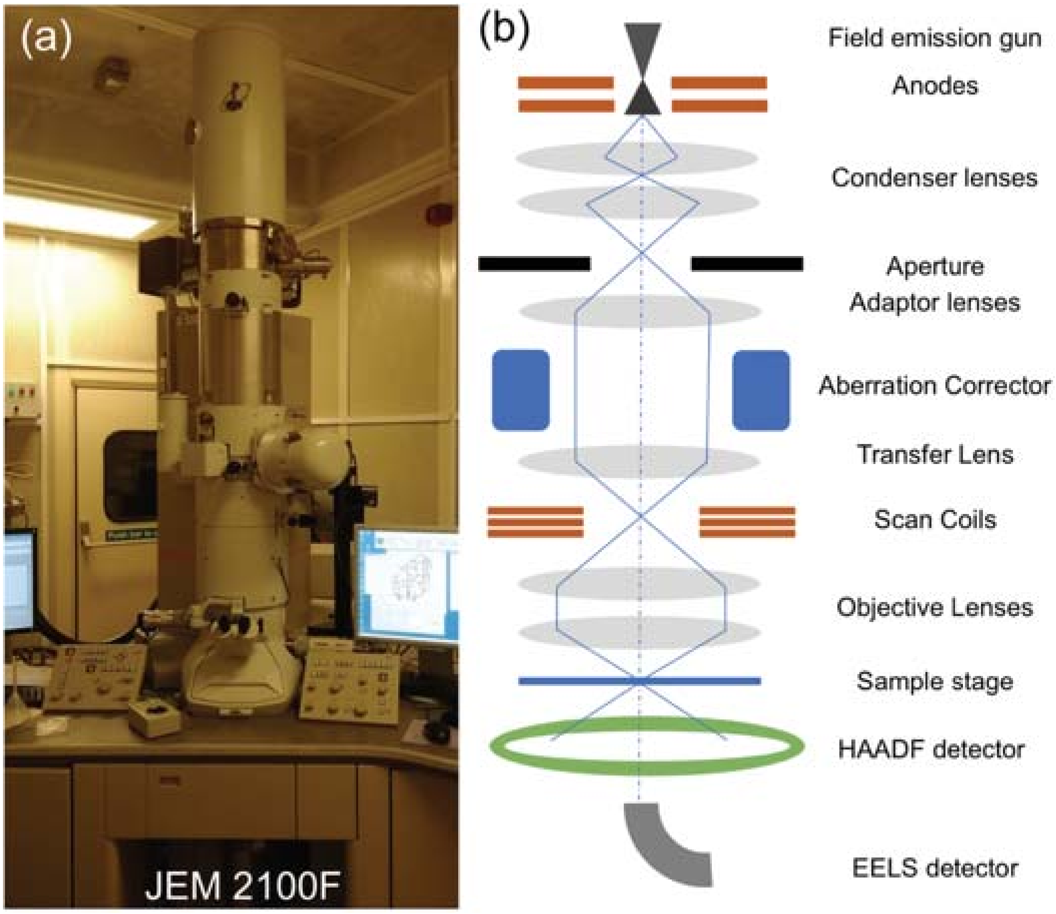

Figure 2.11 Photograph of JOEL JEM 2100F aberration corrected STEM in University of Birmingham (a) and schematic diagram of the internal structures (b).

2.2.2 Resolution and aberration correction

When it comes to a microscope, the most important information is the resolution. A microscope with a better resolution can provide much finer structure information of the object. The invention of the TEM pushes the resolution from the micrometer scale (optical microscopes) down to the nanometer scale, which makes it possible to see the arrangement of atoms in materials. Generally, for a lens (optical lens or electromagnetic lens) the minimum distance (*l*) that can be distinguished for two spots is derived by Rayleigh criterion:[19]

$$l = 1.22 \times \frac{\lambda}{\beta} \tag{2.4}$$

Where λ is the wavelength of the light (or electrons for electron lenses) and β is the collection angle. This equation illustrates that the resolution has the same order of magnitude as the wavelength. According to de Broglie theory,[20] the wavelength of an electron beam with energy of 200 keV is ~ 0.0025 nm, which indicates the resolution of the TEM should reach sub-Angstrom easily. However, the sub-Angstrom resolution was only achieved recently, after the invention of aberration correctors. The reason is that any lens is not perfect and the existence of the aberrations makes the practical resolution much worse than the theoretical value. There are several aberrations in an electromagnetic lens, but three of the most important ones are chromatic aberration, astigmatism and spherical aberration.[21]

Chromatic aberrations derive from the dispersion of electron energy (electron wavelength). Electrons of different energies are bent differently in the magnetic field, so the electromagnetic lens focuses the electrons at different positions. It happens more severely in a thermionic gun, but the electron monochromaticity for a field emission gun usually allows the chromatic aberrations to be neglected.

Astigmatism occurs because the convergent ability of electromagnetic lens is different for the electrons along different directions. It usually results from misalignment or the imperfect geometry of the electromagnetic lens leading to an asymmetric magnetic field along different directions. **Figure 2.12** shows a diagram of the origin of astigmatism. The lens focuses the electrons along the horizontal direction stronger than along vertical direction. As a result, the electrons are focused on the axis at two different positions, which cannot be adjusted by changing the focusing conditions. In TEM, the astigmatism could be easily corrected by providing compensating magnetic field from octupoles after electromagnetic lenses.[21]

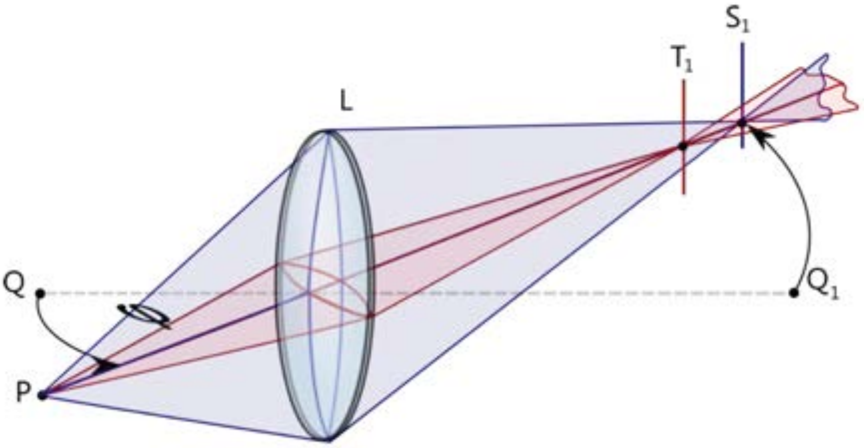

Figure 2.12 Diagram showing the origin of astigmatism.[22] Electrons from different axial directions are focused at different points.

Spherical aberration[23] occurs when the electromagnetic lens has different convergent abilities for on-axis electrons and off-axis electrons due to the inhomogeneous magnetic field inside the lens, which leads to forming a disk on the focal plane instead of a point (see **Figure 2.13**). For a positive spherical aberration (happens in convex lenses), the electrons striking close to the edge of the lens are bent more than those striking near the axis. For the negative spherical aberration (happens in concave lenses), the electrons near the axis are focused more than those close to the edge. The way to correct the spherical aberration is straightforward, combining lenses with positive spherical aberration and lenses with negative spherical aberration. In modern optical microscopes, the spherical aberration is corrected by placing a concave lens before or after the convex lens, so the beam can be re-converged to a point. In the electron microscope, all the round electromagnetic lenses are convex lenses and have positive spherical aberration. Their correction has recently been achieved by two methods (Nion and CEOS). In the Nion approach, multiple quadrupole and octupole lenses are used to construct a structure to diverge electrons, whereas in the CEOS approach, hexapole and transfer lenses are employed to realise the same function.[24] More detailed information can be found in reference [21].

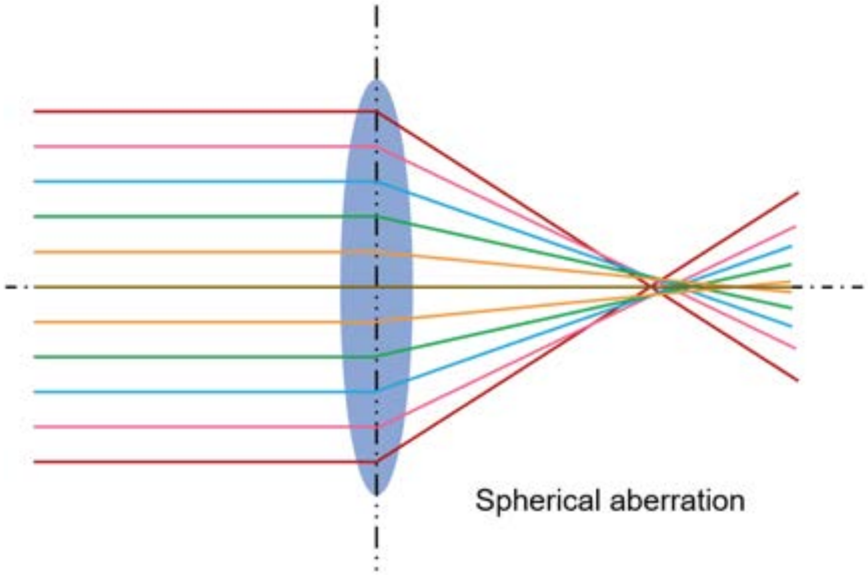

Figure 2.13 Diagram showing the origin of the spherical aberration. The lens focuses the on-axis and off-axis electrons at different points.

2.2.3 High Angle Annular Dark Field imaging

The HAADF imaging technique is the most used technique in STEM since it provides both atomic structure information and composition information (Z-contrast information). The principle of HAADF contrast is much easier to explain compared with phase-contrast in high-resolution TEM. When electrons passing through a thin sample, some of them can be scattered by an angle due to the interaction with the atomic electron cloud and nucleus, as shown in **Figure 2.14** (a). The scattered angle depends on the interaction with the nucleus, which decreases with increasing distance between incident direction and nucleus. The weakly scattered electrons preserve their phase coherence, which could be used to form electron diffraction and HRTEM images together with unscattered electrons. The highly scattered electrons (greater than 50 mrads) are typically used in HAADF mode,[25] which are usually explained by traditional Rutherford scattering theory.[26] The differential cross-section ($\sigma_R(\theta)$) for classic scattering can be described by

$$\sigma_R(\theta)=\frac{e^4Z^2}{16(4\pi\varepsilon_0E_0)^2}\frac{d\Omega}{\sin^4(\frac{\theta}{2})} \quad {}^{27} \tag{2.5}$$

where θ is the scattering angle as shown in **Figure 2.14** (b), Z is the atomic number, E_0 is the initial energy of the electron, Ω is the solid angle of scattering, and ε_0 is the dielectric constant. Therefore, it can be concluded that $\sigma_R(\theta)$ is proportional to Z^2 for a certain STEM. This is also the reason that HAADF images are also termed as “Z contrast” images. However, in reality, the power coefficient is usually less than 2 due to a number of factors such as detector geometry, electron screen effect and so on.[28] The final intensity relationship between two elements can be summarized as:

$$\frac{I_A}{I_B}=\left(\frac{Z_A}{Z_B}\right)^n \tag{2.6}$$

The coefficient n is usually calibrated with the standard size-selected clusters. For the STEM in our lab at the standard operating parameters, the coefficient is 1.46 ± 0.18. In this study, all the HAADF images are taken at the camera length of 10 cm and the HAADF detector is operated with inner angle of 62 mrad and outer angle of 164 mrad (200 kV).

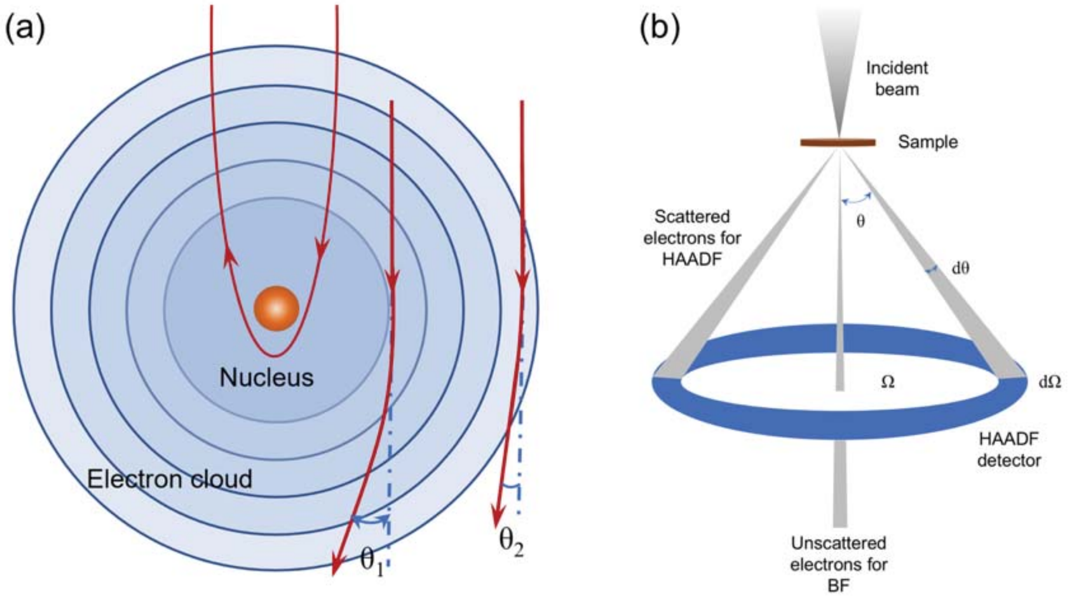

Figure 2.14 (a) Schematic diagram of electron beam elastically scattered by an atom nucleus. When electrons pass through a thin sample, some of them can be scattered by an angle due to the interaction with the atomic electron cloud and nucleus. The scattered angle decreases with increasing the distance between incident direction and nucleus. (b) Schematic diagram of HAADF imaging which collects highly scattered electrons to form "Z-contrast" images.[21]

2.2.4 Energy Dispersive X-ray spectroscopy

In STEM, another useful technique is EDS, where the characteristic X-ray is generated by the inner-shell excitation with incident electrons.[29] When the high-energy electron beam penetrates the inner shell of the atom, the electrons on the inner orbit can be kicked out by inelastic interactions, which excites the atom into an excited state. One way to stabilize the atom to the ground state is transiting the electron from outer-shell to the inner-shell vacancy which may result in the emission of the characteristic X-rays with the energy equivalent to the difference between the two energy levels, as shown in **Figure 2.15**. Because the energy peak of the characteristic X-ray is different for each element, it can be used to identify the element, and from the integrated peak intensity, the compound composition can also be quantified. Due to the emission probability of the characteristic X-rays increasing with the atomic number, the EDS technique is usually more sensitive to heavy elements. For quantitative analysis, the intensity (I) of the emitted characteristic X-rays from an element can be obtained by

$$I=\frac{A\sigma\omega p N_0 \rho M t \Omega \varepsilon}{4\pi N} \tag{2.7}$$

where A is the incident electron intensity, M is the content (mass ratio), σ is the ionisation cross section, t is the sample thickness, ω is the fluorescent yield factor, Ω is the detection angle, p is the proportion of the X-rays being analysed, ε is the detection factor, N_0 is the Avogadro's number, N is the atomic number and ρ is the density. Thus, the ratio between element A and B (C_A/C_B) can be derived from the equations below:

$$\frac{C_A}{C_B}=k_{AB}\left(\frac{I_A}{I_B}\right) \tag{2.8}$$

$$k_{AB}=\frac{\sigma_B \omega_B p_B \varepsilon_B N_A}{\sigma_A \omega_A p_A \varepsilon_A N_B} \tag{2.9}$$

The k_{AB} is a proportionality factor which has been calculated by the Cliff-Lorimer method[30] automatically in the software (BRUKER).

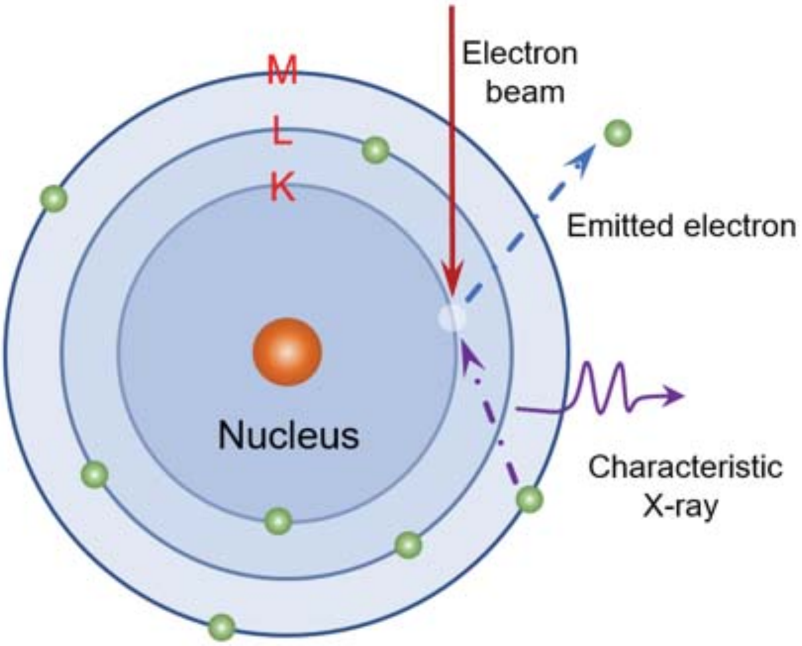

Figure 2.15 Schematic diagram of the principle of EDS. A high-energy electron beam penetrating the inner shell of an atom can kick out the electrons on the inner orbit, which may cause the emission of the characteristic X-rays. The energy of the emitted X-ray depends on the atomic number, which can be used to distinguish different elements.

2.2.5 STEM specimen preparation

The as-deposited clusters on the TEM grids can be directly imaged in HAADF-STEM without further treatments. However, for the powder samples (Au/Cu on MgO and Pd on carbon tape), the STEM specimens were prepared by dispersing a small amount of powder samples (< 1 mg) in DI water or ethanol (~1 ml) in a centrifuge tube followed by sonicating for 5-10 minutes. Then a drop taken from the top layer of the sonicated liquid was cast onto a TEM grid coated with an amorphous-carbon film. After that, the TEM grid was dried under an infrared lamb for 5-10 min to evaporate the solvent.

2.2.6 Estimation of the cluster mass from HAADF images

To compare the activities of the catalysts with different cluster loadings fairly, especially for the samples of a very low metal loading, we also estimated the cluster loading based on the HAADF images of the as-deposited clusters on the TEM grid. The HAADF images are processed by the Fiji software.[31] **Figure 2.16** shows an example of Pd clusters on a TEM grid. The HAADF image of as-deposited clusters is first filtered by a bandpass filter (the typical setting: filter larger structure down to 40 pixels and filter small structure up to 3 pixels) to remove noise and show the boundary more clearly, followed by picking clusters through adjusting the image threshold. After that, the individual 2D cluster area can be obtained by the software ("analyze particles" function) and summarized in a table. Since the clusters from MACS have low kinetic energy, most of them soft land on the TEM grid. If we assume the cluster has a spherical shape on the TEM grid, the total cluster mass per frame ($m_{/frame}$) can be acquired by the equations (2.10) and (2.11):

$$m_{/frame} = \sum_{0}^{n} \frac{4\pi\rho R_n^3}{3} \tag{2.10}$$

$$R = \left(\frac{S}{\pi}\right)^{0.5} \tag{2.11}$$

Where n, ρ, R and S are the cluster number, mass density of Pd, radius of individual cluster and the cluster projected 2D area, respectively. After measuring the total mass of the cluster catalyst from carbon tapes on 21 glass slides, the metal loading ($P_{loading}$) can be calculated by the equation (2.12).

$$P_{loading} = \frac{m_{/frame} \times S_{slide}}{m_{total} \times S_{frame}} \tag{2.12}$$

Here, S_{slide} and S_{frame} are the area of total 21 glass slides (21×75 cm×25 cm) and frame area of the HAADF image (39.35 nm×39.35 nm), respectively.

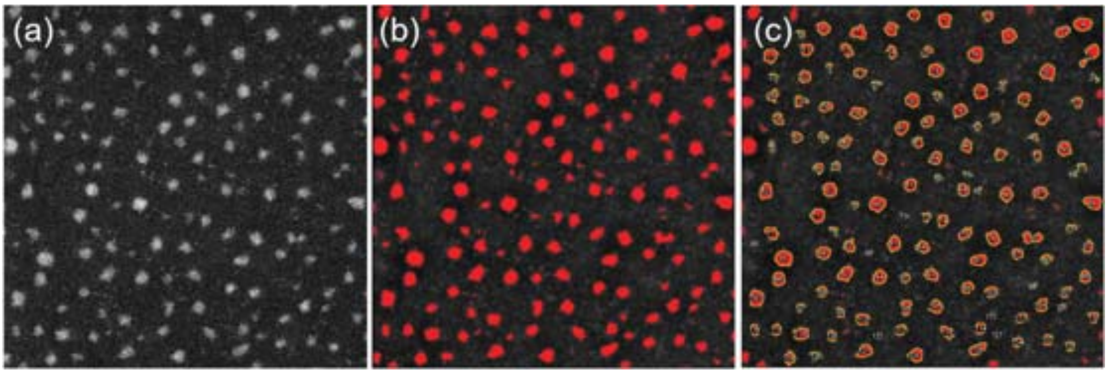

Figure 2.16 A demonstration of estimating cluster loading from HAADF images of as-deposited clusters. (Frame size: 39.35 nm×39.35 nm). (a) HAADF image of as deposited Pd clusters; (b) Filtered HAADF image (by a bandpass filter: filter larger structure down to 40 pixels and filter small structure up to 3 pixels), where clusters are picked out by red colour via adjusting the image threshold; (c) Processed HAADF image where the 2D cluster area is measured individually by the “Fiji” software.

2.3 Preparation of reference samples by chemical methods

The catalysts used in industry are usually produced by wet chemical methods, due to the high flexibility to tune the metal loading, especially for high loading catalysts. To compare the catalytic activity of physically produced cluster catalysts with chemically produced catalysts, small batches of reference samples were synthesized by the traditional impregnation method.[32]

2.3.1 Reference sample for nitrophenol reduction

In the experiment of 4-nitrophenol reduction over Au/Cu alloy cluster catalysts, Au_1Cu_1 on MgO powder (total mass metal loading: 1%) is chosen as the reference sample. Firstly, the pore volume of the MgO support (9.9 g) was carefully measured by adding deionized (DI) water until reaching the incipient wetness point, and following the change in mass during the addition. The amount of added DI water can be calculated easily. 0.088 g copper nitrate hemipentahydrate (Alfa Aesar) and 0.184 g tetrachloroauric acid solution (41.22 wt% Au, Johnson Matthey) were then dissolved in the same amount of DI water to fill the pores of the support and to give the desired concentration and ratio of metals in the final product. After that, the impregnation solution was added in the same amount of MgO support (9.9 g), and the mixture was stirred to give a wet solid which was equally impregnated throughout. The wet solid was dried at 100°C in a drying cabinet for three hours. After that, the dried powder was further treated at 250 ^{o}C in a 5% H_2/N_2 gas mixture in a tube furnace for four hours to remove the anion group from the metal salts.

2.3.2 Reference sample for 1-pentyne selective hydrogenation

For the selective hydrogenation of 1-pentyne experiment, Pd clusters on diced blank carbon tape with the mass metal nominal loading of 0.0006% is the reference sample. The blank carbon support was obtained through the above dicing technique without depositing clusters. Again, firstly the pore volume of the carbon tape powder support was carefully measured by adding DI water until reaching the incipient wetness point, and following the change in mass during the addition. 0.012 g palladium nitrate acid solution (Alfa Aesar) was diluted in the same amount of DI water to fill the pores of the carbon support and give the desired mass metal loading in the final product. The impregnation solution was then added into 1 g blank carbon support, and the mixture was stirred to give wet powders. After that, the wet powders were dried at 100°C in a drying cabinet for three hours, followed by treatment at 250°C in a 5% H_2/N_2 gas mixture at a tube furnace for four hours to remove the anion group from the palladium nitrate salt.

2.4 Catalytic activity measurements

The catalytic activities of physically deposited cluster catalysts were investigated via two kinds of reactions: (i) liquid-phase (4-nitrophenol reduction catalysed by Au/Cu alloy clusters on MgO support) and (ii) vapour-phase (selective 1-pentyne hydrogenation catalysed by Pd and Pd/Au clusters on diced carbon support). The experiments were carried out in the facilities of Johnson Matthey technology center.

2.4.1 Liquid-phase chemical reaction measurement

The liquid phase reduction of 4-nitrophenol was carried out in an open beaker at room temperature with $NaBH_4$ acting as the reductant. The reaction scheme is shown in **Figure 2.17**. The nitro group of nitrophenol is reduced by the hydrogen coming from the decomposition of $NaBH_4$ with the help of the metal catalysts. Studies show that the nitrophenol molecules are firstly adsorbed on the catalyst surface through the two oxygens of the nitro group. Then the reduction is realized by the cleavage of O-N bonds and addition of surface adsorbed hydrogen.[33-34]

The reaction solution was prepared by dissolving 1.67 mg (0.012 mol) of 4-nitrophenol (Sigma-Aldrich) and 18.92 mg (0.5 mol) of $NaBH_4$ (Sigma-Aldrich) in 200 ml DI water sequentially, which gave a 4-nitrophenol concentration of 0.06 mM and

$NaBH_4$ concentration of 2.5 mM. During the mixing process, the colour of the solution became yellow, which indicated 4-nitrophenol converted to 4-nitrophenolate.[35] For each test, 30 mg Au/Cu cluster catalyst was added to 50 ml of this solution and continuously magnetically stirred. The reaction solution is fresh and should be used within 4 hours due to the instability of $NaBH_4$. It has been found that the reaction solution exhibits a strong optical absorbance at 400 nm and the peak intensity is proportional to the concentration of the nitrophenol.[36] Therefore, after adding the catalyst, the optical absorbance of the reaction solution was recorded by a UV-VIS spectrophotometer (Agilent Technologies Cary Series) at intervals of 5 min to monitor the progress of the reaction. For each absorbance measurement, 2 ml of the analyte solution was filtered by a syringe filter to remove the catalyst and poured into a 1 cm^3 cuvette for measurement.

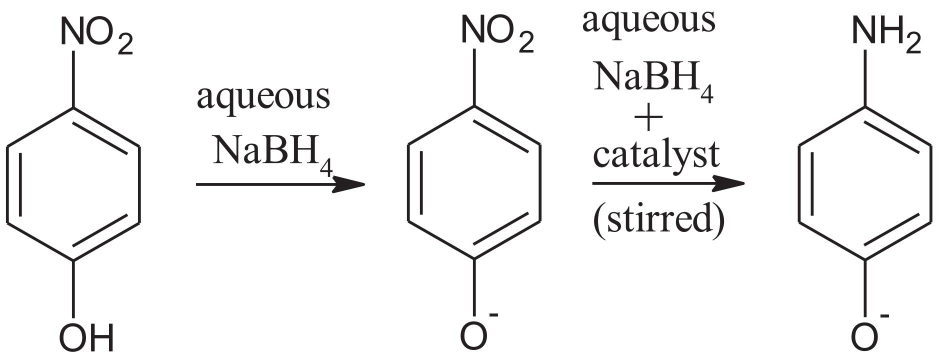

Figure 2.17 Reaction scheme of 4-nitrophenol reduction by $NaBH_4$

2.4.2 Vapour-phase chemical reaction measurement

The vapour-phase selective 1-pentyne hydrogenation was carried out on a home-made rig at Johnson Matthey Technology Centre as shown in **Figure 2.18**. The whole system consists of three parts: Tube Furnace (Carbolite) with a quartz tube reactor; gas chromatograph (Varian CP-3800) for product composition measurement; and liquid pump system (Shimadzu LC-9A) for control of the reagent flow. The catalyst powders were filled in a 360-mm quartz tube (outside diameter: 6 mm, internal diameter: 4 mm) and held by quartz wool, which is chemically inert for this reaction. The reaction tube was placed in the middle of the tube furnace with the temperature systematically controlled. The typically temperature ramping speed for the experiment is 5 ^{o}C/min as shown in **Figure 2.19**. The reactive gases were regulated by a flow meter (Mass-Stream) and mixed into a tube reactor. For this experiment, the reactive gases were obtained by mixing the vaporizing 1-pentyne solution (concentration: 1 M; flow rate: 0.04 ml/min) with reducing gas feed (40% H_2/60% He at an air calibrated flow rate of 200 ml/min) through a preheated filter at the top of the reactor. After the mixture passed through the catalyst powders, it was then transported to the gas chromatograph for the composition analysis.

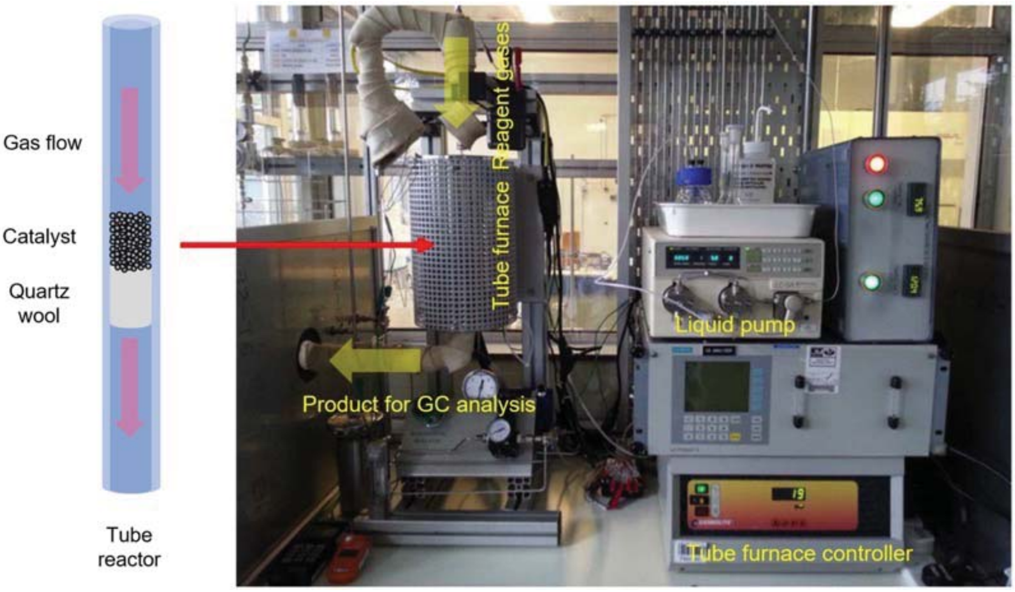

Figure 2.18 Photograph of the gas-phase reaction system at the Johnson Matthey technology centre,[4] which consists of three parts: Tube Furnace (Carbolite) with a quartz tube reactor; gas chromatograph (Varian CP-3800) for product composition measurement; and liquid pump system (Shimadzu LC-9A) for control of the reagent flow.

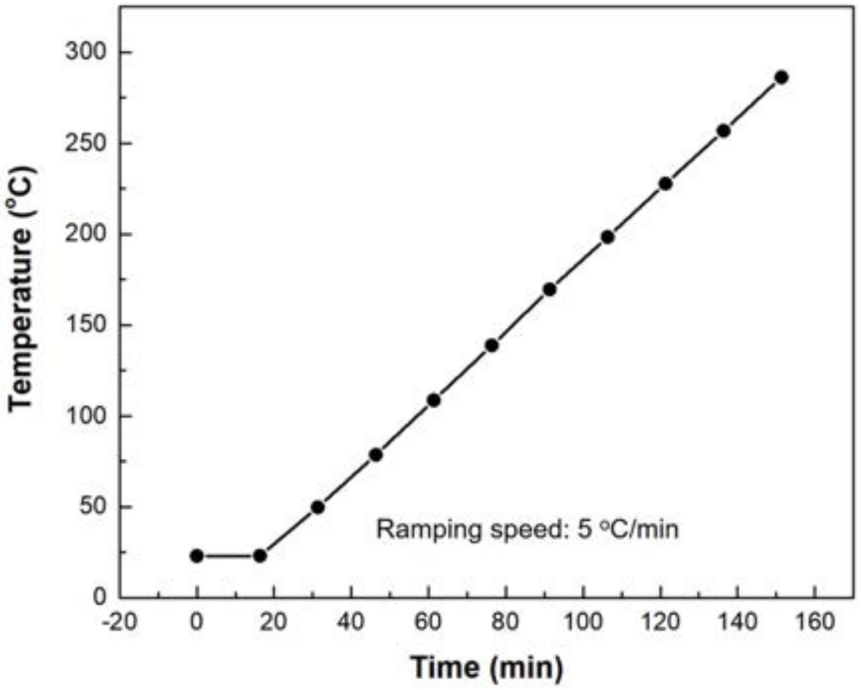

Figure 2.19 Plot of the temperature ramping curve for the 1-pentyne hydrogenation.

References

(1) P. R. Ellis; C. M. Brown; P. T. Bishop; J. Yin; K. Cooke; W. D. Terry; J. Liu; F. Yin; Palmer, R. E. The cluster beam route to model catalysts and beyond. *Faraday Discuss.* **2016,** *188*, 39.

(2) Waits, R. K. Planar magnetron sputtering. *J. Vac. Sci. Technol.* **1978,** *15* (2), 179.

(3) Pratontep, S.; Carroll, S. J.; Xirouchaki, C.; Streun, M.; Palmer, R. E. Size-selected cluster beam source based on radio frequency magnetron plasma sputtering and gas condensation. *Rev. Sci. Instrum.* **2005,** *76* (4), 045103.

(4) Hu, K.-J. Structural variation of size-selected metal clusters in chemical reactions. University of Birmingham 2015.

(5) Granqvist, C. G.; Buhrman, R. A. Ultrafine metal particles. *J. Appl. Phys.* **1976,** *47* (5), 2200.

(6) Soler, J. M.; García, N.; Echt, O.; Sattler, K.; Recknagel, E. Microcluster growth: transition from successive monomer addition to coagulation. *Phys. Rev. Lett.* **1982,** *49* (25), 1857.

(7) Hihara, T.; Sumiyama, K. Formation and size control of a Ni cluster by plasma gas condensation. *J. Appl. Phys.* **1998,** *84* (9), 5270.

(8) Haberland, H.; Karrais, M.; Mall, M.; Thurner, Y. Thin films from energetic cluster impact: A feasibility study. *J. Vac. Sci. Technol. A* **1992,** *10* (5), 3266.

(9) von Issendorff, B.; Palmer, R. E. A new high transmission infinite range mass selector for cluster and nanoparticle beams. *Rev. Sci. Instrum.* **1999,** *70* (12), 4497.

(10) Leung, C.; Palmer, R. E., *Nanoclusters: A bridge across disciplines*. Elsevier: New York, 2010; Vol. 1, p 517.

(11) Palmer, R. E.; Cao, L.; Yin, F. Note: Proof of principle of a new type of cluster beam source

with potential for scale-up. *Rev. Sci. Instrum.* **2016,** *87* (4), 046103.

(12) Cao, L. Deposition of size selected nanoclusters. University of Birmingham 2015.

(13) Shyjumon, I.; Gopinadhan, M.; Helm, C. A.; Smirnov, B. M.; Hippler, R. Deposition of titanium/titanium oxide clusters produced by magnetron sputtering. *Thin Solid Films* **2006,** *500* (1-2), 41.

(14) Larsen, R. A.; Neoh, S. K.; Herschbach, D. R. Seeded supersonic alkali atom beams. *Rev. Sci. Instrum.* **1974,** *45* (12), 1511.

(15) Geohegan, D. B.; Puretzky, A. A.; Duscher, G.; Pennycook, S. J. Time-resolved imaging of gas phase nanoparticle synthesis by laser ablation. *Appl. Phys. Lett.* **1998,** *72* (23), 2987.

(16) Zhao, J.; Cao, L.; Palmer, R. E.; Nordlund, K.; Djurabekova, F. Formation and emission mechanisms of Ag nanoclusters in the Ar matrix assembly cluster source. *Phys. Rev. Materials* **2017,** *1*, 066002.

(17) Habibpour, V.; Song, M. Y.; Wang, Z. W.; Cookson, J.; Brown, C. M.; Bishop, P. T.; Palmer, R. E. Novel powder-supported size-selected clusters for heterogeneous catalysis under realistic reaction conditions. *J. Phys. Chem. C* **2012,** *116* (50), 26295.

(18) Yang, D. S.; Mohammed, O. F.; Zewail, A. H. Scanning ultrafast electron microscopy. *Proc Natl Acad Sci U S A* **2010,** *107* (34), 14993.

(19) Lord Rayleigh, F. R. S. XXXI. Investigations in optics, with special reference to the spectroscope. *The London, Edinburgh, and Dublin Philosophical Magazine and Journal of Science* **2009,** *8* (49), 261.

(20) Bohm, D. A Suggested Interpretation of the Quantum Theory in Terms of "Hidden" Variables. I. *Phys. Rev.* **1952,** *85* (2), 166.

(21) Williams, D. B.; Carter, C. B., *Transmission electron microscopy: A textbook for materials science*. Springer US: 2009.

(22) https://en.wikipedia.org/wiki/Astigmatism_(optical_systems).

(23) Hawkes, P. W. Aberration correction past and present. *Philos Trans A Math Phys Eng Sci* **2009,** *367* (1903), 3637.

(24) Haider, M.; Rose, H.; Uhlemann, S.; Schwan, E.; Kabius, B.; Urban, K. A spherical-aberration-corrected 200 kV transmission electron microscope. *Ultramicroscopy* **1998,** *75*, 53.

(25) Subramanian, S.; Rai, R. S., *Tranmission electron microscopy for failure analysis of semiconductor devices*. ASM International: United States of America, 2004.

(26) Rutherford, E. LXXIX. The scattering of α and β particles by matter and the structure of the atom. *The London, Edinburgh, and Dublin Philosophical Magazine and Journal of Science* **2009,** *21* (125), 669.

(27) Crewe, A. V.; Wall, J.; Langmore, J. Visibility of single atoms. *Science* **1970,** *168*, 1338.

(28) Wang, Z. W.; Li, Z. Y.; Park, S. J.; Abdela, A.; Tang, D.; Palmer, R. E. Quantitative Z-contrast imaging in the scanning transmission electron microscope with size-selected clusters. *Phys. Rev. B* **2011,** *84* (7), 073408.

(29) Shindo, D.; Oikawa, T., *Analytical electron microscopy for materials science*. Springer Japan: 2002.

(30) Watanabe, M.; Williams, D. B. The quantitative analysis of thin specimens: a review of progress from the Cliff-Lorimer to the new ζ-factor methods. *J. Microsc.* **2006,** *221*, 89.

(31) Schindelin, J.; Arganda-Carreras, I.; Frise, E.; Kaynig, V.; Longair, M.; Pietzsch, T.; Preibisch, S.; Rueden, C.; Saalfeld, S.; Schmid, B.; Tinevez, J. Y.; White, D. J.; Hartenstein, V.;

Eliceiri, K.; Tomancak, P.; Cardona, A. Fiji: an open-source platform for biological-image analysis. *Nat. Methods* **2012,** *9* (7), 676.

(32) Bracey, C. L.; Ellis, P. R.; Hutchings, G. J. Application of copper-gold alloys in catalysis: current status and future perspectives. *Chem. Soc. Rev.* **2009,** *38* (8), 2231.

(33) Zhao, P.; Feng, X.; Huang, D.; Yang, G.; Astruc, D. Basic concepts and recent advances in nitrophenol reduction by gold- and other transition metal nanoparticles. *Coord. Chem. Rev.* **2015,** *287*, 114.

(34) Ciganda, R.; Li, N.; Deraedt, C.; Gatard, S.; Zhao, P.; Salmon, L.; Hernandez, R.; Ruiz, J.; Astruc, D. Gold nanoparticles as electron reservoir redox catalysts for 4-nitrophenol reduction: a strong stereoelectronic ligand influence. *Chem. Commun.* **2014,** *50* (70), 10126.

(35) Saha, S.; Pal, A.; Kundu, S.; Basu, S.; Pal, T. Photochemical green synthesis of calcium-alginate-stabilized Ag and Au nanoparticles and their catalytic application to 4-nitrophenol reduction. *Langmuir* **2010,** *26* (4), 2885.

(36) Layek, K.; Kantam, M. L.; Shirai, M.; Nishio-Hamane, D.; Sasaki, T.; Maheswaran, H. Gold nanoparticles stabilized on nanocrystalline magnesium oxide as an active catalyst for reduction of nitroarenes in aqueous medium at room temperature. *Green Chem.* **2012,** *14* (11), 3164.

CHAPTER 3

Catalytic Properties of Physically Deposited Preformed Au/Cu Nanoalloy Clusters for the Reduction of 4-Nitrophenol

In this chapter, we present the catalytic behaviour of physically deposited cluster catalysts (Au/Cu binary clusters on MgO powder supports) in the catalytic reduction of 4-nitrophenol to 4-aminolphenol in solution at room temperature. The idea was proposed in a discussion with Prof. Richard Palmer. I made the Au/Cu cluster catalysts and did the STEM characterizations and catalysis measurements. Jinlong Yin and Kevin Cooke provided the training on the cluster source in Teer Coating's Ltd. Peter R. Ellis, Christopher M. Brown and Ross Griffin provided help with the catalysis measurements. Guojing Chang, Dongjiang Yang, Jun Ren did the DFT simulations on the model clusters. This work has been published in the paper (with me as the first author): *Performance of Preformed Au/Cu Nanoclusters Deposited on MgO Powders in the Catalytic Reduction of 4-Nitrophenol in Solution, Small, 14, 1703734, 2018; doi.org/10.1002/smll.201703734.* Most of the text and figures in this chapter are taken or adapted from this paper.

3.1 Introduction

As we discussed in the chapter 1, cluster beam deposition is a new method to prepare heterogeneous catalysts for research and development, in which atomic clusters (nanoparticles) of tunable size typically below 10 nm are pre-assembled into a beam and then deposited in a vacuum chamber onto the catalyst support.[1-4] Potential advantages of this approach include the absence of solvent and effluent in the catalyst synthesis; control of cluster size, composition and morphology; and the absence of ligands compared with colloidal routes.[5-8] However, this technique is at an early stage,[9] most especially where catalytic behaviour under realistic reaction conditions is concerned. Thus there is an urgent need to validate the performance of this new class of nanomaterials in a series of model chemical transformations, and compare their behaviour with catalysts prepared by more traditional and well established routes. In this work, we report a first investigation of a liquid phase transformation performed by nanoalloy catalysts prepared by cluster beam deposition.

The discovery of the catalytic activity of Au nanoparticles for low temperature oxidation of CO provoked an explosion of interest in gold catalysis. [10-11] Au clusters can catalyse a range of reactions, e.g. the water-gas shift reaction[12-14] and selective oxidation of carbon-carbon double bonds[15-16] and carbon-oxygen bonds.[17-18] The 4-nitrophenol reduction by $NaBH_4$ is considered to be a standard model catalytic reaction[19-20] to evaluate nano-catalyst activity; precise optical measurement of the amount of 4-nitrophenol at very low concentrations is feasible. It is commonly believed that this reaction follows a Langmuir-Hinshelwood (LH) mechanism (**Figure 3.1**), [21-22] in which 4-nitrophenol is adsorbed on the surface of Au particles and reacts with activated hydrogen on the surface formed by the decomposition of $NaBH_4$. It was proposed that adding to Au a second metal element, M, which has a larger adsorption energy for nitrophenol compared to Au, can enhance the reaction rate.[23] The O-N bonds from the nitro group become weaker due to the electron delocalization from the O to the metal atoms, which directly correlates to the reaction rate. Based on this understanding, much effort has been made to produce Au/M bimetallic clusters on different supports and investigate their catalytic performance. For example, Pretzer et al.[24] synthesized Au nanoparticles decorated with palladium (Pd) and found that the activity of the Pd/Au catalyst is 5.5 (13) times that of pure Au (Pd) nanoparticles. Similar evidence of synergistic effects in nitrophenol and nitrothiophenol reduction over Au/Ni catalysts was reported.[25]

The use of copper (Cu) as an additive to improve the activity of noble metal clusters has become a "hot topic" because it can reduce the cost of catalysts and improve catalytic properties simultaneously.[26] It has been reported that adding Cu to Au nanoparticles can significantly improve their catalytic activity in many reactions, e.g. CO oxidation.[27-30] However, for nitrophenol reduction catalysed by Au/Cu bimetallic clusters, limited reports can be found and the catalytic mechanism is unconfirmed. It is commonly believed that Cu has a stronger interaction with the nitro group of nitrophenol than Au, which increases the adsorption energy of nitrophenol on the catalyst surface. Deposition of Au on the surface of Cu nanoparticles by a chemical method led to catalytic activity for 4-nitrophenol reduction that was enhanced by one order of magnitude in comparison with a pure Au catalyst.[31] However, there was no clear evidence that the enhanced activity results from a synergetic effect between Au and Cu, since no Au/Cu alloy structure was observed. Au/Cu bimetallic clusters produced on planar sapphire substrates were active for 4-nitrophenol reduction and the activity could be enhanced by visible light (due to the localized surface plasmon resonance).[32] But the activity without excitation of the light was not explored. Thus, it is important to clarify the active sites in the Au/Cu system due to their significance in catalyst design. Traditionally, Au/Cu bimetallic clusters have been efficiently prepared by various chemical methods, for example, co-impregnation,[33] deposition-precipitation[34] and colloidal methods[35] etc. However, a common disadvantage of these chemical methods is the presence of residual impurities, coming from the anion group of the metal salts not fully burned off in the calcination process or from capping ligands, as used purposely to reduce cluster aggregation. Some researchers report that capping ligands can either decrease the cluster activity by hindering reagent access to the catalyst[36-37] or can increase the activity via electron donation.[38] The existence of these impurities complicates the explanation of the original catalytic activity of the cluster, and can sometimes lead to misinterpretations. Moreover, another major challenge for chemical synthesis of binary nanoparticles is making sure that all the Au and Cu atoms are alloyed inside the clusters. A well-controlled way to make naked Au/Cu nanoparticle catalysts is desirable.

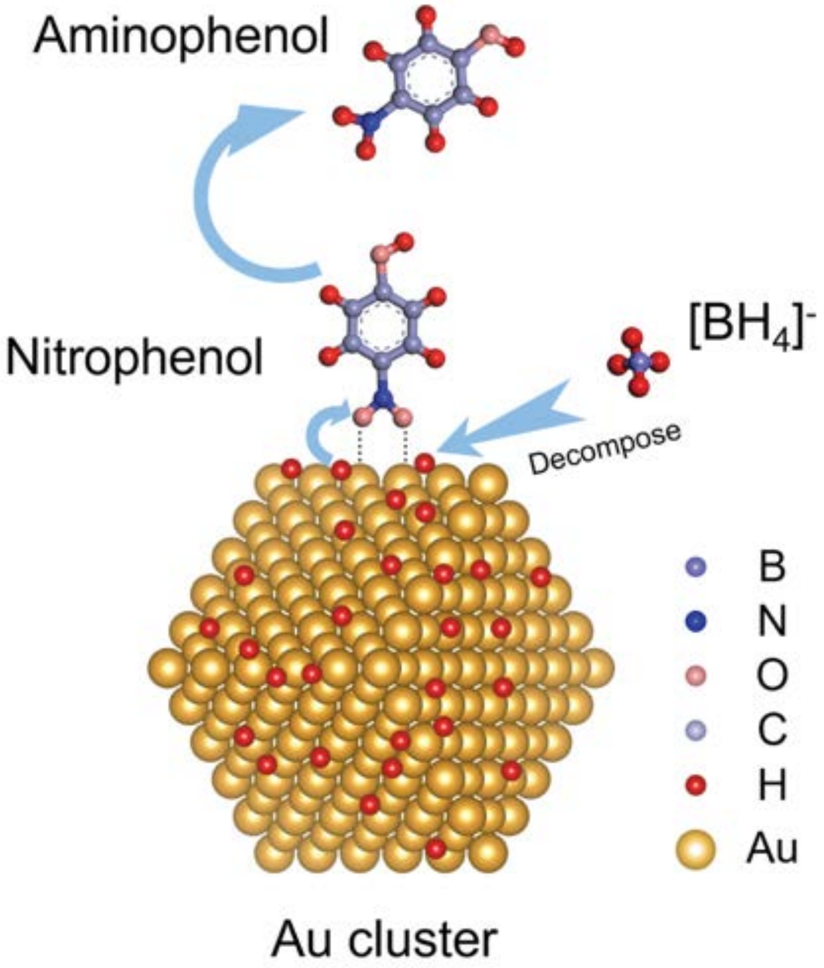

Figure 3.1 Schematic diagram of catalytic reduction of 4-nitrophenol on an Au cluster by $NaBH_4$, following a Langmuir-Hinshelwood mechanism. 4-nitrophenol molecules bind with Au clusters and react with activated hydrogen on the cluster surface formed by decomposition of $NaBH_4$.

Cluster beam deposition is one way to make well controlled nanoparticles because the clusters are formed by gas condensation in high vacuum, and then deposited onto supports directly. In this chapter, we employed a dual-magnetron sputtering gas condensation cluster source to produce Au/Cu bimetallic clusters deposited on an inert powder support, MgO. By changing the power applied to the two targets (Au, Cu), the average Au/Cu ratio can be tuned. Aberration-corrected STEM in HAADF mode, coupled with EDS, reveals that the Au/Cu bimetallic clusters have a random alloy structure. We find that these bimetallic clusters are much more active in selective nitrophenol hydrogenation than pure Au or Cu clusters, and 25 times more active than reference Au/Cu binary nanoparticles produced by impregnation. The interplay between surface Au and Cu sites is deduced to create the most active site for reaction. Our study thus validates the performance of the new nanoalloy materials in a solution phase reaction, and provides an insight into nanocatalyst design of bimetallic systems at the atomic scale.

3.2 Experimental section

Au/Cu clusters with three different Au/Cu ratios were deposited on agitated MgO powder supports. A schematic diagram of the system is shown in **Figure 2.1**. Detailed information can be found in section 2.1.1 and an earlier report.[5] In the magnetron sputtering chamber, two magnetron (with copper and gold target, respectively) are mounted in parallel with a condensation length (the distance between these targets and the exit nozzle of the condensation chamber) of 24 cm. The sputtering power applied to each magnetron is separately controlled in order to tune the material ratio in the resulting binary clusters. Au and Cu atoms are sputtered from the targets and condensed in cold Ar/He gas to form Au/Cu clusters of various sizes. A pressure of ~ 0.21 mbar was maintained in the condensation chamber, with 100 standard cubic centimeters per minute (sccm) Ar flow and 20 sccm He flow. Positively charged clusters are extracted, accelerated and guided by a series of ion optical lenses. The ultimate flight direction of the cluster beam is controlled by an “octosphere” deflector that can transmit the cluster beam forward into a lateral time-of-flight mass filter[39] to measure the clusters’ mass distribution or bend the beam by 90° to propagate vertically towards a lower chamber for powder deposition. In this deposition chamber, the powder supports (0.8 g MgO powders) were loaded into a cup which is agitated continuously to maximize exposure of all the powder to the cluster beam. In addition, during the deposition process, the cup was biased with a potential of -1 kV to accelerate and thus help immobilize clusters on the powder surface. The support used in this experiment was MgO powder obtained from Alfa Aesar with particle size between 100 and 200 nm. The powder itself has been tested and confirmed to be catalytically inert for the nitrophenol reduction reaction. The reference sample of Au_1Cu_1 on MgO powder (Alfa Aesar, size between 100-200 nm) was prepared by a traditional impregnation method[33] which has been introduced in section 2.31.

The elemental composition of the cluster catalysts was characterized by EDS in the STEM and by inductively-coupled plasma mass spectrometry (ICP-MS) following digestion in aqua regia. The cluster size and atomic structure were characterized by a JEOL JEM-2100F scanning transmission electron microscope equipped with a C_s probe corrector (CEOS) at a convergence angle of 20 mrad and a HAADF detector operating with inner angle of 62 mrad and outer angle of 164 mrad at 200 kV. STEM samples were prepared by dispersing the MgO powders decorated with clusters in deionized water, sonicating for several minutes and drop-casting onto a nickel grid coated with an amorphous carbon film.

The geometry optimization of the models (4-nitrophenol and 4-aminophenol absorbed on Au_{13}, Cu_{13} and $Au_{12}Cu_1$ clusters) were performed by professor Dongjiang Yang's group, based on the spin-polarized density functional theory (DFT), as implement in the Vienna Ab initio Simulation Package (VASP),[40-41] where plane waves were employed as basis with a cutoff energy of 400 eV. To describe the core electrons interactions, projector augmented waves[42] (PAW) were employed, and generalized gradient approximation (GGA) was used as the exchange-correlation energy correction. The geometry optimization of the metal cluster/molecule was carried out at the gamma-point of the Brillouin zone. All the optimized structures were set to 10^{-5} eV/atom in energy threshold and 0.02 eV/Å in force convergence. The adsorption energy of nitrophenol (aminophenol) on the metal cluster can be obtained by the equation below. All the energies refer to the optimized systems.

$$E_{ads}=E_{cluster}+E_{molecule}-E_{cluster/molecule} \tag{1}$$

Where the $E_{cluster}$, $E_{molecule}$ and $E_{cluster/molecule}$ are the energies of the free metal cluster, the molecule to be adsorbed and the entire composite system (cluster/molecule), respectively. The length of the N-O and O-metal bonds were measured directly from the optimized structures.

It should be mentioned that the selected model configuration was a buckled biplanar model[43] (one layer has 6 atoms and the other layer has 7 atoms), which has been confirmed to be more stable than an icosahedron.[44] Using *ab initio* calculations, the stability of the biplanar configuration to the other three configurations which are commonly reported in the literature, were also compared in **Table 3.1**. It is clear that the biplanar configuration is the most stable one since it has the lowest energy.

Table 3.1 Energies of the Au_{13} clusters with different configurations

Configurations	**Energy (eV)**	**Configurations**	**Energy (eV)**
Au biplanar	**-28.10**	Cu biplanar	**-30.69**
Au ino-decahedron	-26.59	Cu ino-decahedron	-28.49
Au icosahedron	-26.26	Cu icosahedron	-30.33
Au cuboctahedron	-27.23	Cu cuboctahedron	-29.78

3.3 Results and discussions

3.3.1 Analysis of physically deposited Au/Cu bimetallic clusters

Au/Cu clusters with three different Au/Cu ratios - that we term Au-rich, Au/Cu-equal (approximately) and Cu-rich - were produced by applying sputtering powers to the Au and Cu targets of 6 W : 3 W, 6 W : 6 W and 3 W : 6 W, respectively. The cluster size was characterized by two methods, time-of-flight mass filtering which gives cluster size (mass) information before depositing onto the supports, and STEM which provides cluster size (diameter) information after landing on the supports. **Figure 3.2** shows mass spectra obtained during the cluster deposition as well as STEM cluster diameter distribution histograms for the following samples: Au-rich (a), (d); Au/Cu-equal (b), (e); and Cu-rich (c), (f). The insets show typical low magnification HAADF images of the kind used to acquire the cluster diameter histograms. From the mass spectra, the Au-rich and Cu-rich clusters have peaks at similar masses of ~ 40,000 amu, which is equivalent to the mass of Au_{200}, whereas the Au/Cu-equal clusters peak at a larger value of ~ 65,000 amu, equivalent to the mass of Au_{300}. The cluster diameter histograms based on the HAADF images also show the same trend, i.e. that Au-rich clusters and Cu-rich clusters have a smaller cluster diameter ~ 3.6 nm, than Au/Cu-equal clusters, ~ 4.6 nm. To clarify whether agglomeration takes place after clusters landed on the support, the diameter of the Au/Cu-equal clusters at the peak position in the mass spectrum is estimated based on the cluster volume assuming a quasi-spherical shape. If the cluster composition is assumed to be Au_1Cu_1 and the cluster has a spherical shape on the support, the diameter of a cluster with a mass of 65,000 amu should be ~ 2.4 nm (~3.0 nm for hemispherical clusters), which is much smaller than the average diameter, 4.6 nm, obtained from HAADF images. This indicates that the Au/Cu-equal clusters are larger because they aggregate on the support surface, or possibly lose their spherical shape after landing on the support. In the HAADF images some large clusters formed by coalescence can easily be observed. It should be noted that the surface agglomeration which happens during the deposition process occurs because the powder supports in the vibration cup cannot be agitated entirely and evenly, especially when they are charged by the cluster ion beam, leading to uneven cluster coverage. This behavior occurs for all three samples. Such surface agglomeration has also been reported for deposition of Fe-Co nanoalloy clusters onto carbon supports by dual plasma guns.[45]

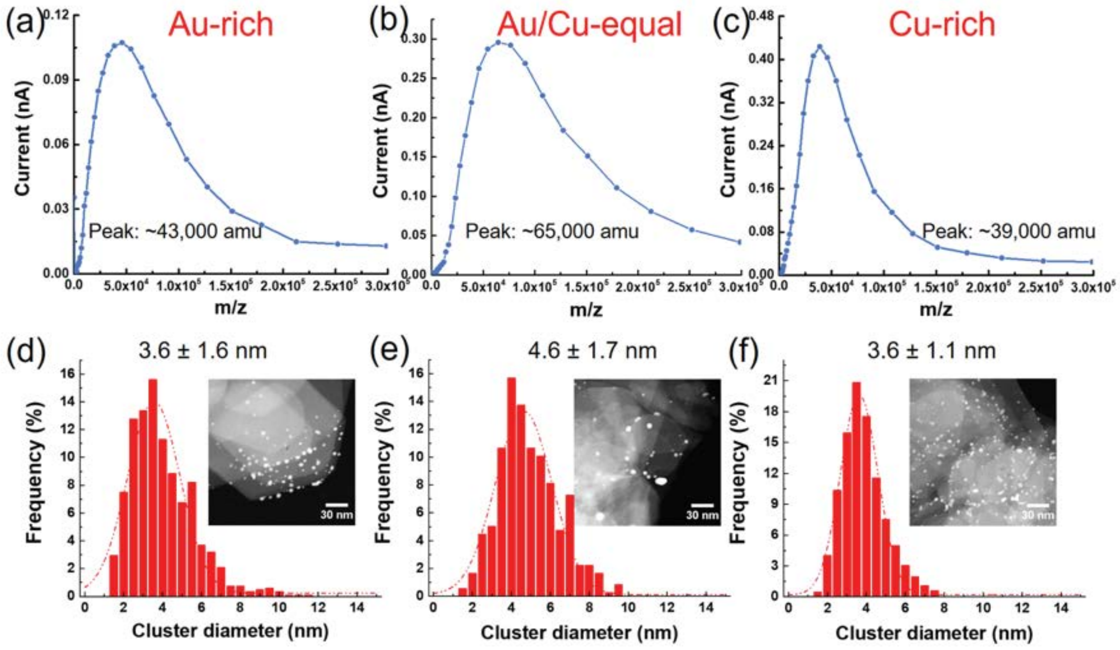

Figure 3.2 (a)-(c) Mass spectra obtained during the cluster deposition process, and (d)-(f) diameter distributions of Au/Cu bimetallic clusters on MgO powder with different Au/Cu ratios; (a) and (d) Au-rich, (b) and (e) Au/Cu-equal, (c) and (f) Cu-rich. The insets are the corresponding low-magnification HAADF images.

Table 3.2 ICP results of the Au/Cu nanoalloy clusters produced as a function of the power applied to the Au and Cu targets

Sample	Au/Cu target Power	Au loading wt%	Cu loading wt%	Au/Cu atomic ratio
Au-rich	6W : 3W	0.12	0.01	3.87 : 1
Au/Cu-equal	6W : 6W	0.18	0.05	1.16 : 1
Cu-rich	3W : 6W	0.07	0.05	0.45 : 1

Table 3.2 shows the ICP results as a function of sputtering power applied to each target, yielding the Au-rich, Au/Cu-equal (approximately) and Cu-rich nanoalloy samples. It can be seen from the Table that the total metal loadings of these three

samples are different, but the atomic ratios of Au and Cu in Au-rich, Au/Cu-equal and Cu-rich samples are 3.87:1, 1.16:1 and 0.45:1, respectively, which indicates the overall catalyst composition is strongly dependent on the power applied to each target. To identify the distributions of Au and Cu atoms inside the clusters, compositional line profiles across individual clusters in each kind of sample were obtained by EDS line scanning (in **Figure 3.3**). Within the clusters, both Au and Cu signals are detected in each of these three samples and no obvious valleys or peaks are observed, which suggests Au atoms and Cu atoms are mixed together instead of forming core-shell or Janus structures. Theoretically, mixing of Au and Cu is energetically-favoured in Au/Cu compounds compared with separated phases.[46-49] A steady increase of Cu signal observed from the Au-rich sample to the Cu-rich sample confirms the increasing Cu content inside the clusters. In addition to EDS line scans, the EDS maps on more than 50 clusters for each sample also confirm the formation of an alloy structure. The typical datasets are shown in **Figure 3.4**. For all the samples, both Au and Cu signals are detected from all clusters which further indicates that the clusters we made are alloys.

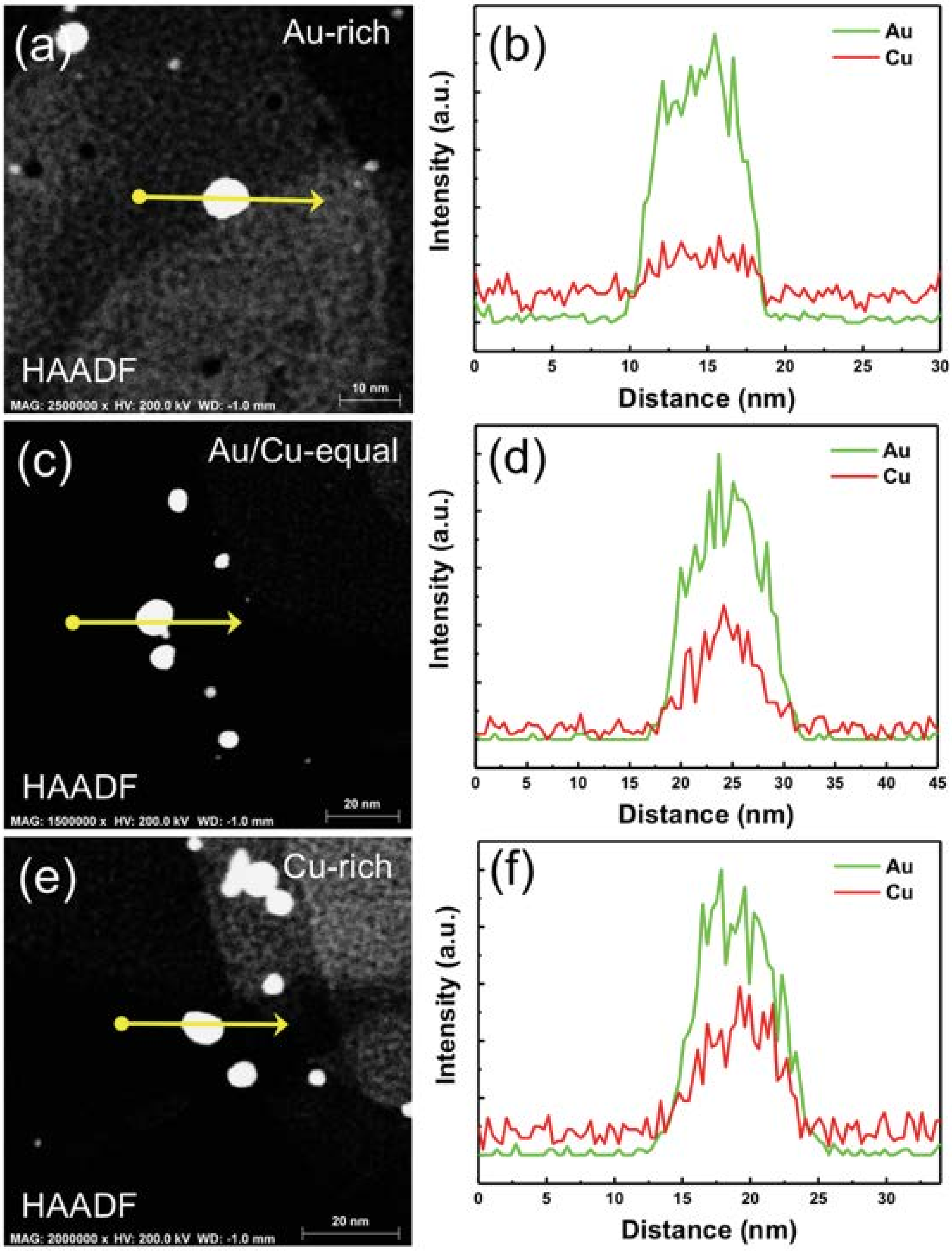

Figure 3.3 Typical HAADF images and corresponding EDS line scanning results for Au-rich clusters (a) and (b), Au/Cu-equal clusters (c) and (d), and Cu-rich clusters (e) and (f). Both Au and Cu signals are detected in each of these three samples and no obvious valleys or peaks are observed, which suggests Au atoms and Cu atoms are mixed together instead of forming core-shell or Janus structures.

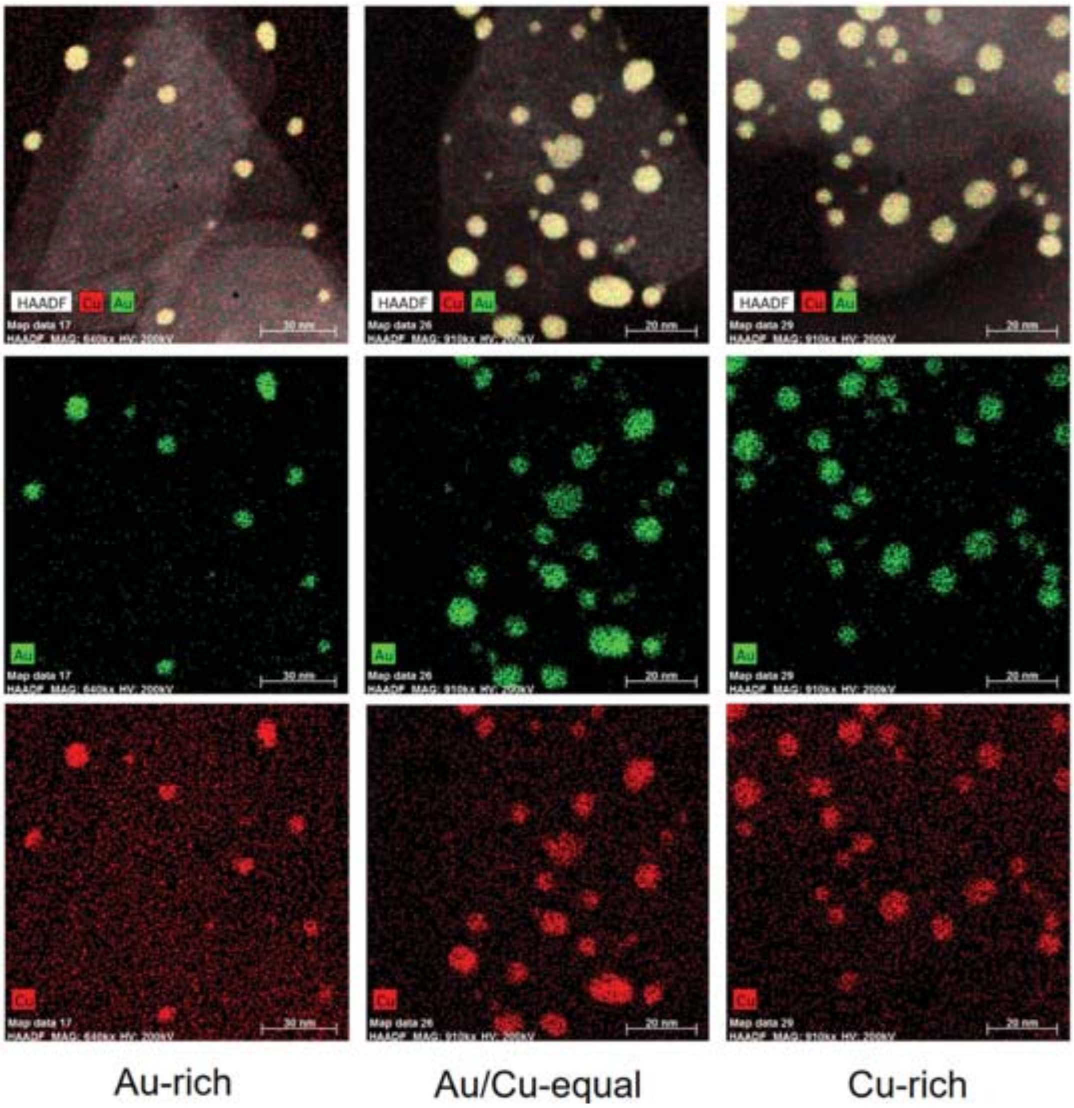

Figure 3.4 Typical EDS maps of Au (green) and Cu (red) elements from Au/Cu cluster catalysts, which further confirms the produced clusters are Au/Cu alloys.

To investigate the atomic structure of the Au/Cu bimetallic clusters, high-resolution HAADF images were acquired as shown in **Figure 3.5**. **Figure 3.5**(a) shows a typical HAADF image of an Au-rich cluster with a crystal domain aligned along the [111] zone-axis. The crystal planes marked by red lines correspond to $(2\bar{2}0)$ planes with an interplanar spacing of 1.39 Å, which lies between the interplanar spacing of $(2\bar{2}0)$ planes for pure Au (1.44 Å) and pure Cu (1.28 Å). The same trend is also found in an

Au/Cu-equal cluster (**Figure 3.5** (b)) and a Cu-rich cluster (**Figure 3.5** (c)); again the measured interplanar spacings of the (002) planes are between those of pure Au and pure Cu. This result further supports the Au/Cu alloy structure, according to Vegard's law.[50] In addition, Yin et al. distinguished the Au/Cu core/shell structure through observing the intensity contrast of HAADF STEM images.[51] A trough or a peak was observed in the intensity line profile across an Au/Cu cluster with core/shell structure. For our Au/Cu bimetallic clusters, it is apparent that no clear core-shell structure exists, which is consistent with the EDS line scanning results. This alloy structure is also observed in clusters of other orientations and amorphous clusters from all the three samples by distinguishing the HAADF intensity of STEM images. The alloy structure we find has also been reported in chemically prepared Au/Cu bimetallic clusters by other groups.[52] For the bulk Au/Cu alloy, chemically ordered structures are energetically favoured and chemically ordered Au_3Cu, Au_1Cu_1 and Au_1Cu_3 phases are found at low temperature. Here, Cu atoms and Au atoms are arranged periodically. In electron diffraction patterns, chemically ordered structures can lead to the appearance of super-structure diffraction spots along certain directions.[53-54] For example, in Au_1Cu_3 nanorods, a [110] oriented chemical ordering was observed by monitoring the appearance of (110) super-structure diffraction spots in the electron diffraction pattern.[55] To confirm the absence of chemical ordered structures in our Au/Cu bimetallic clusters, fast Fourier transforms (FFT) have been calculated for the STEM image of clusters shown in **Figure 3.5** and are displayed as inset. If the ordered structures - Au_3Cu_1, Au_1Cu_1 or Au_1Cu_3 - exist in the clusters, the super-structure diffraction spots from (110) or (100) planes should appear in the FFT images. However, in the insets to **Figure 3.5**, no super-structure diffraction spots are observed at all, which indicates that Au and Cu atoms are randomly located in the clusters and there is no chemical ordering. Finally, the intensity of columns in the HAADF images is related to the Z number of atoms.[56] The heavier the atom, the higher the intensity.[57] Considering Cu is much lighter than Au, it is reasonable to assume that lower column intensity corresponds to more Cu atoms in a column. In **Figures 3.5** (a) and (b), some atom columns are significantly darker than the adjacent columns, highlighted by white arrows, which suggests that more Cu atoms are located in these darker columns than in the neighbors. Again, this behavior is consistent with a random alloy structure.

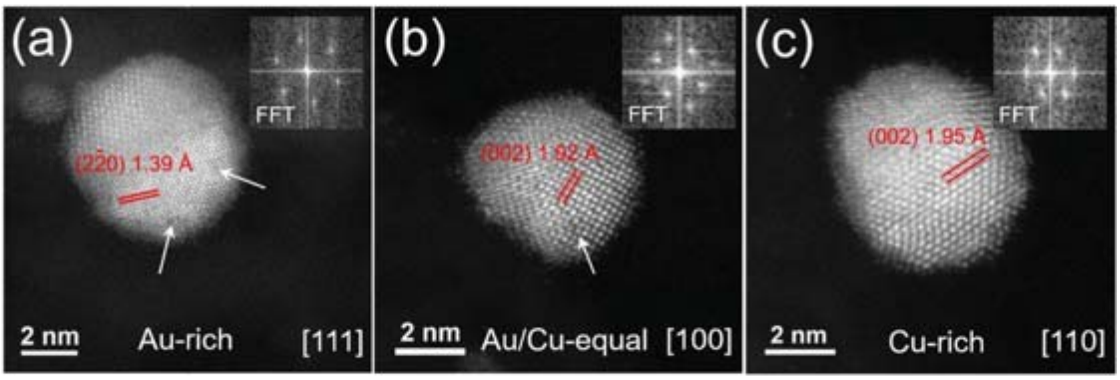

Figure 3.5 Typical high resolution HAADF images of (a) an Au-rich cluster with a crystal domain aligned along the [111] zone-axis, (b) an Au/Cu-equal cluster with a crystal domain aligned along the [100] zone-axis, and (c) a Cu-rich cluster with a crystal domain aligned along the [110] zone-axis. The insets are the FFT images corresponding to the crystal domains in each cluster.

3.3.2 Evaluation of catalytic activity for 4-nitrophenol reduction

After adding $NaBH_4$ to the nitrophenol solution, 4-nitrophenolate ions are formed, which show a strong visible absorbance at 400 nm.[58] The intensity of the absorbance peak, proportional to the concentration of 4-nitrophenolate ions, is used to evaluate the progress of the reaction. **Figure 3.6** shows typical UV-VIS absorbance spectra with time intervals of 5 min after adding of Au-rich, Au/Cu-equal and Cu-rich cluster catalysts supported on MgO. It is obvious that in the case of the Au/Cu-equal cluster catalyst, on adding the catalyst into the reaction mixture, the absorbance peak at 400 nm decreases immediately and continuously. An induction time has been observed when ligand-protected Au cluster catalysts were used,[59-60] but in this study no induction period was found as can be seen in **Figure 3.6**. However, in the case of the Au-rich and Cu-rich cluster catalysts, the peak intensity decreases much more slowly, which indicates that these catalysts are less active than the Au/Cu-equal catalysts.

The reduction of 4-nitrophenol catalyzed by metal particles is considered pseudo-first order with respect to the concentration of 4-nitrophenol in the presence of a large excess of $NaBH_4$.[61-62] Thus, the apparent reaction rate constant k_{app}, which can be used to compare the activity of the catalysts, is defined through the equation below:

$$\frac{dC_t}{dt} = -k_{app}C_t \tag{3.1}$$

Here C_t represents the concentration of nitrophenol at time t. Because the optical absorbance at time t (A_t) is proportional to C_t, a plot of C_t/C_0 and thus $-ln(C_t/C_0)$ versus t can be acquired easily from the absorbance, as shown in **Figure 3.7**. C_0 is the initial concentration of 4-nitrophenol. In accordance with the pseudo-first order kinetic assumption, the relationships for C_t/C_0 and $-ln(C_t/C_0)$ versus reaction time are fitted by an exponential decay and linear growth, respectively. The apparent reaction rate constant is obtained from the linear slope in **Figure 3.7**. The k_{app} obtained for the Au/Cu-equal cluster catalyzed reaction is 17.8×10^{-3} min^{-1}, which is almost 20 (10) times higher than that obtained for the Au-rich (Cu-rich) clusters. Considering the difference of metal loading in these three samples, the intrinsic reaction rate constant k_{nor} is calculated by normalizing the k_{app} values by the number of moles of metal as summarized in **Table 3.3**. The normalised reaction constant k_{nor} for Au/Cu-equal clusters is 3.49×10^4 $min^{-1}mol^{-1}$, which is still 8.9 (6.6) times higher than that of Au-rich (Cu-rich) clusters. It should also be noted that, compared with the Au-rich catalyst, the Cu-rich catalyst has a lower metal loading but higher normalized activity, indicating the Cu-rich clusters are more active than Au-rich clusters. We will discuss this behavior below.

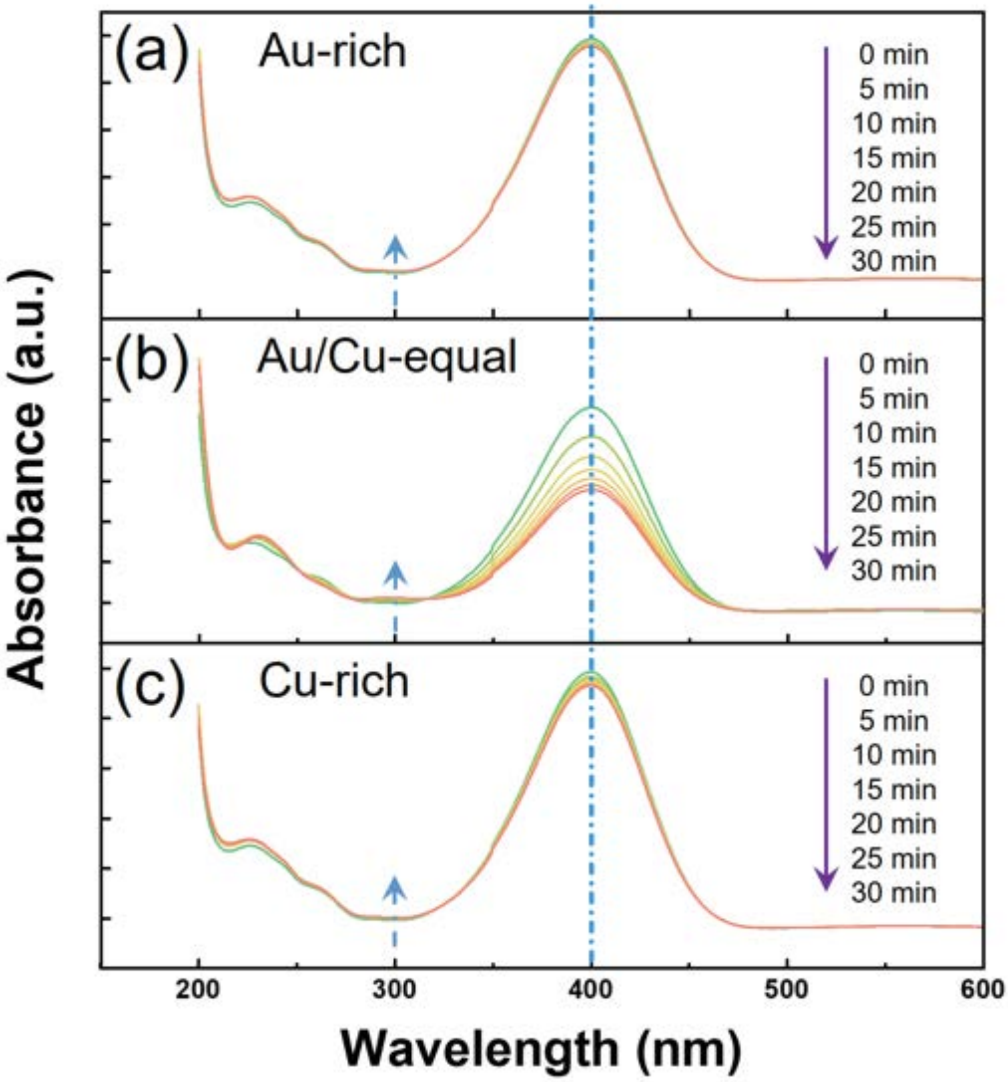

Figure 3.6 UV-VIS absorbance spectra during the 4-nitrophenol reduction by $NaBH_4$ (5 min intervals), in the presence of Au/Cu bimetallic cluster catalysts on MgO support with different Au/Cu ratios, (a) Au-rich, (b) Au/Cu-equal, (c) Cu-rich. The absorbance peak at 400 nm corresponds to 4-nitrophenol and the peak intensity relates to the concentration.

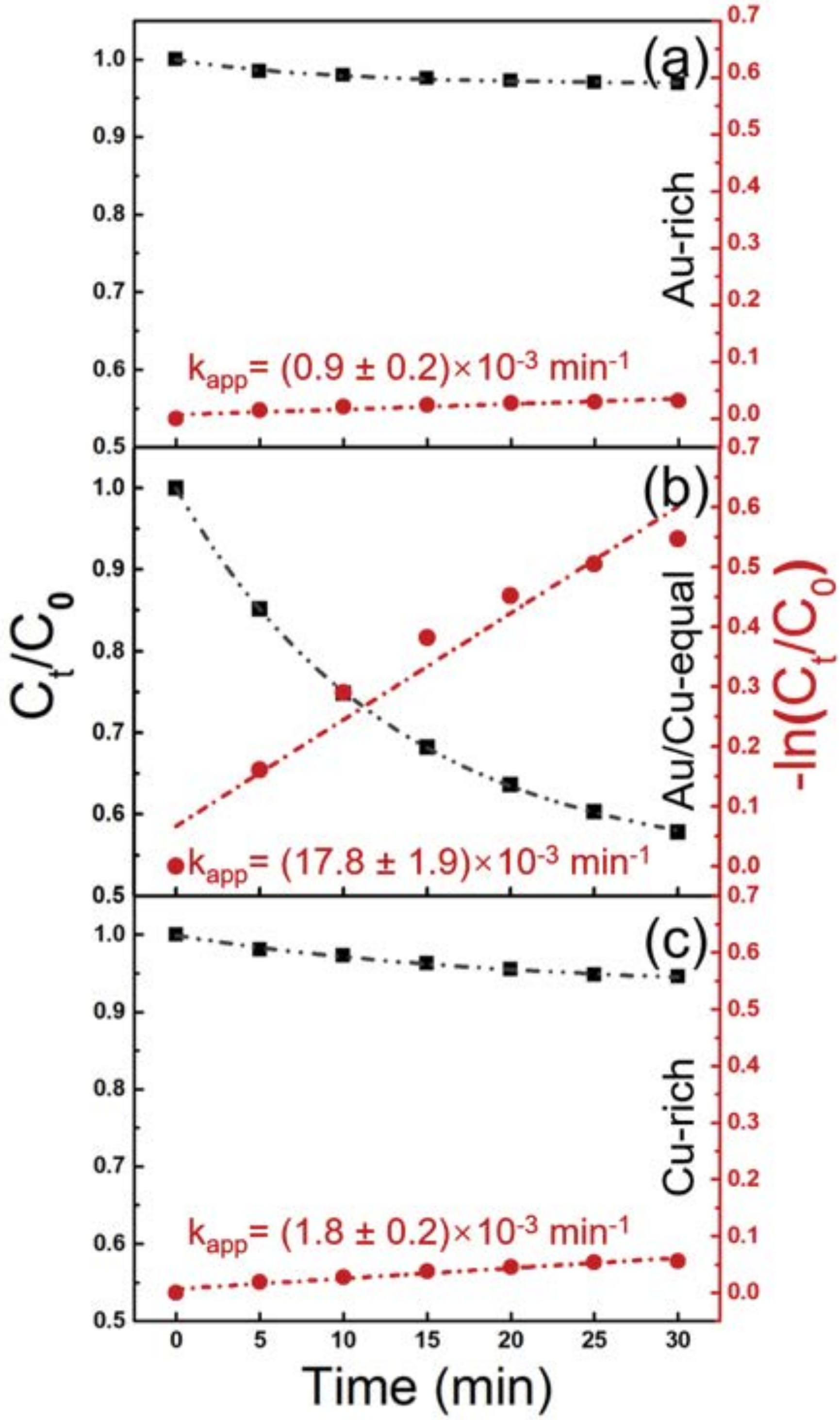

Figure 3.7 Plots of nitrophenol concentration, C_t/C_0 and $-ln(C_t/C_0)$, versus time for the nitrophenol reduction by $NaBH_4$ over (a) Au-rich, (b) Au/Cu-equal and (c) Cu-rich cluster catalysts on MgO. The slope of the red fitting lines shows the apparent reaction rate constant.

Table 3.3 Comparison of the apparent reaction rate constant k_{app} and the intrinsic reaction rate constant k_{nor} normalized by the total number of moles of metal for the reduction of nitrophenol catalysed by Au/Cu cluster catalysts.

Sample	k_{app} ($\times 10^{-3}$ min^{-1})	k_{nor} ($\times 10^{4}$ min^{-1}mole of metal^{-1})
Au-rich	0.9 ± 0.2	0.39 ± 0.09
Au/Cu-equal	17.8 ± 1.9	3.49 ± 0.37
Cu-rich	1.8 ± 0.2	0.53 ± 0.06
Au/Cu reference	1.7 ± 0.1	0.14 ± 0.01

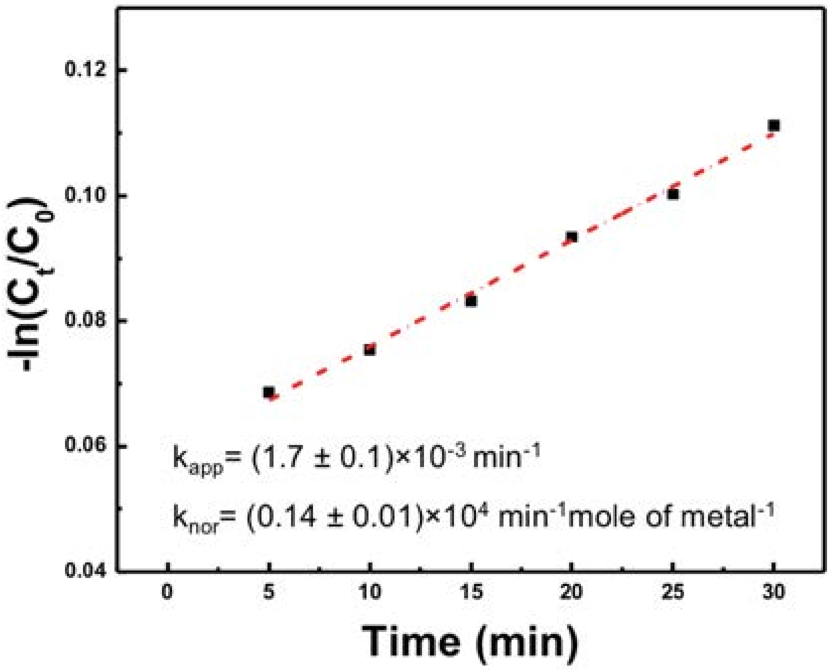

Figure 3.8 Plot of $-\ln(C_t/C_0)$ versus time for the nitrophenol reduction catalyzed by the Au/Cu reference sample. The slope of the fitted line shows the apparent reaction rate constant.

In addition, we also compared the catalytic activity of the Au/Cu-equal clusters on MgO sample with a reference catalyst (Au_1Cu_1 on MgO powder) produced by the traditional impregnation method. The k_{nor} for the reference sample is 0.14×10^4 min^{-1}

mole of metal^{-1}, which is 25 times smaller than that for the Au/Cu-equal cluster sample (see **Table 3.3** and **Figure 3.8**). A list of recent studies on 4-nitrophenol reduction over chemically produced Au and Cu based catalysts is summarized in **Table 3.4** together with our Au/Cu-equal cluster catalyst. Since many factors can affect the cluster activity such as cluster size distribution, support, ligands and the amount of $NaBH_4$ used in the reaction, it is difficult to explain why the intrinsic reaction rate constant obtained for the new cluster catalyst is not yet competitive with the best Au and Cu catalysts synthesized chemically. But this method still provides a way to establish the original catalytic activity of "naked" clusters.

Table 3.4 Recent studies on the nitrophenol reduction over Au and Cu based catalysts with different supports.

Catalyst	Particle size (nm)	$NaBH_4$/ Nitrophenol	Metal loading	k_{app} (s^{-1})	k_{nor} (s^{-1} ·mol of metal^{-1})
Au on TiO_2 **[63]**	/	100	1wt%	7.1×10^{-3}	2.4×10^{3}
Au on NAP-MgO [58]	5-7	46	1.34%	7.6×10^{-3}	7.4×10^{3}
Au on CeO_2 (powder)[64]	~ 5	41.7	0.31 wt%	3.6×10^{-5}	2.3×10^{2}
Cu [65]	5.6	167	/	1.5×10^{-3}	7.62
Cu nanocubes [66]	9.6	165	15 mM	1.0×10^{-2}	6.7×10^{3}
Cu polyhedrons [66]	18.0	165	15 mM	5.7×10^{-3}	3.8×10^{3}
Au/Cu-equal on MgO (this work)	4.6 ± 1.7	40	0.23%	3.0×10^{-4}	5.8×10^{2}

3.3.3 Discussion of the catalytic activity for 4-nitrophenol reduction over Au/Cu nanoalloy cluster catalysts and model calculations

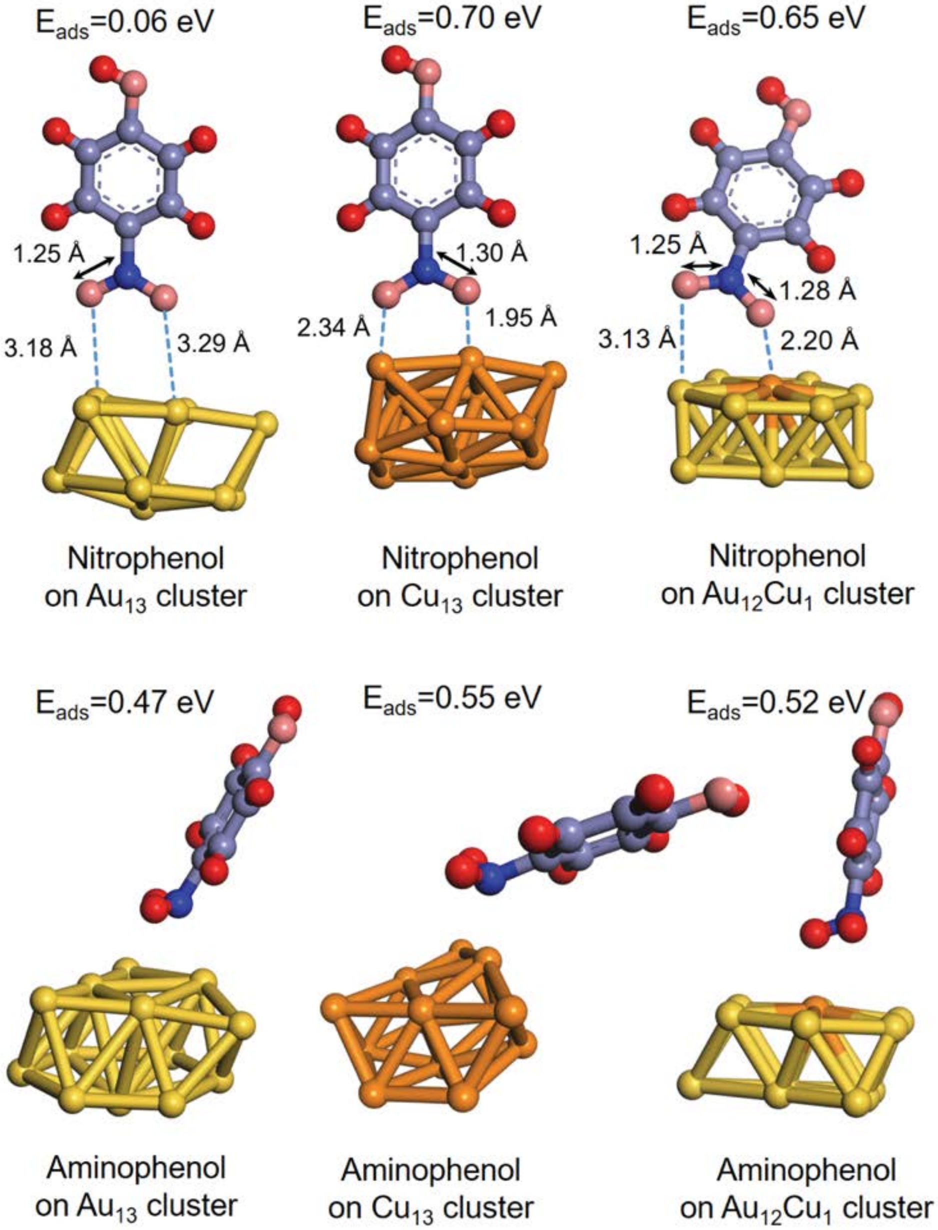

Figure 3.9 DFT-simulations of 4-nitrophenol and 4-aminophenol binding to Au_{13}, Cu_{13} and $Au_{12}Cu_1$ clusters conducted by professor Dongjiang Yang's group. The substitution of the Cu atom in the Au cluster optimized the adsorption of 4-nitrophenol and desorption of 4-aminophenol, which enhanced the catalytic activity for the whole reaction. (Atom colours as in **Figure 3.1**)

The principal topics for discussion arising from the experimental results concern: (i) why the random nanoalloy Au/Cu-equal cluster catalysts supported on MgO are so much more active than the Au-rich or Cu-rich clusters and (ii) why the Au/Cu-equal cluster catalysts are significantly more active than the reference Au/Cu catalysts generated by impregnation. In addressing these questions, the result that Cu-rich clusters are somewhat more active than Au-rich clusters should also be noticed. A central issue in understanding the enhancement of catalytic activity must be the nature of the binding of the principal reactant (4-nitrophenol) and product (4-aminophenol) to the MgO-supported Au/Cu nanoparticles.

In order to investigate the interaction between the reactant (product) and the clusters, Professor Dongjing Yang's group conducted DFT calculations about the binding of 4-nitrophenol (4-aminophenol) to model Au_{13}, Cu_{13} and $Au_{12}Cu_1$ free clusters. **Figure 3.9** summarises their results showing the DFT optimized models of 4-nitrophenol and 4-aminophenol adsorbed on Au_{13}, Cu_{13} and $Au_{12}Cu_1$ clusters. The nitrophenol bonds with two metal atoms through the two O atoms from the nitro group. As expected, the two metal-O bonds from the nitro group are much longer on the Au cluster (3.18 Å and 3.29 Å) than on the Cu cluster (2.34 Å and 1.95 Å), which reflects the fact that nitrophenol has a much stronger interaction with Cu than Au. For the $Au_{12}Cu_1$ clusters, the nitro group is bonded on an Au/Cu site and the lengths of the two metal-O bonds, Au-O bond (3.13 Å) and Cu-O bond (2.20 Å), are similar to those of the Au-O bond on the Au cluster and Cu-O bond on the Cu cluster, respectively. This indicates that the substitution of Cu in the Au cluster is helpful for 4-nitrophenol adsorption. The calculated adsorption energies of 4-nitrophenol on model clusters further confirm this conclusion. For the $Au_{12}Cu_1$ cluster the bonding energy with the nitrophenol molecule is 0.65 eV compared with 0.06 eV for the Au cluster and 0.70 eV for the Cu cluster. In addition, due to the electron delocalization from O to the metal, on the $Au_{12}Cu_1$ cluster the length of the O-N bond on Cu atom (1.28 Å) is longer than that on Au atom (1.25 Å), so the N-O bond on the Cu atom is much easier to cleave. However, the catalyst activity is also affected by the desorption of the product. The calculated adsorption energy of 4-aminophenol on $Au_{12}Cu_1$ clusters (0.52 eV) is larger than that on the Au cluster (0.47 eV), but smaller than that on Cu clusters (0.55 eV), suggesting that the aminophenol molecule also has a stronger interaction with Cu than Au. Thus, although Cu is beneficial for the adsorption of the nitrophenol and for cleavage of the N-O bonds, it also hinders the release of the product, which results in a limited catalytic activity.

The results from the model calculations, namely that Cu has a stronger interaction than Au with both the reagent, 4-nitrophenol, and the product, 4-aminophenol, provide an appealing basis for explaining why the Au/Cu-equal clusters are the most active for the reduction of the nitrophenol. Assuming the reaction follows an LH mechanism, the reduction only happens on the cluster surface. For the pure Au cluster, the catalytic activity is limited by the weak adsorption of nitrophenol, whereas the pure Cu cluster has an overly strong interaction with the aminophenol, which hinders the desorption of the product and again leads to limited activity. The combination of Au with Cu increases the adsorption energy of nitrophenol compared with gold and reduces the adsorption energy of aminophenol compared with copper. We have shown that the optimized adsorption configuration for this reaction involves the nitro group bonding with adjacent Au and Cu sites through the two O atoms; then the abundance of Au/Cu sites on the cluster surface will regulate the catalytic activity. Given the random arrangement of Au and Cu atoms in the clusters, more Au/Cu sites exist on the Au/Cu-equal cluster surface than Au-rich and Cu-rich clusters, which gives a reason why the Au/Cu-equal cluster catalyst exhibits the highest catalytic activity. Moreover, we can associate the higher catalytic activity of the Cu-rich clusters compared to the Au-rich clusters with the fact that the Au/Cu atomic ratio obtained is closer to the presumably optimal 1:1 ratio in the Cu-rich clusters (0.45:1) compared with that in the Au-rich clusters (3.87:1), which allows for more of the proposed Au-Cu active sites on the surface of the Cu-rich clusters.

Table 3.5 ICP results of the Au_1Cu_1 reference sample

Sample	Au loading wt%	Cu loading wt%	Au/Cu atomic ratio
Au_1Cu_1 reference	0.96	0.45	0.69 : 1

The reason why the Au/Cu-equal cluster catalyst is much more active than the Au/Cu reference sample seems to be associated with the diameter distribution and composition of the clusters in the reference sample, see **Figure 3.10** and **Table 3.5**. Compared with the Au/Cu-equal catalyst, the clusters in the Au/Cu reference sample have much larger diameter (~ 10 nm), which is traceable to the calcination process at high temperature.

Due to the lower specific surface area for the larger clusters, the reference sample presents significantly fewer Au/Cu active sites on the surface per unit mole of catalyst. In addition, the ICP results show that the Au/Cu atomic ratio for the reference sample is 0.69 : 1 after the calcination, which should decrease the number of the Au/Cu sites on the cluster surface. So, the unbalanced composition achieved in our impregnation method after calcination may combine with the larger size to give the reduced activity for the reference sample compared with the Au/Cu-equal clusters. The result emphasizes the utility of the cluster beam method in generating nanoparticle catalysts of tunable size below 10 nm and well-defined composition.

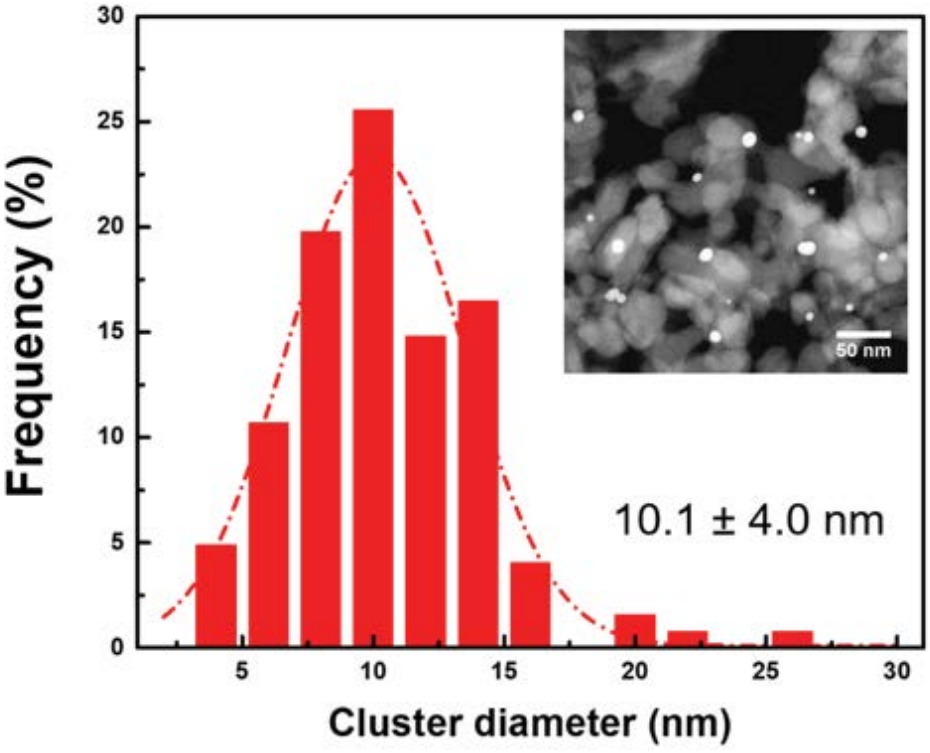

Figure 3.10 Cluster diameter distribution histogram of the Au_1Cu_1 reference sample. The inset is a typical HAADF image used to obtain the cluster diameter distribution.

3.4 Conclusions

The performance of Au/Cu bimetallic nanoparticles in a model liquid phase catalytic reaction has been validated. The nanoalloy clusters were produced by a dual-target magnetron sputtering and gas condensation cluster source and deposited onto MgO powder supports in vacuum. The composition of the Au/Cu catalysts can be controlled by tuning the power applied to the sputtering targets. EDS line scanning spectra and Z-contrast STEM images reveal that the Au/Cu bimetallic clusters, whether Au-rich, Cu-rich or Au/Cu-equal, have a random alloy structure without chemical ordering. The catalytic performance of the three types of MgO-supported catalysts in the reduction of 4-nitrophenol by $NaBH_4$ has been investigated by UV-VIS spectrophotometry. A normalised intrinsic reaction rate constant of 3.49×10^4 min^{-1} mole of $metal^{-1}$ is obtained from the Au/Cu-equal cluster catalyst, which is 8.9 (6.6) times higher than the Au-rich (Cu-rich) cluster catalysts. The enhanced catalytic activity of the Au/Cu-equal catalyst is deduced to result from a higher abundance of Au/Cu sites on the surface of the Au/Cu-equal clusters compared with the other two samples. Theoretical investigation of Au, Cu and Au/Cu clusters by professor Dongjiang Yang's group show that the proximity of Au and Cu surface atoms enables a balancing of the adsorption of 4-nitrophenol and desorption of 4-animophenol, which increases the catalytic activity for the system. Moreover, we have demonstrated that physically deposited Au/Cu-equal catalysts show an activity per mole of metal 25 times higher than that of an Au/Cu reference sample made by the chemical impregnation method. The results validate the performance of this new class of nanoalloy catalysts generated by cluster beam deposition in an important model selective transformation in the liquid phase.

References

(1) Palmer, R. E.; Pratontep, S.; Boyen, H. G. Nanostructured surfaces from size-selected clusters. *Nat. Mater.* **2003,** *2* (7), 443.

(2) Baxter, E. T.; Ha, M.-A.; Cass, A. C.; Alexandrova, A. N.; Anderson, S. L. Ethylene dehydrogenation on $Pt_{4,7,8}$ clusters on Al_2O_3: strong cluster size dependence linked to preferred catalyst morphologies. *ACS Catal.* **2017,** *7* (5), 3322.

(3) Liu, C.; Yang, B.; Tyo, E.; Seifert, S.; DeBartolo, J.; von Issendorff, B.; Zapol, P.; Vajda, S.; Curtiss, L. A. Carbon dioxide conversion to methanol over size-selected Cu_4 clusters at low pressures. *J. Am. Chem. Soc.* **2015,** *137* (27), 8676.

(4) Rondelli, M.; Zwaschka, G.; Krause, M.; Rötzer, M. D.; Hedhili, M. N.; Högerl, M. P.; D'Elia, V.; Schweinberger, F. F.; Basset, J.-M.; Heiz, U. Exploring the Potential of Different-Sized Supported Subnanometer Pt Clusters as Catalysts for Wet Chemical Applications. *ACS Catal.* **2017,** *7* (6), 4152.

(5) P. R. Ellis; C. M. Brown; P. T. Bishop; J. Yin; K. Cooke; W. D. Terry; J. Liu; F. Yin; Palmer, R. E. The cluster beam route to model catalysts and beyond. *Faraday Discuss.* **2016,** *188*, 39.

(6) Vajda, S.; White, M. G. Catalysis applications of size-selected cluster deposition. *ACS Catal.* **2015,** *5* (12), 7152.

(7) Habibpour, V.; Yin, C.; Kwon, G.; Vajda, S.; Palmer, R. E. Catalytic oxidation of cyclohexane by size-selected palladium clusters pinned on graphite. *J. Exp. Nanosci.* **2013,** *8* (7-8), 993.

(8) Ha, M. A.; Baxter, E. T.; Cass, A. C.; Anderson, S. L.; Alexandrova, A. N. Boron switch for selectivity of catalytic dehydrogenation on size-selected Pt clusters on Al_2O_3. *J. Am. Chem. Soc.*

2017, *139* (33), 11568.

(9) E. C. Tyo; Vajda, S. Catalysis by clusters with precise numbers of atoms. *Nat. Nanotechnol.* **2015,** *10* (7), 577.

(10) Haruta, M.; Kobayashi, T.; Sano, H.; Yamada, N. Novel gold catalysts for the oxidation of carbon monoxide at a temperature far below 0 DEG.C. *Chem. Lett.* **1987,** *16*, 405.

(11) Hu, K. J.; Plant, S. R.; Ellis, P. R.; Brown, C. M.; Bishop, P. T.; Palmer, R. E. Atomic resolution observation of a size-dependent change in the ripening modes of mass-selected Au nanoclusters involved in CO oxidation. *J. Am. Chem. Soc.* **2015,** *137* (48), 15161.

(12) Magadzu, T.; Yang, J. H.; Henao, J. D.; Kung, M. C.; Kung, H. H.; Scurrell, M. S. Low-temperature water–gas shift reaction over Au supported on anatase in the presence of copper: EXAFS/XANES analysis of gold–copper ion mixtures on TiO_2. *J. Phys. Chem. C* **2017,** *121* (16), 8812.

(13) Xu, H.; Li, Y.; Luo, X.; Xu, Z.; Ge, J. Monodispersed gold nanoparticles supported on a zirconium-based porous metal-organic framework and their high catalytic ability for the reverse water-gas shift reaction. *Chem. Commun.* **2017,** *53* (56), 7953.

(14) Yao, S.; Zhang, X.; Zhou, W.; Gao, R.; Xu, W.; Ye, Y.; Lin, L.; Wen, X.; Liu, P.; Chen, B.; Crumlin, E.; Guo, J.; Zuo, Z.; Li, W.; Xie, J.; Lu, L.; Kiely, C. J.; Gu, L.; Shi, C.; Rodriguez, J. A.; Ma, D. Atomic-layered Au clusters on α-MoC as catalysts for the low-temperature water-gas shift reaction. *Science* **2017,** *357* (6349), 389.

(15) Karakalos, S.; Xu, Y.; Cheenicode Kabeer, F.; Chen, W.; Rodriguez-Reyes, J. C.; Tkatchenko, A.; Kaxiras, E.; Madix, R. J.; Friend, C. M. Noncovalent bonding controls selectivity in heterogeneous catalysis: coupling reactions on gold. *J. Am. Chem. Soc.* **2016,** *138*

(46), 15243.

(16) Ravelli, D.; Protti, S.; Fagnoni, M. Carbon-carbon bond forming reactions via photogenerated intermediates. *Chem. Rev.* **2016,** *116* (17), 9850.

(17) Wang, L.; Zhang, J.; Wang, G.; Zhang, W.; Wang, C.; Bian, C.; Xiao, F. S. Selective hydrogenolysis of carbon-oxygen bonds with formic acid over a Au-Pt alloy catalyst. *Chem. Commun.* **2017,** *53* (18), 2681.

(18) Li, D.-Y.; Wei, Y.; Shi, M. Gold(I)-catalyzed intramolecular carbon-oxygen bond cleavage reaction via gold carbenes derived from vinylidenecyclopropanes. *Adv. Synth. Catal.* **2016,** *358* (19), 3002.

(19) Ye, H.; Wang, Q.; Catalano, M.; Lu, N.; Vermeylen, J.; Kim, M. J.; Liu, Y.; Sun, Y.; Xia, X. Ru nanoframes with an fcc structure and enhanced catalytic properties. *Nano Lett.* **2016,** *16* (4), 2812.

(20) Bingwa, N.; Patala, R.; Noh, J. H.; Ndolomingo, M. J.; Tetyana, S.; Bewana, S.; Meijboom, R. Synergistic effects of gold-palladium nanoalloys and reducible supports on the catalytic reduction of 4-nitrophenol. *Langmuir* **2017,** *33* (28), 7086.

(21) Zhao, P.; Feng, X.; Huang, D.; Yang, G.; Astruc, D. Basic concepts and recent advances in nitrophenol reduction by gold- and other transition metal nanoparticles. *Coord. Chem. Rev.* **2015,** *287*, 114.

(22) Ciganda, R.; Li, N.; Deraedt, C.; Gatard, S.; Zhao, P.; Salmon, L.; Hernandez, R.; Ruiz, J.; Astruc, D. Gold nanoparticles as electron reservoir redox catalysts for 4-nitrophenol reduction: a strong stereoelectronic ligand influence. *Chem. Commun.* **2014,** *50* (70), 10126.

(23) Pozun, Z. D.; Rodenbusch, S. E.; Keller, E.; Tran, K.; Tang, W.; Stevenson, K. J.;

Henkelman, G. A systematic investigation of p -nitrophenol reduction by bimetallic dendrimer encapsulated nanoparticles. *J. Phys. Chem. C* **2013,** *117*, 7598.

(24) Pretzer, L. A.; Heck, K. N.; Kim, S. S.; Fang, Y.-L.; Zhao, Z.; Guo, N.; Wu, T.; Miller, J. T.; Wong, M. S. Improving gold catalysis of nitroarene reduction with surface Pd. *Catal. Today* **2016,** *264*, 31.

(25) Vysakh, A. B.; Babu, C. L.; Vinod, C. P. Demonstration of synergistic catalysis in Au@Ni bimetallic core–shell nanostructures. *J. Phys. Chem. C* **2015,** *119* (15), 8138.

(26) Bandarenka, A. S.; Varela, A. S.; Karamad, M.; Calle-Vallejo, F.; Bech, L.; Perez-Alonso, F. J.; Rossmeisl, J.; Stephens, I. E. L.; Chorkendorff, I. Design of an active site towards optimal electrocatalysis: Overlayers, surface alloys and near-surface alloys of Cu/Pt(111). *Angew. Chem. Int. Ed.* **2012,** *51*, 11845.

(27) Bracey, C. L.; Ellis, P. R.; Hutchings, G. J. Application of copper-gold alloys in catalysis: current status and future perspectives. *Chem. Soc. Rev.* **2009,** *38* (8), 2231.

(28) Najafishirtari, S.; Brescia, R.; Guardia, P.; Marras, S.; Manna, L.; Colombo, M. Nanoscale transformations of alumina-supported AuCu ordered phase nanocrystals and their activity in CO oxidation. *ACS Catal.* **2015,** *5* (4), 2154.

(29) Li, X.; Fang, S. S. S.; Teo, J.; Foo, Y. L.; Borgna, A.; Lin, M.; Zhong, Z. Activation and deactivation of Au–Cu/SBA-15 catalyst for preferential oxidation of CO in H_2-rich gas. *ACS Catal.* **2012,** *2* (3), 360.

(30) Zhang, L.; Kim, H. Y.; Henkelman, G. CO oxidation at the Au–Cu interface of bimetallic nanoclusters supported on CeO_2(111). *J. Phys. Chem. Lett.* **2013,** *4* (17), 2943.

(31) Zhao, D.; Xiong, X.; Qu, C.-L.; Zhang, N. Remarkable enhancement in Au catalytic

utilization for liquid redox reactions by galvanic deposition of Au on Cu nanoparticles. *J. Phys. Chem. C* **2014,** *118* (33), 19007.

(32) Hajfathalian, M.; Gilroy, K. D.; Yaghoubzade, A.; Sundar, A.; Tan, T.; Hughes, R. A.; Neretina, S. Photocatalytic enhancements to the reduction of 4-nitrophenol by resonantly excited triangular Gold–Copper nanostructures. *J. Phys. Chem. C* **2015,** *119* (30), 17308.

(33) Belin, S.; Bracey, C. L.; Briois, V.; Ellis, P. R.; Hutchings, G. J.; Hyde, T. I.; Sankar, G. CuAu/SiO_2 catalysts for the selective oxidation of propene to acrolein: the impact of catalyst preparation variables on material structure and catalytic performance. *Catal. Sci. Technol.* **2013,** *3* (11), 2944.

(34) Sandoval, A.; Louis, C.; Zanella, R. Improved activity and stability in CO oxidation of bimetallic Au–Cu/TiO_2 catalysts prepared by deposition–precipitation with urea. *Appl. Catal. B* **2013,** *140-141*, 363.

(35) Yang, S.; Chai, J.; Song, Y.; Fan, J.; Chen, T.; Wang, S.; Yu, H.; Li, X.; Zhu, M. In situ two-phase ligand exchange: A new method for the synthesis of alloy nanoclusters with precise atomic structures. *J. Am. Chem. Soc.* **2017,** *139* (16), 5668.

(36) Yamamoto, H.; Yano, H.; Kouchi, H.; Obora, Y.; Arakawa, R.; Kawasaki, H. N,N-Dimethylformamide-stabilized gold nanoclusters as a catalyst for the reduction of 4-nitrophenol. *Nanoscale* **2012,** *4* (14), 4148.

(37) Wand, P.; Kratzer, E.; Heiz, U.; Cokoja, M.; Tschurl, M. High stability of thiol-protected colloidal platinum nanoparticles with reduced ligand coverages in the hydrogenation of 3-hexyne. *Catal. Commun.* **2017,** *100*, 85.

(38) Tsunoyama, H.; Ichikuni, N.; Sakurai, H.; Tsukuda, T. Effect of electronic structures of au

clusters stabilized by poly(N-vinyl-2-pyrrolidone) on aerobic oxidation catalysis. *J. Am. Chem. Soc.* **2009,** *131* (20), 7086.

(39) von Issendorff, B.; Palmer, R. E. A new high transmission infinite range mass selector for cluster and nanoparticle beams. *Rev. Sci. Instrum.* **1999,** *70* (12), 4497.

(40) Meitzner, G.; Via, G. H.; Lytle, F. W.; Sinfelt, J. H. Structure of bimetallic clusters. Extended x-ray absorption fine structure (EXAFS) studies of Ag–Cu and Au–Cu clusters. *J. Chem. Phys.* **1985,** *83* (9), 4793.

(41) Kresse, G.; Furthmüller, J. Efficient iterative schemes for ab initio total-energy calculations using a plane-wave basis set. *Phys. Rev. B* **1996,** *54*, 11169.

(42) Kresse, G.; Furthmüller, J. Efficiency of ab-initio total energy calculations for metals and semiconductors using a plane-wave basis set. *Comput. Mater. Sci.* **1996,** *6*, 15.

(43) Chang, C. M.; Chou, M. Y. Alternative low-symmetry structure for 13-atom metal clusters. *Phys. Rev. Lett.* **2004,** *93* (13), 133401.

(44) Longo, R. C.; Gallego, L. J. Structures of 13-atom clusters of fcc transition metals by *ab initio* and semiempirical calculations. *Phys. Rev. B* **2006,** *74* (19), 193409.

(45) Sadakiyo, M.; Heima, M.; Yamamoto, T.; Matsumura, S.; Matsuura, M.; Sugimoto, S.; Kato, K.; Takata, M.; Yamauchi, M. Preparation of solid-solution type Fe-Co nanoalloys by synchronous deposition of Fe and Co using dual arc plasma guns. *Dalton Trans.* **2015,** *44* (36), 15764.

(46) Suzuki, S.; Tomita, Y.; Kuwabata, S.; Torimoto, T. Synthesis of alloy AuCu nanoparticles with the $L1_0$ structure in an ionic liquid using sputter deposition. *Dalton Trans.* **2015,** *44* (9), 4186.

(47) Ferrando, R.; Jellinek, J.; Johnston, R. L. Nanoalloys: From theory to applications of alloy clusters and nanoparticles. *Chem. Rev.* **2008,** *108*, 845.

(48) Rao, J. L.; Chaitanya, G. K.; Basavaraja, S.; Bhanuprakash, K.; Venkataramana, A. Density-functional study of Au–Cu binary clusters of small size (n=6): Effect of structure on electronic properties. *J. Mol. Struct. (THEOCHEM)* **2007,** *803* (1-3), 89.

(49) Ozoliņš, V.; Wolverton, C.; Zunger, A. Cu-Au, Ag-Au, Cu-Ag, and Ni-Au intermetallics: First-principles study of temperature-composition phase diagrams and structures. *Phys. Rev. B* **1998,** *57*, 6427.

(50) Denton, A. R.; Ashcroft, N. W. Vegard's law. *Phys. Rev. A* **1991,** *43* (6), 3161.

(51) Yin, F.; Wang, Z. W.; Palmer, R. E. Controlled formation of mass-selected Cu-Au core-shell cluster beams. *J. Am. Chem. Soc.* **2011,** *133* (27), 10325.

(52) Hai, Z.; El Kolli, N.; Chen, J.; Remita, H. Radiolytic synthesis of Au–Cu bimetallic nanoparticles supported on TiO_2: application in photocatalysis. *New J. Chem.* **2014,** *38* (11), 5279.

(53) Pauwels, B.; Van Tendeloo, G.; Zhurkin, E.; Hou, M.; Verschoren, G.; Theil Kuhn, L.; Bouwen, W.; Lievens, P. Transmission electron microscopy and Monte Carlo simulations of ordering in Au-Cu clusters produced in a laser vaporization source. *Phys. Rev. B* **2001,** *63* (16), 165406.

(54) Yasuda, H.; Mori, H. Effect of cluster size on the chemical ordering in nanometer-sized Au-75at % Cu alloy clusters. *Z. Phys. D* **1996,** *37*, 181.

(55) Chen, S.; Jenkins, S. V.; Tao, J.; Zhu, Y.; Chen, J. Anisotropic seeded growth of Cu–M (M = Au, Pt, or Pd) bimetallic nanorods with tunable optical and catalytic properties. *J. Phys. Chem.*

C **2013,** *117* (17), 8924.

(56) Mejia-Rosales, S. J.; Fernandez-Navarro, C.; Perez-Tijerina, E.; Blom, D. A.; Allard, L. F.; Jose-Yacaman, M. On the structure of Au/Pd bimetallic nanoparticles. *J. Phys. Chem. C* **2007,** *111*, 1256.

(57) Wang, Z. W.; Palmer, R. E. Intensity calibration and atomic imaging of size-selected Au and Pd clusters in aberration-corrected HAADF-STEM. *J. Phys: Conf. Ser.* **2012,** *371*, 012010.

(58) Layek, K.; Kantam, M. L.; Shirai, M.; Nishio-Hamane, D.; Sasaki, T.; Maheswaran, H. Gold nanoparticles stabilized on nanocrystalline magnesium oxide as an active catalyst for reduction of nitroarenes in aqueous medium at room temperature. *Green Chem.* **2012,** *14* (11), 3164.

(59) Wunder, S.; Lu, Y.; Albrecht, M.; Ballauff, M. Catalytic activity of faceted gold nanoparticles studied by a model reaction: evidence for substrate-induced surface restructuring. *ACS Catal.* **2011,** *1* (8), 908.

(60) Ansar, S. M.; Kitchens, C. L. Impact of gold nanoparticle stabilizing ligands on the colloidal catalytic reduction of 4-nitrophenol. *ACS Catal.* **2016,** *6* (8), 5553.

(61) Menumerov, E.; Hughes, R. A.; Neretina, S. Catalytic reduction of 4-nitrophenol: A quantitative assessment of the role of dissolved oxygen in determining the induction time. *Nano Lett.* **2016,** *16* (12), 7791.

(62) Zhang, Q.; Blom, D. A.; Wang, H. Nanoporosity-enhanced catalysis on subwavelength Au nanoparticles: a plasmon-enhanced spectroscopic study. *Chem. Mater.* **2014,** *26* (17), 5131.

(63) Ismail, A. A.; Hakki, A.; Bahnemann, D. W. Mesostructure Au/TiO_2 nanocomposites for highly efficient catalytic reduction of p-nitrophenol. *J. Mol. Catal. A: Chem.* **2012,** *358*, 145.

(64) Zhang, J.; Chen, G.; Chaker, M.; Rosei, F.; Ma, D. Gold nanoparticle decorated ceria nanotubes with significantly high catalytic activity for the reduction of nitrophenol and mechanism study. *Appl. Catal. B* **2013,** *132*, 107.

(65) Deka, P.; Deka, R. C.; Bharali, P. In situ generated copper nanoparticle catalyzed reduction of 4-nitrophenol. *New J. Chem.* **2014,** *38* (4), 1789.

(66) Zhang, P.; Sui, Y.; Xiao, G.; Wang, Y.; Wang, C.; Liu, B.; Zou, G.; Zou, B. Facile fabrication of faceted copper nanocrystals with high catalytic activity for p-nitrophenol reduction. *J. Mater. Chem. A* **2013,** *1* (5), 1632.

CHAPTER 4

A Validation Study of a New Type of Cluster Beam Source in Vapour-Phase Catalysis Applications

In this chapter, the catalytic performance of the cluster catalysts (Pd clusters supported on diced carbon tapes) made with a new type of cluster beam source, MACS, is demonstrated in selective hydrogenation of 1-pentyne to 1-pentene in vapour phase. The cluster size evolution before and after the reaction is explored by STEM and linked with the cluster activity and stability. The idea of this research was proposed by Richard Palmer and Peter Ellis. I performed the sample preparation, characterization and catalysis measurements. Thibaut Mathieu and Vitor T. A. Oiko provided Au, Pd/Au cluster samples and training on the cluster beam source. The catalysis measurements were conducted under the supervision of Christopher M. Brown and Peter Ellis. Peter Ellis also prepared reference samples (by impregnation) with me. Some data from this chapter are used in a review paper, which has been published in Accounts of Chemical Research: *Synthesis without solvents: the cluster (nanoparticle) beam route to catalysts and sensors, Accounts of Chemical Research, 2018, 51, 2296-2304; doi: 10.1021/acs.accounts.8b00287.*

4.1 Introduction

As we mentioned in section 1.4, the cluster beam deposition exhibits various advantages over chemical methods including precise size and composition control; no involvement of any solvents; and absence of ligands etc., but its application in making practical catalysts is still held back by the low deposition rate. To overcome this bottleneck, a new type of cluster beam source, MACS, was recently developed, which increases the cluster flux by several orders of magnitude and could be further scaled up.[1-2] The cluster atoms in MACS are firstly assembled within a solid Ar matrix and then sputtered by a high current beam of ions. Although the enhanced high deposition rate and the mechanism of this new technique have been investigated both experimentally[1-4] and theoretically,[5] the catalytic performance of the cluster catalysts produced, especially under the realistic reaction conditions, is still not clear. The increased cluster deposition rate might cause other problems such as surface aggregation that can counteract the benefit of high cluster flux for catalytic reactions. In addition, since an Ar ion beam is employed to sputter the matrix, the formed clusters might also be affected by the ion beam causing a different surface coordination compared with the clusters formed by gas condensation and chemical methods, which might lead to a different cluster activity. Therefore, direct catalytic validation of the cluster catalysts made in MACS is highly desired.

Selective hydrogenation of alkyne to alkene is an important reaction (see **Figure 4.1**), as it produces a high purity alkene steam which is widely used in the petrochemical industry and synthesis of different polymers.[6-8] Among all the transition metal catalysts, Pd is reckoned as an efficient catalyst for this hydrogenation reaction with relatively high selectivity.[9-11] Recently, its selectivity was found to be associated with two factors. One is the Pd-C sub-surface layers formed by carbon dissolving during the reaction.[12-13] These Pd-C sub-surface layers can block or slow the diffusion of the dissolved hydrogen (in the hydride form) to the catalyst surface,[14-15] which is much more active than the surface adsorbed hydrogen and usually leads to full hydrogenation. Those metals with high hydrogen storage ability usually exhibit low selectivity, e.g. Ni and Pt.[16] Pd catalysts supported on carbon exhibiting much higher selectivity than those on oxide supports also demonstrates that the involvement of carbon can significantly improve the catalytic selectivity.[17] The second factor is the density of the active sites on the cluster surface. It is found that when Pd clusters alloy with another element (less active than Pd), the active sites on the cluster surface can be diluted according to the composition.[14] These isolated active sites decrease the density of di-σ-adsorbed alkenes (the opened carbon-carbon triple bonds bind with two active sites) which correlates to the further hydrogenation and need the involvement of the neighboring sites.[18-19] Based on this understanding, some alloy systems are proposed to improve the selectivity such as Pd/Au binary clusters.[20-21] Cluster beam deposition provides opportunities to produce clean clusters (without ligands), which makes it possible to explore clusters' original activity and selectivity.

In this study, we choose vapour-phase 1-pentyne hydrogenation as the model catalytic reaction and carbon supported ultrafine Pd and Pd/Au clusters (1-1.5 nm) as the catalytic particles to validate our new cluster beam source in catalysis applications.

To avoid surface aggregation, the carbon supports are pre-sputtered by an Ar ion beam to generate point defects on the surface, which can anchor clusters. A dicing technique[22] is adopted to transform cluster decorated carbon tape supports to catalyst powders. Their catalytic activity for 1-pentyne hydrogenation was assessed under realistic reaction conditions and compared with the Pd reference sample made by wet impregnation. It was shown that the Pd cluster catalyst made by MACS has a similarly high selectivity (~95%) as the Pd reference sample but the activity (in terms of per unit weight) is much higher. The investigation on their cluster size evolution before and after the reaction disclosed that the observed higher activity over the Pd cluster catalysts was associated with the smaller size (larger specific surface area) and better stability against sintering than the Pd reference sample. Moreover, by comparing the activity (per surface atom) of Pd clusters with Pd/Au alloy clusters from MACS, it was found that alloying Au atoms with Pd clusters did not enhance the cluster activity, which could be attributed to the surface re-arrangements driven by oxidation in air, leading to a similar Pd surface as pure Pd clusters. Therefore, our study validates the catalytic performance of the cluster catalysts made by MACS and demonstrates a new method to produce physically deposited cluster catalysts.

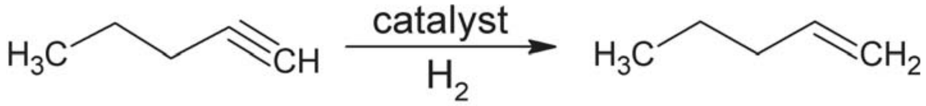

Figure 4.1 Reaction scheme of 1-pentyne hydrogenation

4.2 Experimental section

Three kinds of cluster catalysts (Pd, Pd/Au and Au cluster catalyst) were produced using a prototype MACS as shown in **Figure 2.9**, which consists of two sections: matrix generation chamber and cluster deposition chamber. Detailed information has been introduced in section 2.1.2 and a previous report.[3] The cluster formation process can be briefly summarized by two steps, i) matrix generation, and ii) matrix sputtering. In the matrix generation chamber, the vaporized metal atoms (from a thermal evaporator and/or an e-beam evaporator) co-condensed with Ar gas to form a solid matrix (metal concentration: ~ 4at%) on the matrix support. An Ar ion beam (1.5 keV, ~30 μA) was then employed to sputter the matrix, causing the clusters nucleate and/or ripen. The ejected clusters were collected by diced carbon tape supports loaded onto a carousel with a typical surface coverage of ~10% (8 min per slide) to reduce surface aggregation. A dicing technique[22] was adopted to transform clusters deposited carbon tape supports into the powder catalysts, as shown schematically in **Figure 2.10**. Before the cluster deposition, carbon tape supports were cut mechanically with a cutting depth of 0.1 mm and cutting pitch of 1 mm by a diamond saw to generate groves on the surface. Then the diced carbon tapes were pre-sputtered with an Ar^+ beam (~10 μA, ~30 s), causing point defects formed on carbon surface to immobilize clusters. After cluster deposition, the topmost layers of the carbon tape were scraped off by a scalpel to obtain catalyst powders. Pd (Au) clusters were prepared by sputtering a Pd-Ar (Au-Ar) matrix with the metal concentration of ~4%, the same as Pd/Au binary clusters (Pd/Au ratio: ~1/1). The preparation of the Pd reference sample and catalysis measurements were described in section 2.3.2 and section 2.4.2, respectively.

The size distribution and atomic structure of the produced clusters (Pd, Pd/Au and Au) were examined by a JEOL JEM-2100F STEM equipped with a Cs corrector (CEOS) at a convergence angle of 20 mrad and a HAADF detector operating with an inner angle of 62 mrad and an outer angle of 164 mrad at 200 kV. The elemental composition was characterized by EDS in STEM.

4.3 Results and discussions

4.3.1 Analysis of the cluster catalysts before 1-pentyne hydrogenation

The cluster diameter distribution of the cluster catalysts is characterized by STEM. **Figure 4.2** shows the typical HAADF-STEM images and corresponding cluster diameter distribution of the following samples before reaction: Pd cluster on carbon (a), Pd/Au cluster on carbon (b), Au cluster on carbon (c) and Pd reference on carbon (d). The three MACS samples have the similar cluster diameter between 1.2 nm and 1.4 nm (with the variation in diameter of 30%-35%). No significant surface aggregation is observed since clusters were deposited with a relatively low surface coverage (~10%) and immobilized by pre-sputtered point defects.[23-24] For the Pd reference sample, the clusters are much larger (~ 2.38 nm) and broader (variation in diameter: 108%) than the MACS samples, which is traceable to the calcination process at high temperature. The metal loading of the cluster catalysts is estimated by measuring the cluster density and cluster size of the as-deposited clusters (on TEM grids) as well as the total mass of the obtained catalyst powders (see section 2.2.6). For the MACS samples, the metal loading

(~ 1 g catalyst powders) is calculated to be (0.00072 ± 0.00009)wt%, (0.00070 ± 0.00004)wt%, (0.00163 ± 0.00030)wt% for Pd cluster catalyst, Pd/Au cluster catalyst and Au cluster catalyst, respectively. Compared with the catalyst used in industry (metal loading: 1wt%-5wt%), the mass metal loading of the MACS samples is still quite low, but it could be further increased by decreasing the cutting depth on the carbon tape or depositing clusters on thin films (evaporated oxides film etc.). The studies on the co-deposition of clusters and supports to increase cluster loading are under way.

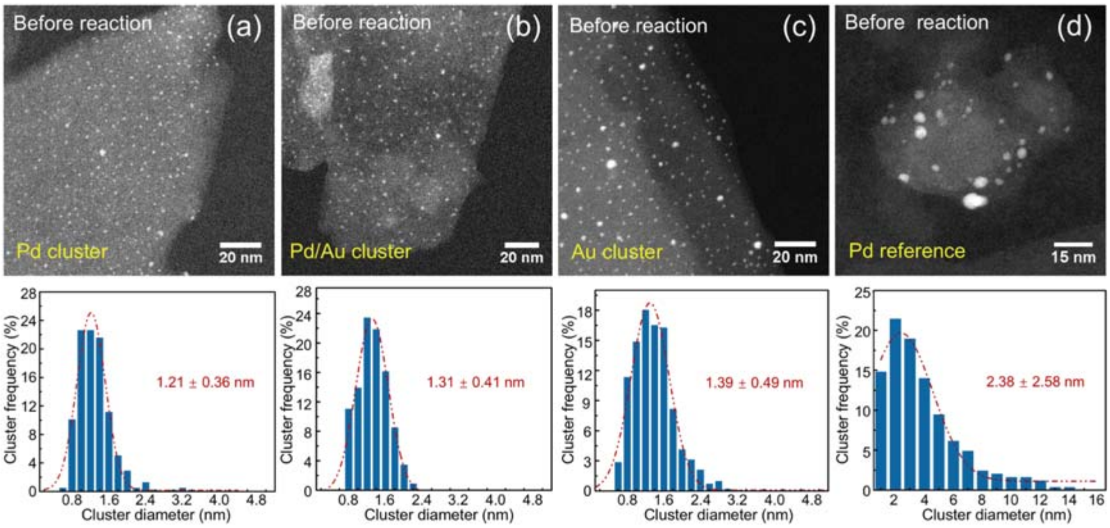

Figure 4.2 Typical HAADF images and cluster diameter distribution of the cluster catalysts made by MACS and Pd reference sample made by wet impregnation before 1-pentyne hydrogenation. (a) Pd cluster on carbon, (b) Pd/Au cluster on carbon, (c) Au cluster on carbon, (d) Pd reference on carbon. Compared with the reference sample, the clusters made from MACS are much smaller and the distribution is much narrower.

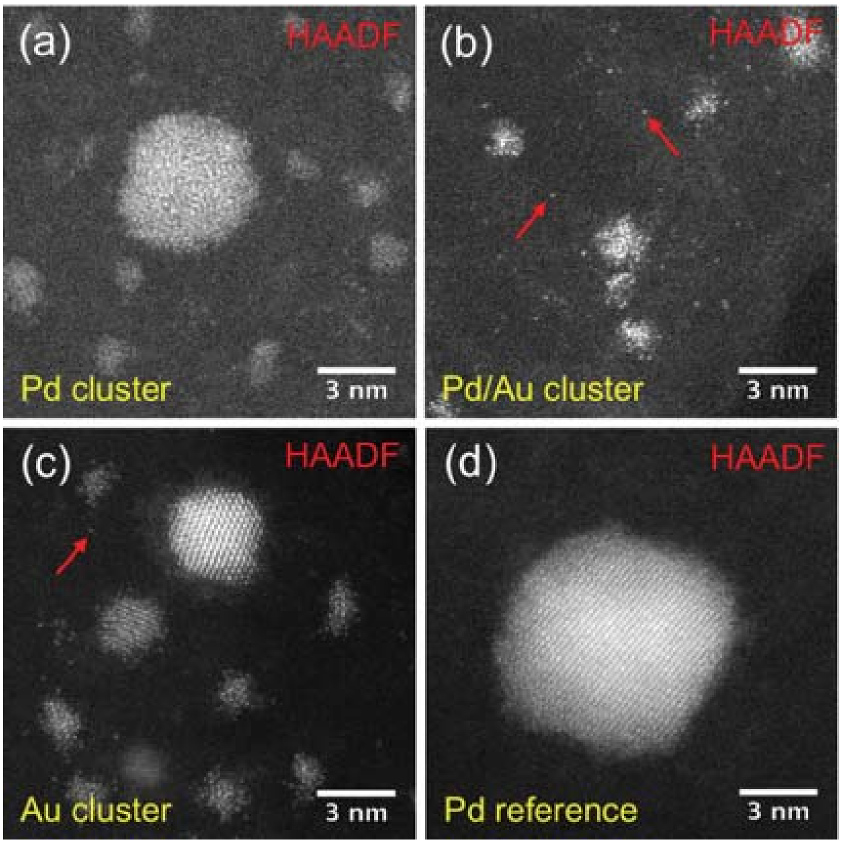

Figure 4.3 Typical high-resolution HAADF images of the cluster catalysts and Pd reference sample showing the cluster atomic structure before hydrogenation. (a) Pd cluster on carbon, (b) Pd/Au cluster on carbon, (c) Au cluster on carbon, (d) Pd reference on carbon. Most of the clusters in the MACS samples have an amorphous structure without ordered patterns, whereas for the reference sample, most of them are crystalline. The red arrows in (b) and (c) indicate the single atoms formed by electron beam irradiation while imaging.

To clarify the atomic structure of the cluster catalysts before reaction, high-resolution HAADF STEM images were obtained as shown in **Figure 4.3**. Most of the clusters in the MACS samples have an amorphous structure without clear ordered patterns. Although some crystalline structures are observed in Au clusters, they usually appear in bigger clusters. Whereas for the Pd reference sample, the clusters are much larger and most of them exhibit a crystalline structure due to the calcination at high temperature. Some single atoms near the clusters (marked by red arrows in **Figures 4.3** (b) and (c)) are also observed, which are formed by electron beam irradiation while imaging. It should be noted that since the Pd/Au clusters before reaction are very small, the atomic arrangements of Pd and Au in the clusters (core-shell, alloy or Janus structure) are not stable under the electron beam[25] and could not be distinguished from the intensity contrast. However, the chemical composition of the cluster catalysts after reaction were successfully obtained by EDS point spectra, which confirmed that only Pd signals were detected from Pd clusters, but both Pd and Au signals were found from Pd/Au clusters. The typical EDS spectra are shown in **Figure 4.4**, where the Cu signal comes from the Cu TEM grids.

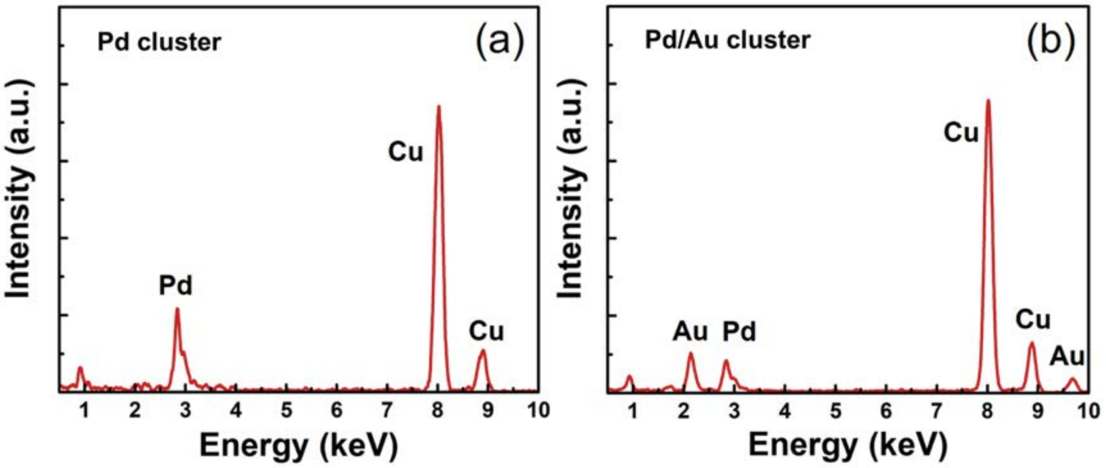

Figure 4.4 Typical EDS spectra from a Pd cluster and a Pd/Au cluster after reaction, which confirm that only Pd signal is detected from Pd clusters, but both Pd and Au signals are found from Pd/Au clusters. The Cu signal comes from the TEM grid.

4.3.2 Evaluation of the catalytic performance for 1-pentyne hydrogenation

All the produced catalysts and a blank carbon tape support (30 mg for each measurement) were tested in a tube reactor for selective hydrogenation of 1-pentyne in vapour phase. **Figure 4.5** shows the catalytic performance as a function of the reaction temperature. For the 1-pentyne conversion rate, it is obvious that the blank carbon tape support and Au cluster catalyst were not active for this reaction even at the temperature of 220^{o}C. Although Au clusters have been reported to be active for alkyne hydrogenation, the activity is much lower than Pd clusters and usually observed with a high metal loading.[26-29] As a contrast, prominent activities were observed from the Pd, Pd/Au cluster catalysts and Pd reference sample. Overall, the activities for these three samples increased with the elevated temperature, but the Pd cluster catalyst showed a higher 1-pentyne conversion rate of ~ 65% at 220^{o}C than Pd/Au cluster catalyst (~45%) and Pd reference sample (~25%), which is consistent with the smallest cluster size observed from STEM. Considering the metal loading of these three samples are almost the same, a smaller cluster size can provide more active sites on the surface per unit weight, thus leading to a higher activity. It should be mentioned that a lower light-off temperature (75 ^{o}C) was found from the Pd reference sample compared with Pd cluster catalysts (140 ^{o}C), suggesting a proportion of catalyst particles in the reference sample were active at lower temperature. **Figure 4.5(b)** shows the 1-pentene selectivity *versus* reaction temperature for Pd, Pd/Au cluster catalysts and Pd reference sample. Since Pd and Pd/Au cluster catalysts were only active at the temperature above 130 ^{o}C, their selectivity was thus plotted in the range of 130 to 230^{o}C. All these three samples showed comparable excellent 1-pentene selectivity (above 94%), but it is slightly higher for the Pd reference sample due to the lower conversion rate.

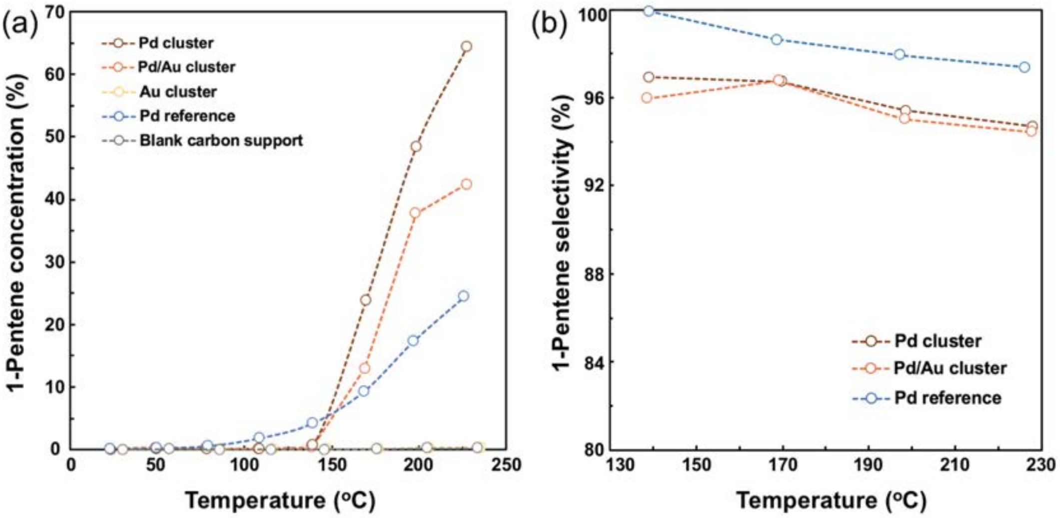

Figure 4.5 Vapour-phase selective 1-pentyne hydrogenation as a function of the reaction temperature over the produced cluster catalysts, Pd reference sample and blank carbon tape support. (a) Comparison of 1-pentyne conversion rate. (b) 1-pentene selectivity in the range of 130-230°C. The selectivity was calculated by the concentration of 1-pentene and concentration of all the products using $C_{1\text{-pentene}}/C_{products}$. The Pd cluster catalyst shows the highest 1-pentyne conversion rate at temperature of 220°C with competitive excellent 1-pentene selectivity.

The long-term durability is an important factor that determines a catalyst to be used in vapour-phase reaction. The durability of these three active samples was assessed by testing at 220°C for 6 hours. **Figure 4.6** shows the 1-pentyne conversion rate and 1-pentene selectivity over the reaction time. In general, the activities of all the samples decreased with the reaction time, which are associated with the formed cokes[30-31] (due to the reaction) on the cluster surface blocking active sites and sintering[7, 32] causing decreased cluster surface area. The Pd cluster catalyst again exhibited the highest activity compared with Pd/Au cluster catalyst and Pd reference sample, but since the samples were kept at 220 °C for a while before introducing reagent gases, the initial 1-pentyne conversion rate did not achieve the same values as shown in **Figure 4.5**. The durability of the catalysts was evaluated by the product half yield life time (with respect to the peak value), which is around 135, 120 and 90 min for Pd, Pd/Au cluster catalysts and Pd reference sample, respectively. This indicates that the Pd cluster catalyst is more stable against sintering than the other two samples. As for the 1-pentene selectivity, all the samples can sustain a high selectivity above 92% at least for 6 hours.

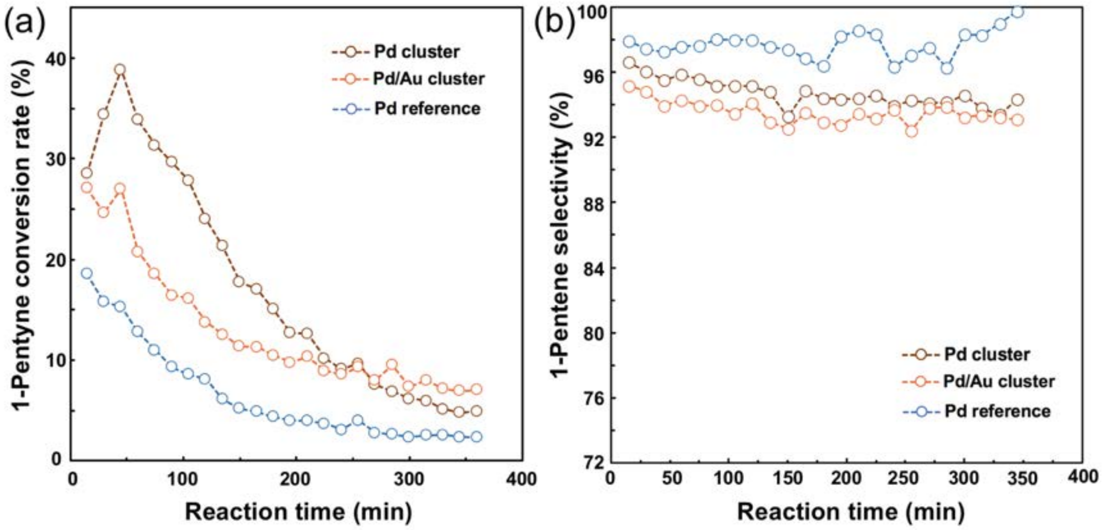

Figure 4.6 Stability test of the Pd cluster catalyst, Pd/Au cluster catalyst and Pd reference sample for 1-pentyne hydrogenation over 6 hours at 220°C. (a) 1-pentyne conversion rate and (b)1-pentene selectivity as a function of reaction time.

4.3.3 Analysis of the cluster catalysts after 1-pentyne hydrogenation

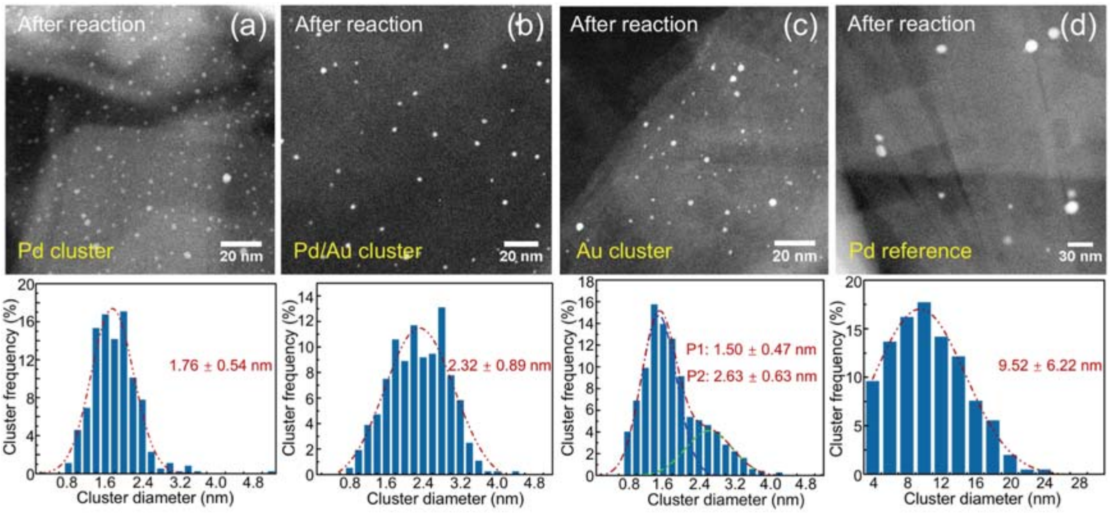

Figure 4.7 Typical HAADF images and cluster diameter distribution of the cluster catalysts and Pd reference sample after 1-pentyne hydrogenation (for 1 hour). (a) Pd cluster on carbon, (b) Pd/Au cluster on carbon, (c) Au cluster on carbon, (d) Pd reference on carbon. Compared with the Pd reference sample, the MACS samples exhibited much better stability against sintering with smaller changes in diameter.

To further understand their catalytic behaviour, the cluster diameter distribution after reaction was also obtained as shown in **Figure 4.7**. When compared with the samples before reaction, the cluster diameter of all the samples increased, but the MACS samples underwent a much weaker sintering than the Pd reference sample, which could attribute to the pre-sputtered defects immobilizing the clusters from MACS. The sintering process was also consistent with the STEM observations that the cluster density on the carbon flakes decreased after the reaction. It should be noted that in the three MACS samples, the Pd cluster showed the smallest change in diameter which could explain the observed longest durability during the catalytic reaction. Whereas the pure Au cluster exhibiting a bi-distribution model with the second peak at 2.63 nm, larger than the diameter of Pd (1.76 nm) and Pd/Au clusters (2.32 nm), suggests that the Au cluster has a higher diffusion rate on carbon than Pd cluster due to the weak interaction with carbon. As for the Pd/Au cluster, its diameter change was in between Pd and Au clusters, indicating the addition of Au atoms to Pd clusters decreased the cluster stability by enhancing diffusion.

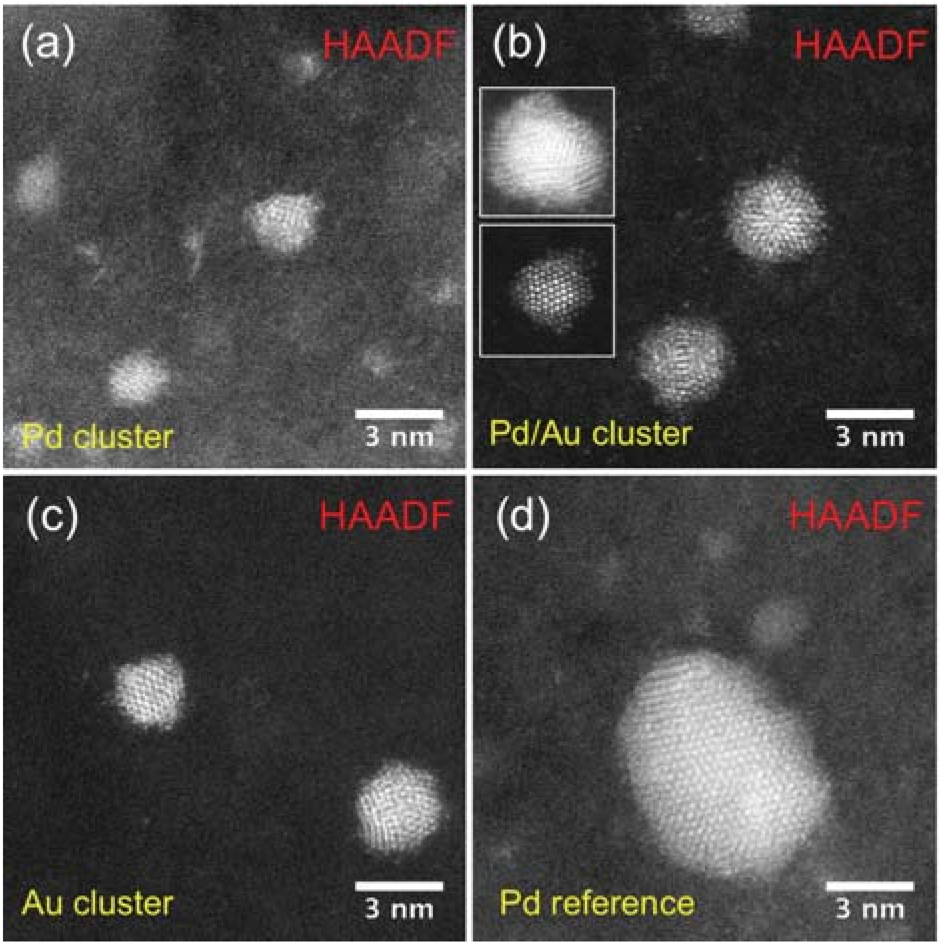

Figure 4.8 Typical high-resolution HAADF images of the cluster catalysts and Pd reference sample showing the cluster atomic structure after hydrogenation. (a) Pd clusters on carbon, (b) Pd/Au clusters on carbon, (c) Au clusters on carbon, (d) Pd reference on carbon. The insets show Pd-Au clusters with clear core-shell structure.

Figure 4.8 shows typical high-resolution HAADF STEM images of the cluster catalysts after reaction. More clusters in the MACS samples show crystalline structure and the shape becomes more spherical, compared with the clusters before reaction. It should be emphasized that in the Pd/Au sample, a small portion of the clusters with a clear core/shell structure were also observed as shown in the insets to **Figure 4.8(b)**. These core-shell clusters have a brighter core in the middle, suggesting a higher proportion of Au in the core. In addition to these core/shell clusters, more clusters have a darker ring surrounded compared with the pure Au clusters (see **Figure 4.8(b)**), but it is difficult to determine whether it is due to the composition effect (smaller Au proportion) and/or thickness effect (less metal atoms).

4.3.4 Discussion of the cluster activity for 1-pentyne hydrogenation

The catalysis measurements showed that the Pd cluster catalyst is more active (per unit weight) than the Pd reference sample and Pd/Au cluster catalyst. Considering the difference in cluster size, the superior activity could potentially be explained by the size effect that smaller clusters have a larger specific surface area, so more surface Pd atoms can be involved in the reaction. In this context, it is important to clarify: i) whether the surface Pd atoms from MACS (smaller clusters) are more active than those made from wet impregnation (larger clusters), assuming the same surface area; ii) the role of the added Au atoms to the Pd cluster for this reaction. To reveal the answer, the 1-pentene formation rate was replotted as a basis of per surface atom, as shown in **Figure 4.9**. In processing this conversion, the fitted diameter distribution (by a Gaussian function) of the catalyst particles before reaction was used to calculate the total surface atoms, since the wide diameter distribution for Pd reference sample might mislead the results when using the mean cluster size.

It is obvious that the Pd reference sample is about two times more active (initial activity) than the Pd cluster catalyst in terms of activity per surface atom, which indicates the surface Pd atoms made from impregnation (larger Pd clusters) are more active than those made from MACS (smaller Pd clusters). The observed lower light-off temperature from Pd reference sample can also confirm this conclusion. Two explanations, here, are deduced to account for this “size effect”. One is the ratio of the different types of surface atoms, determining the binding mode of the 1-pentyne to Pd clusters, is different for clusters of different sizes.[26, 33] Larger clusters usually have more surface atoms in the crystal plane (terrace atoms), which benefit for the two carbon atoms from C≡C triple bonds to bind with two proximate Pd atoms[34] (see the inset to **Figure 4.9**, type A). This bonding mode provides a lower energy barrier to open C≡C triple bonds, thus is more active for hydrogenation. Whereas for the smaller clusters, more surface atoms exist on the corner or edge, which are more likely to provide one binding site for 1-pentyne adsorption (through one carbon atom, see the inset to **Figure 4.9**, type B). Compared with the binding through two carbon atoms, this binding mode has a higher energy barrier to break C≡C triple bonds.[33] Another explanation is that the steric hindrance for the two binding modes is different. For the binding through two carbon atoms, it needs larger space for 1-pentyne molecules to lie on the cluster surface, better accommodated on larger clusters. Whereas for the binding through one carbon atom, since the molecule is perpendicular to the cluster surface, it requires less space, and could dominate in smaller clusters. Therefore, surface Pd atoms on larger clusters are more active than those on smaller clusters.

In addition, a similar cluster activity per surface atom was observed from pure Pd clusters and Pd/Au binary clusters, suggesting the addition of Au atoms to Pd cluster did not enhance the cluster activity. One possible reason is that the oxidation could drive Pd atoms to the cluster surface when the samples were kept in air. So, the Pd/Au binary clusters actually have a similar Pd surface as the pure Pd clusters, thus leading to the similar activity per surface atom. The oxidization driven atomic re-arrangements have been reported in many bimetallic clusters, such as Ag/Au[35] and Au/Cu.[36] In addition, compared with the Pd cluster catalyst, the selectivity of Pd/Au clusters is not further increased after introducing Au, which might also indicate a similar cluster surface as the Pd clusters. Although the synergetic effect was not found in Pd/Au binary clusters, this study provides a way to decrease the catalyst cost by constructing a core/shell structure with a cheaper metal in the core.

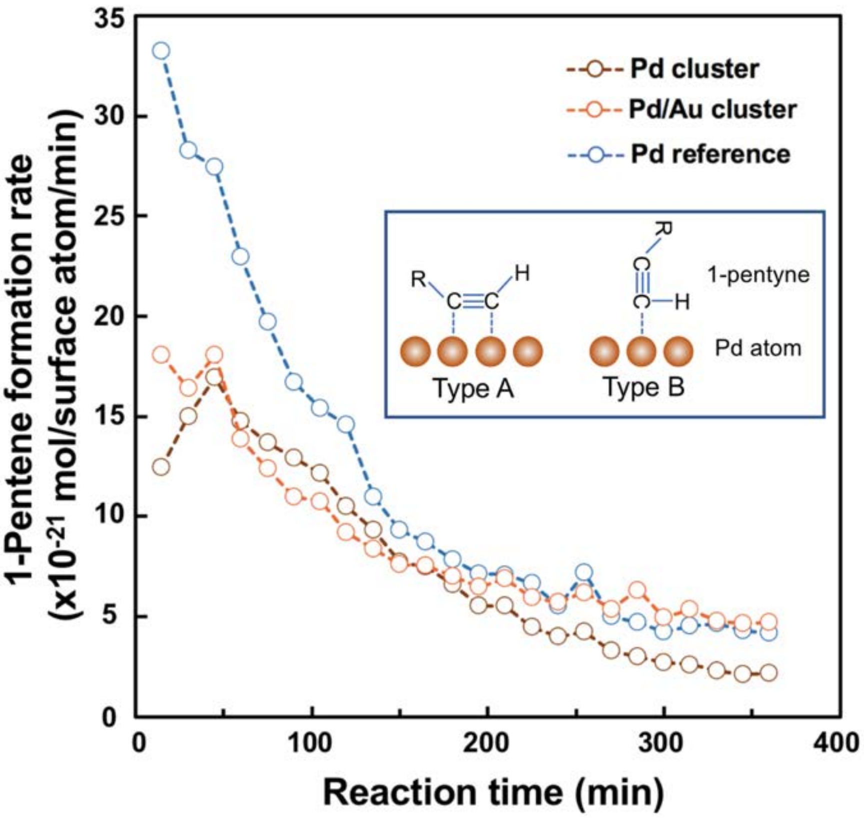

Figure 4.9 Comparison of the catalytic activity as a basis of per surface atom for 1-pentyne hydrogenation at 220°C. The inset shows two binding modes when a 1-pentyne molecule is adsorbed on a Pd cluster.

4.4 Conclusions

In conclusion, we have validated the catalytic performance of Pd cluster catalysts made by MACS for a model catalytic reaction, selective 1-pentyne hydrogenation. Their catalytic activity was compared with a Pd reference sample made by wet impregnation. The catalytic results showed that the Pd cluster catalyst is more active (per unit weight) and more stable than the Pd reference sample. Aberration-corrected STEM characterizations on their cluster size evolution before and after reaction demonstrated that the observed robust activity for the Pd cluster catalyst was rendered by the pre-sputtered defects, which immobilized the clusters on the support. And the superior catalytic activity could be associated with the smaller cluster size than the Pd reference sample, which provided more specific surface area for the reaction. However, it was also found that the surface Pd atoms from a larger Pd cluster are more active than those from a smaller cluster. This is because compared with smaller Pd clusters, 1-pentyne molecules are more likely to bind to larger clusters accommodating a lower-energy-barrier mode (carbon-carbon triple bonds lie on the cluster surface). In addition, no synergetic effect was found in Pd/Au cluster catalyst. The observed similar activity (per surface atom) from the Pd and Pd/Au cluster catalysts could be attributed to surface oxidation, which can drive the Pd atoms to the cluster surface, thus forming a similar Pd surface as pure Pd clusters. Our study presented a new method to make physically deposited practical cluster catalysts with high catalytic activity.

References

(1) Palmer, R. E.; Cao, L.; Yin, F. Note: Proof of principle of a new type of cluster beam source with potential for scale-up. *Rev. Sci. Instrum.* **2016,** *87* (4), 046103.

(2) P. R. Ellis; C. M. Brown; P. T. Bishop; J. Yin; K. Cooke; W. D. Terry; J. Liu; F. Yin; Palmer, R. E. The cluster beam route to model catalysts and beyond. *Faraday Discuss.* **2016,** *188*, 39.

(3) Cai, R.; Jian, N.; Murphy, S.; Bauer, K.; Palmer, R. E. A new method to prepare colloids of size-controlled clusters from a matrix assembly cluster source. *APL Mater.* **2017,** *5* (5), 053405.

(4) Oiko, V. T.; Mathieu, T.; Cao, L.; Liu, J.; Palmer, R. E. Note: Production of silver nanoclusters using a Matrix-Assembly Cluster Source with a solid CO_2 matrix. *J. Chem. Phys.* **2016,** *145* (16), 166101.

(5) Zhao, J.; Cao, L.; Palmer, R. E.; Nordlund, K.; Djurabekova, F. Formation and emission mechanisms of Ag nanoclusters in the Ar matrix assembly cluster source. *Phys. Rev. Materials* **2017,** *1*, 066002.

(6) Al-Herz, M.; Simmons, M. J. H.; Wood, J. Selective hydrogenation of 1-Heptyne in a mini trickle bed reactor. *Ind. Eng. Chem. Res.* **2011,** *51* (26), 8815.

(7) Chan, C. W.; Mahadi, A. H.; Li, M. M.; Corbos, E. C.; Tang, C.; Jones, G.; Kuo, W. C.; Cookson, J.; Brown, C. M.; Bishop, P. T.; Tsang, S. C. Interstitial modification of palladium nanoparticles with boron atoms as a green catalyst for selective hydrogenation. *Nat. Commun.* **2014,** *5*, 5787.

(8) Srimani, D.; Diskin-Posner, Y.; Ben-David, Y.; Milstein, D. Iron pincer complex catalyzed, environmentally benign, E-selective semi-hydrogenation of alkynes. *Angew. Chem. Int. Ed.* **2013,** *52* (52), 14131.

(9) Jia, J.; Haraki, K.; Kondo, J. N.; Domen, K.; Tamaru, K. Selective hydrogenation of acetylene over Au/Al_2O_3 catalyst. *J. Phys. Chem. B* **2000,** *104*, 11153.

(10) Venkatesan, R.; Prechtl, M. H. G.; Scholten, J. D.; Pezzi, R. P.; Machado, G.; Dupont, J. Palladium nanoparticle catalysts in ionic liquids: synthesis, characterisation and selective partial hydrogenation of alkynes to Z-alkenes. *J. Mater. Chem.* **2011,** *21* (9), 3030.

(11) Teschner, D.; Vass, E.; Havecker, M.; Zafeiratos, S.; Schnorch, P.; Sauer, H.; Knopgericke, A.; Schlogl, R.; Chamam, M.; Wootsch, A. Alkyne hydrogenation over Pd catalysts: A new paradigm. *J. Catal.* **2006,** *242* (1), 26.

(12) Hu, K. J.; Plant, S. R.; Ellis, P. R.; Brown, C. M.; Bishop, P. T.; Palmer, R. E. The effects of 1-pentyne hydrogenation on the atomic structures of size-selected Au_N and Pd_N ($N = 923$ and 2057) nanoclusters. *Phys. Chem. Chem. Phys.* **2014,** *16* (48), 26631.

(13) Yang, B.; Burch, R.; Hardacre, C.; Headdock, G.; Hu, P. Influence of surface structures, subsurface carbon and hydrogen, and surface alloying on the activity and selectivity of acetylene hydrogenation on Pd surfaces: A density functional theory study. *J. Catal.* **2013,** *305*, 264.

(14) Armbrüster, M.; Behrens, M.; Cinquini, F.; Föttinger, K.; Grin, Y.; Haghofer, A.; Klötzer, B.; Knop-Gericke, A.; Lorenz, H.; Ota, A.; Penner, S.; Prinz, J.; Rameshan, C.; Révay, Z.; Rosenthal, D.; Rupprechter, G.; Sautet, P.; Schlögl, R.; Shao, L.; Szentmiklósi, L.; Teschner, D.; Torres, D.; Wagner, R.; Widmer, R.; Wowsnick, G. How to control the selectivity of palladium-based catalysts in hydrogenation reactions: the role of subsurface chemistry. *ChemCatChem* **2012,** *4* (8), 1048.

(15) Teschner, D.; Borsodi, J.; Wootsch, A.; Révay, Z.; Hävecker, M.; Knop-Gericke, A.;

Jackson, S. D.; Schlögl, R. The roles of subsurface carbon and hydrogen in palladium-catalyzed alkyne hydrogenation. *Science* **2008,** *320*, 86.

(16) Delgado, J. A.; Benkirane, O.; Claver, C.; Curulla-Ferre, D.; Godard, C. Advances in the preparation of highly selective nanocatalysts for the semi-hydrogenation of alkynes using colloidal approaches. *Dalton Trans.* **2017,** *46* (37), 12381.

(17) Benavidez, A. D.; Burton, P. D.; Nogales, J. L.; Jenkins, A. R.; Ivanov, S. A.; Miller, J. T.; Karim, A. M.; Datye, A. K. Improved selectivity of carbon-supported palladium catalysts for the hydrogenation of acetylene in excess ethylene. *Appl. Catal., A* **2014,** *482*, 108.

(18) Doyle, A. Alkene chemistry on the palladium surface: nanoparticles vs single crystals. *J. Catal.* **2004,** *223* (2), 444.

(19) Shaikhutdinov, S.; Heemeier, M.; Bäumer, M.; Lear, T.; Lennon, D.; Oldman, R. J.; Jackson, S. D.; Freund, H. J. Structure–reactivity relationships on supported metal model catalysts: adsorption and reaction of ethene and hydrogen on Pd/Al_2O_3/NiAl(110). *J. Catal.* **2001,** *200* (2), 330.

(20) Wang, S.; Xin, Z.; Huang, X.; Yu, W.; Niu, S.; Shao, L. Nanosized Pd-Au bimetallic phases on carbon nanotubes for selective phenylacetylene hydrogenation. *Phys. Chem. Chem. Phys.* **2017,** *19* (8), 6164.

(21) Choudhary, T. V.; Sivadinarayana, C.; Datye, A. K.; Kumar, D.; Goodman, D. W. Acetylene hydrogenation on Au-based catalysts. *Catal. Lett.* **2003,** *86*, 1.

(22) Habibpour, V.; Song, M. Y.; Wang, Z. W.; Cookson, J.; Brown, C. M.; Bishop, P. T.; Palmer, R. E. Novel powder-supported size-selected clusters for heterogeneous catalysis under realistic reaction conditions. *J. Phys. Chem. C* **2012,** *116* (50), 26295.

(23) Claeyssens, F.; Pratontep, S.; Xirouchaki, C.; Palmer, R. E. Immobilization of large size-selected silver clusters on graphite. *Nanotechnology* **2006,** *17* (3), 805.

(24) Di Vece, M.; Palomba, S.; Palmer, R. E. Pinning of size-selected gold and nickel nanoclusters on graphite. *Phys. Rev. B* **2005,** *72* (7).

(25) Wells, D. M.; Rossi, G.; Ferrando, R.; Palmer, R. E. Metastability of the atomic structures of size-selected gold nanoparticles. *Nanoscale* **2015,** *7* (15), 6498.

(26) Nikolaev, S. A.; Smirnov, V. V. Synergistic and size effects in selective hydrogenation of alkynes on gold nanocomposites. *Catal. Today* **2009,** *147*, S336.

(27) Vile, G.; Perez-Ramirez, J. Beyond the use of modifiers in selective alkyne hydrogenation: silver and gold nanocatalysts in flow mode for sustainable alkene production. *Nanoscale* **2014,** *6* (22), 13476.

(28) Wagh, Y. S.; Asao, N. Selective transfer semihydrogenation of alkynes with nanoporous gold catalysts. *J. Org. Chem.* **2015,** *80* (2), 847.

(29) Li, G.; Jin, R. Gold nanocluster-catalyzed semihydrogenation: a unique activation pathway for terminal alkynes. *J. Am. Chem. Soc.* **2014,** *136* (32), 11347.

(30) Peña, J. A.; Herguido, J.; Guimon, C.; Monzón, A.; Santamaría, J. Hydrogenation of Acetylene over Ni/NiAl$_2$O$_4$Catalyst: Characterization, Coking, and Reaction Studies. *J. Catal.* **1996,** *159*, 313.

(31) Kennedy, D. R.; Webb, G.; Jackson, S. D.; Lennon, D. Propyne hydrogenation over alumina-supported palladium and platinum catalysts. *Appl. Catal., A* **2004,** *259* (1), 109.

(32) Bridier, B.; López, N.; Pérez-Ramírez, J. Partial hydrogenation of propyne over copper-based catalysts and comparison with nickel-based analogues. *J. Catal.* **2010,** *269* (1), 80.

(33) Semagina, N.; Renken, A.; Kiwi-Minsker, L. Palladium Nanoparticle Size Effect in 1-Hexyne Selective Hydrogenation. *J. Phys. Chem. C* **2007,** *111*, 13933.

(34) Crespo-Quesada, M.; Yarulin, A.; Jin, M.; Xia, Y.; Kiwi-Minsker, L. Structure sensitivity of alkynol hydrogenation on shape- and size-controlled palladium nanocrystals: which sites are most active and selective? *J. Am. Chem. Soc.* **2011,** *133* (32), 12787.

(35) Belić, D.; Chantry, R. L.; Li, Z. Y.; Brown, S. A. Ag-Au nanoclusters: Structure and phase segregation. *Appl. Phys. Lett.* **2011,** *99* (17), 171914.

(36) Yin, F.; Wang, Z. W.; Palmer, R. E. Ageing of mass-selected Cu/Au and Au/Cu core/shell clusters probed with atomic resolution. *J. Exp. Nanosci.* **2012,** *7* (6), 703.

CHAPTER 5

A New Method to Prepare Colloids of Size-Controlled Clusters from MACS

In this chapter, a facile and fast method for the production of colloidal suspensions of physically deposited size-controlled clusters is demonstrated, which is realised by depositing clusters onto a water-soluble polymer film and subsequently dissolving into solvents to produce a colloidal suspension. The catalytic properties of the colloids produced by this method were investigated by catalyzing 4-nitrophenol reduction over Pd colloids supported on TiO_2 powders. The idea of this work was proposed by Richard Palmer. I conducted the experiments of sample preparations, characterizations and catalysis measurements. William Terry installed the cluster source and Shane helped with the sample preparation. Nan Jian and Karl Bauer provided the reference sample of size selected Au_{923} clusters. The catalysis measurements were conducted in Johnson Matthey under the supervisions of Peter Ellis and Christopher Brown. Most of the results have been published in the paper (with me as the first author): *A new method to prepare colloids of size-controlled clusters from a matrix assembly cluster source, APL Materials, 5, 053405, 2017; doi: 10.1063/1.4977204.* In this chapter, most of the text and figures are taken or adapted from this paper.

5.1 Introduction

There is a burgeoning requirement for colloids of ultraprecise nanoparticles, particularly for life science applications[1-2] and liquid phase reactions,[3-4] where precise control of nanoparticle size, shape and composition is critical to delivering safe, consistent and efficient nanoparticle-based diagnostics for medical treatment[5] and tuning the catalytic properties for the colloid based catalysts.[6-8] Commercial colloids are produced by batch chemical processes where it can be difficult to precisely control size and dispersion, especially for the colloids below 5 nm. Variations between batches of the same product can arise due to small differences in the mixing or heating of the reagents. Moreover, developing new recipes for new nanomaterials through chemical synthesis routes can also be time-consuming and difficult. The physical production of nanoparticles using cluster beam technology offers the possibility to produce nanoparticles in an environmentally benign way (i.e. it does not involve hazardous chemicals or chemical waste), with unparalleled control over nanoparticle size and allows new nanomaterials to be developed more quickly than by chemical synthesis routes.[9-10]

In order to provide a storage and delivery solution suitable for life science applications and liquid phase catalytic reactions, a means of transferring the cluster beam-deposited nanoparticles into biocompatible colloidal suspensions is required. In this chapter, a proof-of-principle study of the preparation of colloidal suspensions of cluster beam-deposited size-controlled clusters is presented. This is realised by depositing clusters onto a water-soluble polymer film that is subsequently dissolved to produce a colloidal suspension where the polymer molecules encapsulate the clusters and stabilise them against aggregation. A key feature of this approach is that the clusters are pre-formed before dispersal in the colloidal suspension, as opposed to chemical synthesis where the nanoparticles are formed in solution and chemical concentration variations during preparation (e.g. during heating) can result in a heterogeneous product. There have been previous attempts to prepare colloids of physically deposited clusters by direct deposition into ionic liquids[11-12], silicon oil[13] and organic liquids such as castor oil.[14] However, the size control is quite limited due to the aggregation inside the liquid and moreover they are not suitable for life science applications.

Another difficulty limiting the use of cluster beam technology for colloid production is the fact that it is difficult to produce nanoparticles in sufficient quantities for commercial exploitation. Using conventional cluster beam technology, e.g. a mass-filtered gas aggregation source, it would take a prohibitively long time to produce even a small amount of colloid.[10, 15] This problem has recently been addressed with the development of the matrix assembly cluster source, which allows the production of large quantities of size-controlled clusters. For example, a sustained cluster beam current of the order of 1 μA has been demonstrated with the MACS, which is a 1000-fold increase over the cluster current typically obtained with a mass-filtered gas aggregation source. The principle of the MACS is illustrated in **Figures 5.1** (a) and (b), and has been described in detail elsewhere.[9, 16-17] Briefly, a target matrix comprising metal atoms embedded in a noble gas matrix is produced by physical vapour deposition of metal atoms onto a cryogenically-cooled support while simultaneously co-

condensing the noble gas. The matrix is subsequently sputtered with Ar ions to produce cascades of atomic collisions inside the matrix, causing clusters to nucleate and ripen before eventually being ejected from the matrix. The cluster size is controlled via the metal concentration inside the matrix, the matrix support temperature, and the sputter parameters. Size-controlled clusters can be deposited without the need for a subsequent mass-filtering step, which would invariably lead to significant loss of materials.

In addition, the catalytic activity of Pd colloids supported on TiO_2 powder produced by this new method was also investigated for catalyzing a liquid phase reaction, 4-nitrophenol reduction. The catalysis results show that Pd colloid catalyst exhibits a small catalytic activity for this reaction compared to bare clusters in the literature.[18] The low metal loading (0.05 wt%) and too many protecting polymers on the cluster surface (blocking the active sites) may account for this weak activity. We also anticipate this method has another promising application, functionalization of metal clusters by adding suitable agents to the polymer film.

5.2 Experimental section

5.2.1 Metal cluster deposition and preparation of colloidal suspensions

The MACS used for these experiments is shown schematically in **Figure 5.1** (c). Detailed information can be found in section 2.1.2. It comprises two vacuum chambers that are maintained at a base pressure in the mid 10^{-8} mbar range. In the first chamber the matrix is prepared on an oxygen-free Cu support mounted on a cold finger that is cooled to below 20 K by a continuous flow of liquid He. The matrix is produced by depositing metal atoms onto the matrix support from a thermal effusion cell while simultaneously introducing argon gas into the chamber. Once the matrix is generated, it is then moved to the second chamber and sputtered by an ion source (energy: 1.5 keV, current: ~30 μA), where a sample carousel is designed to hold up to 21 (2.5 cm × 7.5 cm, each) glass slides. The glass slides are coated with a polymer film by spin-coating a drop (0.3 ml) of 3.5 μM polymer solution on each slide at 4000 rpm for 10 s. The thickness of the resulting polymer film was determined by profilometer to be between 10 nm and 50 nm and it can be tuned by the concentration of the polymer solution and the spin speed. Cluster deposition times are typically selected to result in a cluster coverage of between 10 % and 20 % on each polymer film to avoid the cluster aggregation on the surface. The process of building the matrix and subsequently coating all the slides with clusters takes approximately 8 h. After cluster deposition, the glass slides are immersed in deionised water for 5 min to dissolve the polymer film and release the clusters into the suspension. When all 21 polymer films have been dissolved in 10 ml of water, this results in a colloidal suspension with a metal concentration of the order of 10 μg/ml. The process is outlined schematically in **Figure 5.2**.

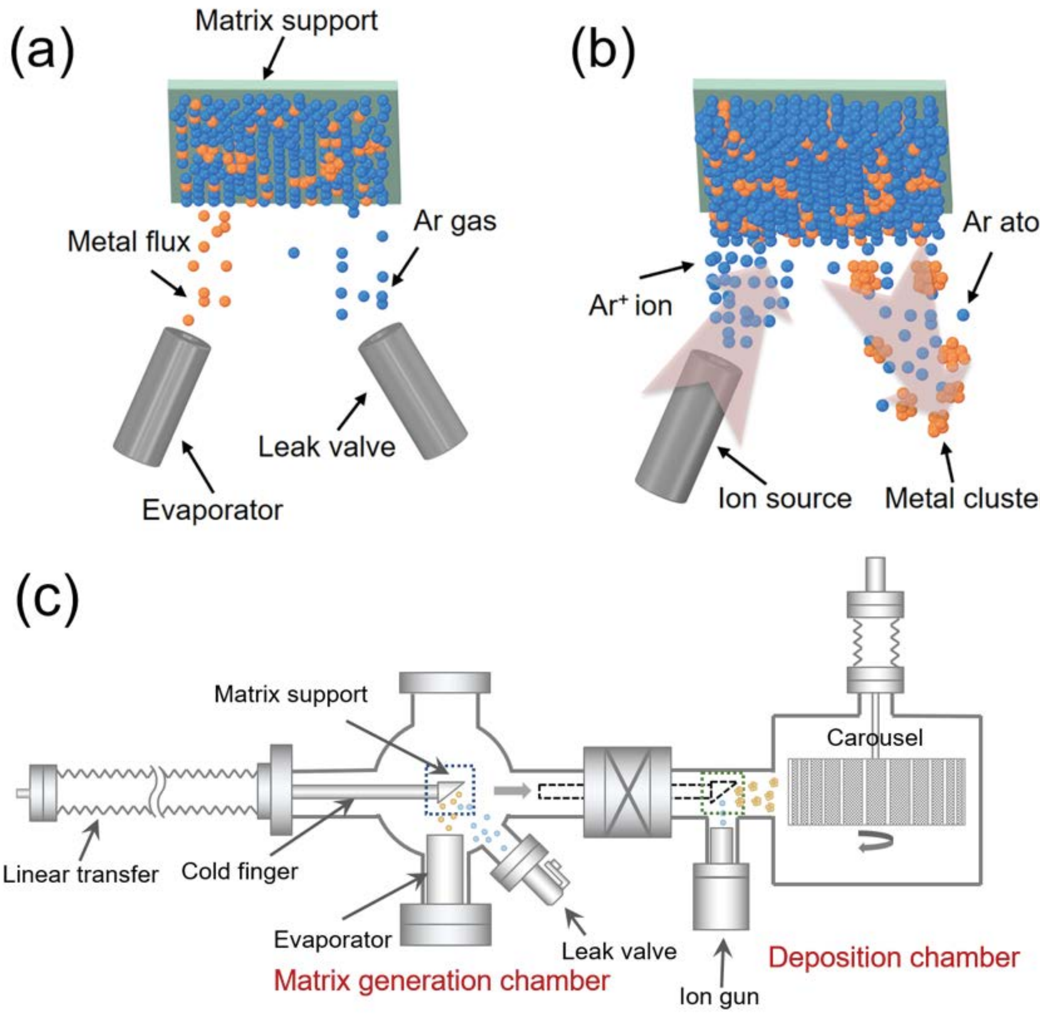

Figures 5.1 (a, b) Principle of operation of the matrix assembly cluster source with (a) formation of matrix by co-condensation of metal and Ar gas onto a cryogenically cooled surface, and (b) production of clusters by sputtering of the matrix with Ar ions. (c) Schematic diagram of the MACS system consisting of two sections: matrix generation chamber and deposition chamber. In the matrix generation chamber, a matrix support is mounted on a cold finger, which is cooled by a steady flow of liquid helium. A thermal evaporator is mounted on the bottom of the chamber to provide metal vapour and Ar gas is introduced through a leak valve. After building the matrix, the cold finger is moved to the deposition chamber for sputtering. The produced clusters can be collected by a sample carousel which can hold up to 21 glass slides.

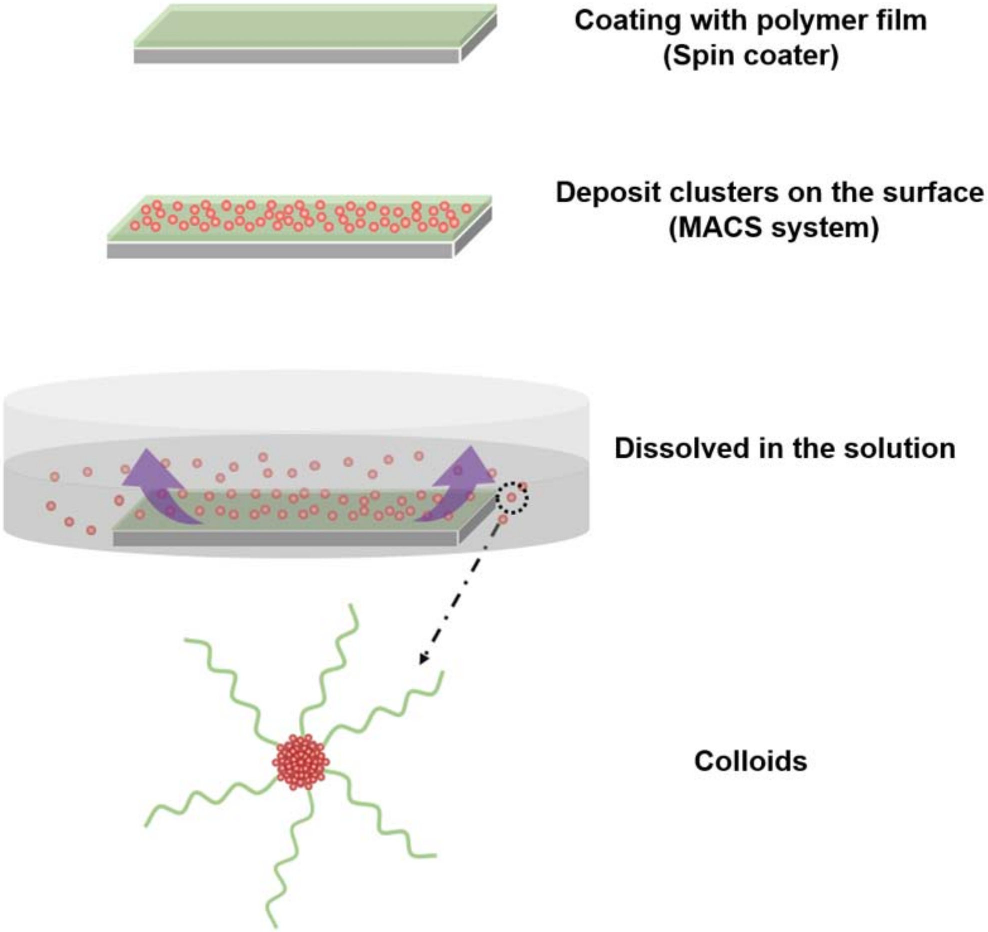

Figure 5.2 Schematic diagram of the preparation method to prepare colloids from MACS-deposited clusters. The glass slides are first coated with a soluble polymer film by spin-coating. After drying in air, the glass slides are loaded into the MACS and metal clusters are deposited on their surfaces. Then the cluster decorated glass slides are dissolved in the solution one by one to release clusters. The dissolved clusters encapsulated by polymers form the colloidal suspension.

5.2.2 Characterization of the as-deposited clusters and the cluster colloids

STEM images of the as-deposited clusters were obtained by depositing clusters directly onto Cu TEM grids coated with an amorphous carbon film. Samples of the metal colloids were prepared for STEM by casting a 20 μl drop of solution onto a TEM grid. The size distribution of colloids and as-deposited clusters were characterized by a JEOL JEM-2100F STEM equipped with a C_s corrector (CEOS) at a convergence angle of 20 mrad and an HAADF detector operating with an inner angle of 62 mrad and an outer angle of 164 mrad at 200 keV.

5.2.3 Preparation of Pd colloid catalyst

After obtaining the colloidal suspension, the total mass of the metal colloids in the solution can be calculated based on the cluster density and cluster diameter of the as-deposited clusters on the TEM grid. The calculation method was introduced in Chapter 2. In this experiment, 27 μg Pd cluster colloids were released in ~ 10 ml IPA solution, which was then added to 54 mg TiO_2 powder support (P25, Alfa Aesar) giving a mass metal loading of 0.05wt%. The wet mixture was dried at 100 ^oC for three hours.

5.2.4 Nitrophenol reduction measurement

The reduction of 4-nitrophenol catalysed by Pd colloid catalyst was carried out in aqueous solution at room temperature with $NaBH_4$ acting as the reductant. The reaction solution was prepared following the method described in section 2.4.1. In this experiment, 47 mg catalyst was added to 50 ml of the prepared solutions and continuously magnetically stirred. The reaction progress was monitored by recording the optical absorbance of the reaction solution at different reaction times using a UV-VIS spectrophotometer (Agilent Technologies Cary Series). The absorbance peak at 400 nm corresponds to 4-nitrophenol and the peak intensity is proportional to its concentration.[19-21] For each measurement, 2 ml of the analyte solution was filtered by a syringe filter (pore size: 0.2 μm) to remove the catalyst and poured into a cuvette for tests.

5.3 Results and discussions

5.3.1 Size evolution of different metal clusters (Au and Ag) before and after dissolving in IPA solution

In order to demonstrate this method, both Au and Ag colloids were prepared using polyvinylpyrrolidone (PVP) dissolved in isopropanol (IPA). PVP was the first polymer tested due to its wide usage as a stabilizing agent in colloidal systems.[22-24] **Figure 5.3** compares the HAADF-STEM images and size distributions of the as-deposited Au and Ag clusters with their colloidal counterparts. The as-deposited Au and Ag clusters exhibited a mean size of 1.3 nm and 1.7 nm, respectively. The deposited cluster coverage is low enough (~ 10%) to ensure that the clusters are not aggregated prior to encapsulation by the polymer. Some single atoms can also be observed, which may result from electron irradiation by the microscope. After dissolving the cluster-coated polymer films in IPA, isolated Au and Ag clusters are still observed in the drop-cast colloid samples shown in **Figures 5.3** (b) and (d), confirming that they do not aggregate while in the polymer solution. This supports the notion that the polymer molecules encapsulate the clusters and keep them apart in the suspension. In the case of the colloidal Au clusters, the cluster diameter remains 1.3 nm. It can be seen in **Figure 5.3** (b) that the clusters have accumulated in only part of the imaged area due to a drying effect that suspended particles prefer accumulating during evaporation.[25-27] In the case of the Ag clusters, the cluster size decreases slightly from 1.7±0.4 nm to 1.4±0.3 nm after dispersal into the colloidal suspension. One possible explanation for this is that PVP has a strong interaction with Ag atoms through multiple coordination of the >N-C=O groups[28] and the O will bind with the metal atoms[29] and etch the Ag clusters to reduce their size. It has been reported that small Ag clusters can be synthesized via etching of large metal nanoparticles by adding excess ligands.[30]

To further investigate the effect of the colloid preparation process on cluster size and structure, size-selected clusters were also prepared using a magnetron sputtering gas condensation cluster source equipped with a time-of-flight mass filter.[31] Size-selected $Au_{(923 \pm 20)}$ clusters were deposited onto a PVP film and then dissolved in IPA to produce colloids. Au_{923} clusters were chosen because their relatively large size (3.4 nm in diameter) makes it easier to resolve their microstructure in the STEM. **Figure 5.3** (i) shows the size distribution of the as-deposited Au_{923} clusters. It can be seen that the as-deposited clusters have a narrow size distribution with an average size of 3.4 nm. And after dissolving in IPA, the peak size of the clusters does not change, but the peak becomes slightly broader (see **Figure 5.3** (j)), which may be due to the influence of the dried polymer solution on the background intensity during analysis of the STEM images. From the magnified HAADF images, some crystalline structures are observed both from the as-deposited clusters and their colloidal counterparts, which indicates that the colloid preparation process does not significantly affect the structure of the clusters.

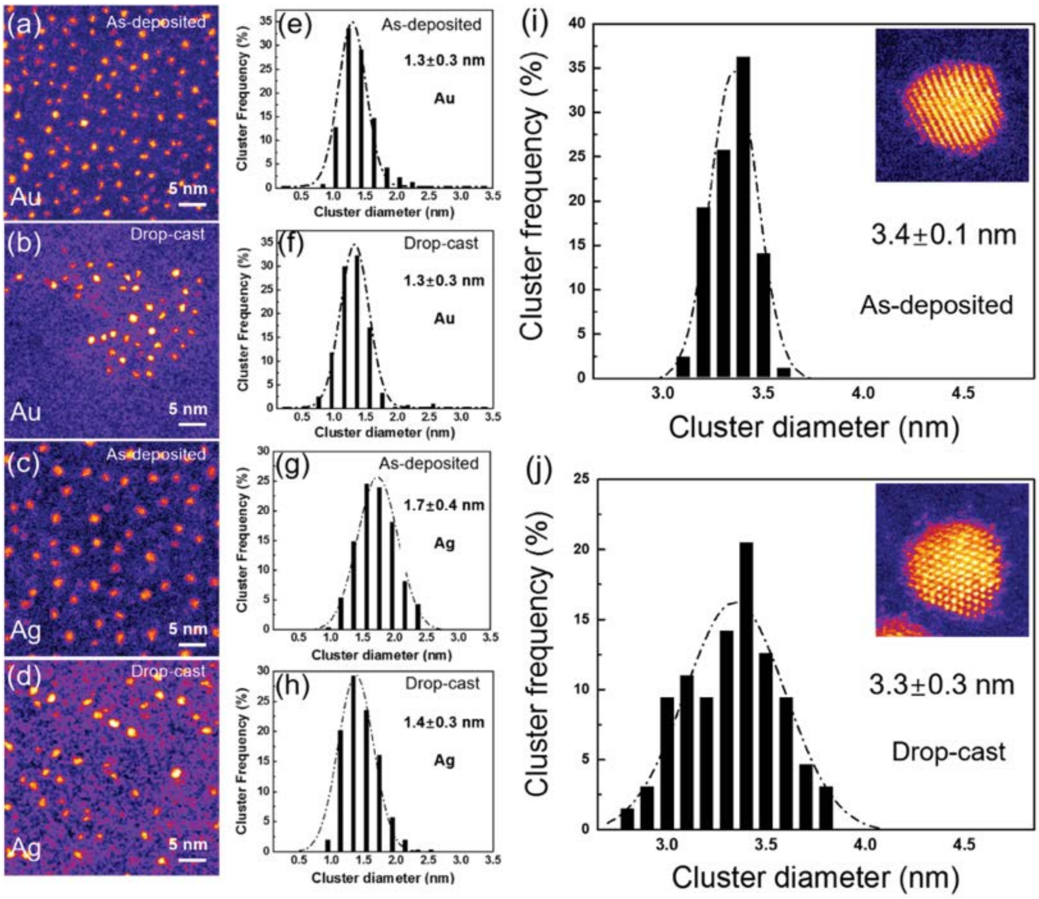

Figure 5.3 PVP-stabilised Au and Ag colloidal clusters prepared by MACS deposition onto PVP films followed by dissolution of the cluster/polymer layer in isopropanol. STEM images and size distributions of as-deposited Au clusters (a) and (e), drop-cast Au colloidal clusters (b) and (f), as-deposited Ag clusters (c) and (g), and drop-cast Ag colloidal clusters (d) and (h). Panels (i) and (j) show size distributions of size-selected Au_{923} and its corresponding colloid produced with a mass-filtered magnetron sputtering gas condensation cluster source. The insets show the typical STEM images of the as-deposited and colloidal Au_{923} in the mean peak of the size distribution. (The clusters used to obtain the diameter distribution are more than 500 for the as-deposited clusters and around 250 for the cluster colloids.)

5.3.2 The influence of the different polymer protecting layers to the size of the dissolved Au colloids in DI water

In addition to PVP, both polyvinyl alcohol (PVA) and polyethylene glycol (PEG) have also been tested as the stabilizing agent. **Figure 5.4** shows the typical STEM images and size distribution histograms of the as-deposited Au clusters, and the resulting Au colloids using PVA and PEG. The as-deposited clusters were deposited with an average size of 0.9 nm. No aggregation has been observed. After dissolving the cluster-coated polymer films in de-ionized water (PEG and PVA are difficult to dissolve in IPA), STEM measurements of the resulting colloidal clusters confirm that both polymers work well as stabilizing agents. It should be noted that in both cases drying effects resulted in the accumulation of clusters in certain areas of the carbon film on the TEM grid. The cluster size measured for both colloidal suspensions is larger, being 1.2 nm for Au/PVA colloids and 1.4 nm for Au/PEG colloids. This indicates that some limited aggregation occurs during the dissolving process. This could be due to the weaker binding of PVA and PEG to the metal clusters via their OH group compared to the stronger binding of PVP via it's >N-C=O group. Moreover, as the PVA and PEG dissolve slowly in water, it is possible that some aggregation of clusters can occur during the early stages of dissolution of the polymer film. However, once the polymer films have been fully dissolved, the clusters are stable against further aggregation.

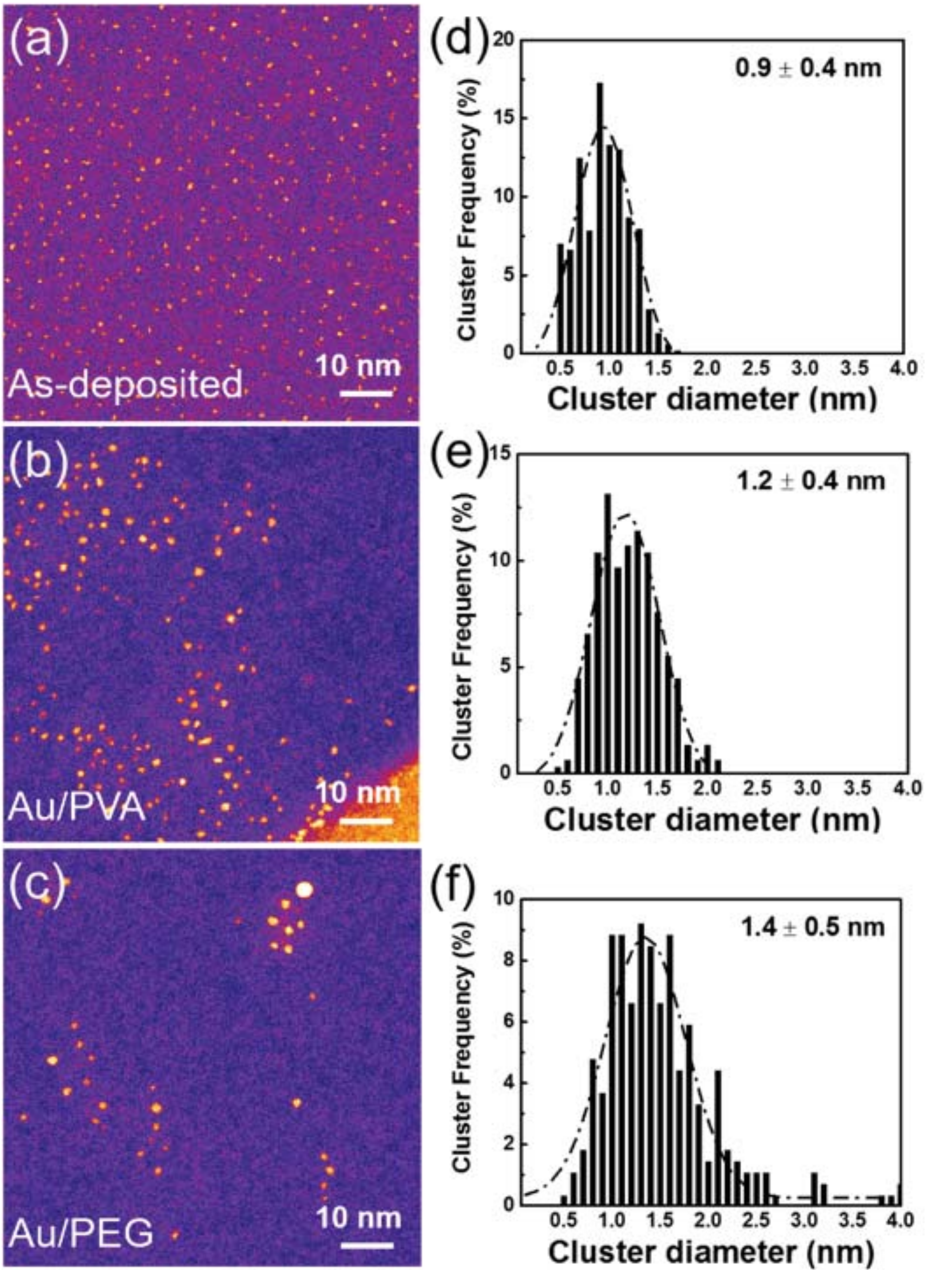

Figure 5.4 Au colloids prepared with different polymer protecting layers dissolved in DI water. STEM images and size distribution histograms of the as-deposited Au clusters, (a) and (d); colloidal Au clusters in PVA solution, (b) and (e); and colloidal Au in PEG solution, (c) and (f).

5.3.3 Catalytic properties of the Pd colloid catalyst for the nitrophenol reduction by $NaBH_4$

Following the methodology study, the catalytic properties of the colloid catalyst produced by this method was also investigated through catalyzing the liquid phase reaction, 4-nitrophenol reduction. Pd cluster was chosen as the study object since it has been reported catalytic active for this reaction.[20, 32] **Figure 5.5** (a) shows the diameter distribution histogram of the as-deposited Pd clusters on the TEM grid. The inset is a typical HAADF image used to obtain the diameter distribution. It can be seen that dense Pd clusters are deposited on the TEM grid with an average diameter of ~1.06 nm. To prepare Pd colloids, the Pd clusters were also deposited onto PVP coated glass slides, which were then dissolved in IPA solution. Considering the cluster number and total surface area, a large excess of PVP molecules exists in the colloidal suspensions. So, it could be imagined that the surface of the TiO_2 supports was covered by PVP molecules after drying in the air. To investigate the catalytic activity of the produced Pd colloid catalyst, the optical absorbance spectra of the reaction solution were recorded at different times after adding the powder catalysts in the reaction solution, as shown in **Figure 5.5** (b). It can be seen that the peak intensity at 400 nm, corresponding to the nitrophenol, does not change prominently. However, after zooming in on the spectra in the range of 390 – 410 nm, a slow, sequent decrease of the peak intensity with the reaction time is observed, which suggests the Pd colloid catalyst is slightly active for the nitrophenol reduction. To show the activity more clearly, the plot of the absorbance at 400 nm *versus* the reaction time is presented in **Figure 5.5** (c). Obviously, the absorbance at 400 nm decreases with the reaction time. Considering this reaction following a pseudo-first order kinetics in the presence of a large excess of $NaBH_4$, the relationship between absorbance and reaction time is fitted by an exponential function with the R square of 0.993, which further confirms that Pd colloid catalyst is slightly active for this reaction.

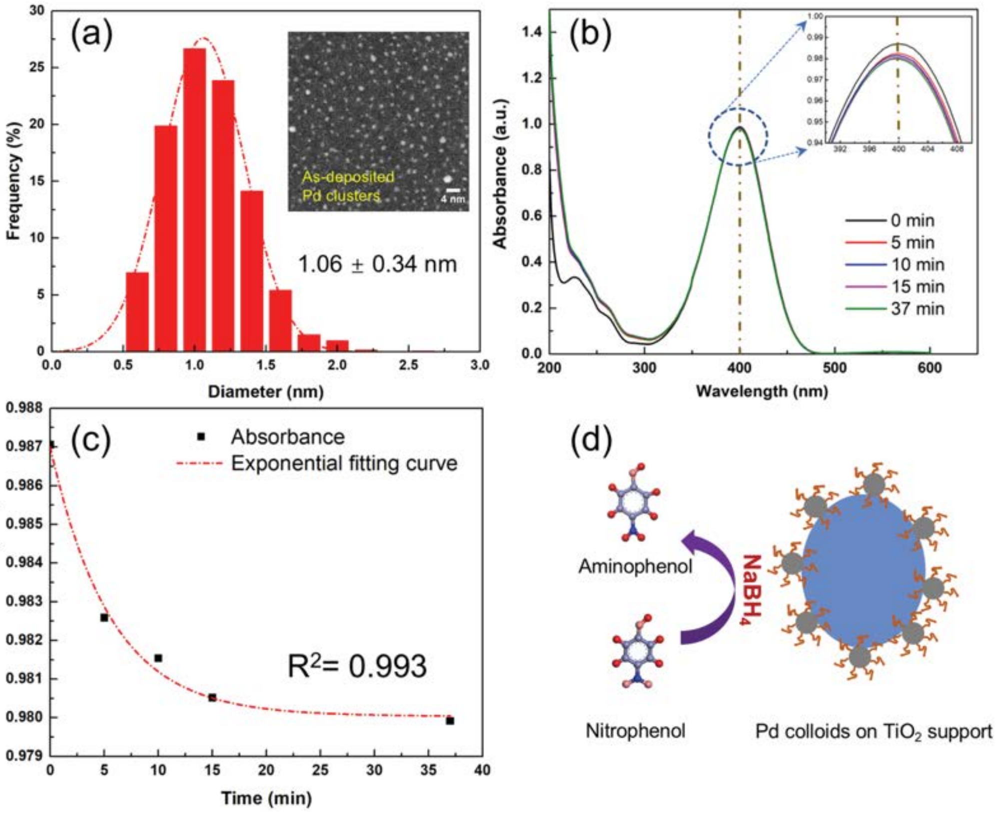

Figure 5.5 (a) Cluster diameter distribution histogram of as-deposited Pd clusters on the TEM grid. The inset is a typical HAADF image used to obtain the cluster diameter. (b) UV-VIS absorbance spectra at different reaction times for the 4-nitrophenol reduction catalyzed by Pd colloidal catalyst. The inset shows the magnified absorbance spectra in the range of 390 – 410 nm. The absorbance peak at 400 nm wavelength represents 4-nitrophenol. (c) Plot of the absorbance at 400 nm wavelength *versus* reaction time. The red dashed curve is the exponential fitting curve. $R^2 = 0.993$. (d) Schematic diagram of the nitrophenol reduction catalyzed by Pd colloid based catalyst.

It is believed that the low activity can be explained by two reasons. One is the low metal loading (~0.05wt%) compared with the industrial catalysts (usually 1wt% - 5wt%), which leads to insufficient metal particles participating in the reaction. The second reason may be related to the protecting polymers. After drying the catalyst powder, the Pd colloids are deposited on the surface of TiO_2 supports, schematically shown in **Figure 5.5** (d). The existence of the protecting polymers prevents cluster aggregation, but simultaneously too many protecting polymers can also block the active sites on the cluster surface. During the reaction, only limited nitrophenol molecules can access metal sites on the Pd clusters. So, the low metal loading and too many protecting polymers may account for this low catalytic activity.

5.3.4 Discussion of the new colloid preparation method for catalysis application

Based on the experimental results discussed above, we have demonstrated a new simple method to prepare colloids from physically deposited size-controlled clusters. However, this method is at an early stage. The catalysts made by this method are not yet as competitive as those made by traditional colloidal routes. Our catalysis study on TiO_2 supported Pd colloids for nitrophenol reduction has shown that too many polymers can block the active sites on the cluster surface, thus result in a weak activity. So, a further study of controlling the amount of the polymers used in this method and comparing the activities of the colloids with different protecting polymers and different thicknesses is still needed. By tuning the spin speed (for polymer coating) and concentration of the polymer solution, the thickness of the coated polymer layer is expected to be controlled. Also, evaporating polymer molecules to glass slides in a vacuum chamber is another way to decrease the usage of protecting polymers. It should be further noted that by using this method, the functionalization of metal clusters for medical and sensing applications, could be easily achieved by adding other suitable agents (ligands) to the polymer solution (for spin-coating). During the release process, the cluster will preferably bind with the molecules that have stronger interaction with clusters. Therefore, by choosing proper polymers and functional agents, the preformed clusters could be easily functionalized according to the application.

5.4 Conclusions

In summary, we have demonstrated the proof-of-principle study of a simple method for the preparation of colloids of physically deposited size-controlled clusters. The colloids are prepared by depositing pre-formed clusters from a cluster beam source onto soluble polymer films, followed by dissolution of the cluster-coated polymer films in a solvent. This has been demonstrated using different cluster materials (Au and Ag), polymers (PVP, PVA and PEG) and solvents (IPA and water). In all cases, STEM measurements of the colloidal clusters revealed limited aggregation, confirming that the polymer molecules encapsulate the clusters and stabilize them against aggregation in suspension. It is also indicated that no microstructure changes occur inside the clusters during the colloid formation process. We propose that this method can be applied to prepare biocompatible colloids of ultraprecise clusters using cluster beam technology. In addition, the catalytic activity of the colloid catalyst produced by this method is also investigated by catalyzing nitrophenol reduction over Pd colloids supported on TiO_2 powders. It is found that the Pd colloids on TiO_2 support exhibit a small activity for the reaction which may derive from the low metal loading and too many protecting polymers that can block the active sites on the cluster surface. Furthermore, we also anticipate that it will be possible to functionalize the clusters by the addition of suitable agents to the polymer films.

References

(1) Jain, P. K.; Huang, X.; El-Sayed, I. H.; El-Sayed, M. A. Noble Metals on the Nanoscale: Optical and Photothermal Properties and Some Applications in Imaging, Sensing, Biology, and Medicine. *Acc. Chem. Res.* **2008,** *41*, 1578.

(2) Daniel, M.-C.; Astruc, D. Dold Nanoparticles: Assembly, Supramolecular Chemistry, Quantum-Size-Related Properties, and Applications toward Biology, Catalysis, and Nanotechnology. *Chem. Rev.* **2004,** *104*, 293.

(3) Toshima, N.; Shiraishi, Y.; Teranishi, T.; Miyake, M.; Tominaga, T.; Watanabe, H.; Brijoux, W.; Bönnemann, H.; Schmid, G. Various ligand-stabilized metal nanoclusters as homogeneous and heterogeneous catalysts in the liquid phase. *Appl. Organomet. Chem.* **2001,** *15*, 178.

(4) Tsunoyama, H.; Sakurai, H.; Negishi, Y.; Tsukuda, T. Size-Specific Catalytic Activity of Polymer-Stabilized Gold Nanoclusters for Aerobic Alcohol Oxidation in Water. *J. Am. Chem. Soc.* **2005,** *127*, 9374.

(5) Chen, X.; Schluesener, H. J. Nanosilver: a nanoproduct in medical application. *Toxicol. Lett.* **2008,** *176* (1), 1.

(6) Narayanan, R.; El-Sayed, M. A. Shape-dependent catalytic activity of platinum nanoparticles in colloidal solution. *Nano Lett.* **2004,** *4*, 1343.

(7) Fenger, R.; Fertitta, E.; Kirmse, H.; Thunemann, A. F.; Rademann, K. Size dependent catalysis with CTAB-stabilized gold nanoparticles. *Phys. Chem. Chem. Phys.* **2012,** *14* (26), 9343.

(8) Narayanan, R.; El-Sayed, M. A. Effect of colloidal catalysis on the nanoparticle size distribution: dendrimer-Pd vs PVP-Pd nanoparticles catalyzing the Suzuki coupling reaction. *J.*

Phys. Chem. B **2004,** *108*, 8572.

(9) P. R. Ellis; C. M. Brown; P. T. Bishop; J. Yin; K. Cooke; W. D. Terry; J. Liu; F. Yin; Palmer, R. E. The cluster beam route to model catalysts and beyond. *Faraday Discuss.* **2016,** *188*, 39.

(10) Palmer, R. E.; Pratontep, S.; Boyen, H.-G. Nanostructured surfaces from size-selected clusters. *Nat. Mater.* **2003,** *2*, 443.

(11) Engemann, D. C.; Roese, S.; Hövel, H. Preformed 2 nm Ag clusters deposited into ionic liquids: stabilization by cation–cluster interaction. *J. Phys. Chem. C* **2016,** *120* (11), 6239.

(12) Rogov, A. V.; Fanchenko, S. S.; Belova, N. E. Generation of metal-nanoparticle colloidal solution by means of magnetron deposition on a liquid surface. *Nanotechnol. Russ.* **2010,** *4* (11-12), 802.

(13) Wagener, M.; Günther, B. High pressure DC-magnetron sputtering on liquids: A new process for the production of metal nanosuspensions. *Progr. Colloid Ploym. Sci.* **1998,** *111*, 78.

(14) Wender, H.; de Oliveira, L. F.; Feil, A. F.; Lissner, E.; Migowski, P.; Meneghetti, M. R.; Teixeira, S. R.; Dupont, J. Synthesis of gold nanoparticles in a biocompatible fluid from sputtering deposition onto castor oil. *Chem Commun (Camb)* **2010,** *46* (37), 7019.

(15) E. C. Tyo; Vajda, S. Catalysis by clusters with precise numbers of atoms. *Nat. Nanotechnol.* **2015,** *10* (7), 577.

(16) Palmer, R. E.; Cao, L.; Yin, F. Note: Proof of principle of a new type of cluster beam source with potential for scale-up. *Rev. Sci. Instrum.* **2016,** *87* (4), 046103.

(17) Oiko, V. T.; Mathieu, T.; Cao, L.; Liu, J.; Palmer, R. E. Note: Production of silver nanoclusters using a Matrix-Assembly Cluster Source with a solid CO_2 matrix. *J. Chem. Phys.* **2016,** *145* (16), 166101.

(18) Pozun, Z. D.; Rodenbusch, S. E.; Keller, E.; Tran, K.; Tang, W.; Stevenson, K. J.; Henkelman, G. A systematic investigation of p -nitrophenol reduction by bimetallic dendrimer encapsulated nanoparticles. *J. Phys. Chem. C* **2013,** *117*, 7598.

(19) Lin, F.; Doong, R. Bifunctional Au−Fe_3O_4 heterostructures for magnetically recyclable catalysis of nitrophenol reduction. *J. Phys. Chem. C* **2011,** *115* (14), 6591.

(20) Harish, S.; Mathiyarasu, J.; Phani, K. L. N.; Yegnaraman, V. Synthesis of conducting polymer supported Pd nanoparticles in aqueous medium and catalytic activity towards 4-nitrophenol reduction. *Catal. Lett.* **2008,** *128* (1-2), 197.

(21) Cai, R.; Ellis, P. R.; Yin, J.; Liu, J.; Brown, C. M.; Griffin, R.; Chang, G.; Yang, D.; Ren, J.; Cooke, K.; Bishop, P. T.; Theis, W.; Palmer, R. E. Performance of preformed Au/Cu nanoclusters deposited on MgO powders in the catalytic reduction of 4-nitrophenol in solution. *Small* **2018,** *14*, 1703734.

(22) Santiago Gonzalez, B.; Rodriguez, M. J.; Blanco, C.; Rivas, J.; Lopez-Quintela, M. A.; Gaspar Martinho, J. M. One step synthesis of the smallest photoluminescent and paramagnetic PVP-protected gold atomic clusters. *Nano Lett.* **2010,** *10* (10), 4217.

(23) Zhang, H.; Kawashima, K.; Okumura, M.; Toshima, N. Colloidal Au single-atom catalysts embedded on Pd nanoclusters. *J. Mater. Chem. A* **2014,** *2* (33), 13498.

(24) Koczkur, K. M.; Mourdikoudis, S.; Polavarapu, L.; Skrabalak, S. E. Polyvinylpyrrolidone (PVP) in nanoparticle synthesis. *Dalton Trans.* **2015,** *44* (41), 17883.

(25) Yunker, P. J.; Still, T.; Lohr, M. A.; Yodh, A. G. Suppression of the coffee-ring effect by shape-dependent capillary interactions. *Nature* **2011,** *476* (7360), 308.

(26) Anyfantakis, M.; Geng, Z.; Morel, M.; Rudiuk, S.; Baigl, D. Modulation of the coffee-ring

effect in particle/surfactant mixtures: the importance of particle-interface interactions. *Langmuir* **2015,** *31* (14), 4113.

(27) Das, S.; Dey, A.; Reddy, G.; Sarma, D. D. Suppression of the coffee-ring effect and evaporation-driven disorder to order transition in colloidal droplets. *J. Phys. Chem. Lett.* **2017,** *8* (19), 4704.

(28) Tsunoyama, H.; Sakurai, H.; Ichikuni, N.; Negishi, Y.; Tsukuda, T. Colloidal gold nanoparticles as catalyst for carbon-carbon bond formation: Application to aerobic homocoupling of phenylboronic acid in water. *Langmuir* **2004,** *20*, 11293.

(29) Zhang, H.; Toshima, N.; Takasaki, K.; Okumura, M. Preparation of Ag core /Au shell bimetallic nanoparticles from physical mixtures of Au clusters and Ag ions under dark conditions and their catalytic activity for aerobic glucose oxidation. *J. Alloys Compd.* **2014,** *586*, 462.

(30) Yuan, X.; Luo, Z.; Zhang, Q.; Zhang, X.; Zheng, Y.; Lee, J. Y.; Xie, J. Synthesis of highly fluorescent metal (Ag, Au, Pt, and Cu) nanoclusters by electrostatically induced reversible phase transfer. *ACS Nano* **2011,** *5*, 8800.

(31) Pratontep, S.; Carroll, S. J.; Xirouchaki, C.; Streun, M.; Palmer, R. E. Size-selected cluster beam source based on radio frequency magnetron plasma sputtering and gas condensation. *Rev. Sci. Instrum.* **2005,** *76* (4), 045103.

(32) Li, H.; Han, L.; Cooper-White, J.; Kim, I. Palladium nanoparticles decorated carbon nanotubes: facile synthesis and their applications as highly efficient catalysts for the reduction of 4-nitrophenol. *Green Chem.* **2012,** *14* (3), 586.

CHAPTER 6

Conclusions

In this thesis, the catalytic properties of cluster catalysts produced by two types of cluster beam source were demonstrated in liquid-phase and vapour-phase model catalytic reactions. Aberration-corrected STEM coupled with the EDS technique was employed to investigate the effects of the cluster chemical composition, atomic structure and size evolution during the reactions on the cluster activities.

First, physically produced Au/Cu alloy clusters (from a dual-magnetron sputtering gas condensation cluster source) deposited on MgO powder supports were found to be active for the liquid-phase 4-nitrophenol reduction. Clusters with similar amount of Au and Cu were much more active than the Au-rich and Cu-rich clusters. Given the random distribution of Au and Cu atoms, more Au/Cu two atom sites are believed to exist on the cluster surface for the Au/Cu-equal clusters. Therefore, the interplay between Au and Cu atoms was deduced to account for the enhanced activity, which was confirmed by model DFT calculations of the cluster-adsorbate system. In addition, it was also found that the physically deposited Au/Cu cluster catalysts were much more active than the chemically synthesized Au/Cu reference samples. This was attributed to the superior size and composition control of the cluster beam technique.

Second, vapour-phase 1-pentyne selective hydrogenation was conducted on Pd clusters that were deposited by MACS onto diced carbon tapes. The activity was compared with a Pd reference sample made by traditional wet impregnation. It was found that the Pd cluster catalyst made from MACS was more active in terms of per unit weight than the Pd reference sample and exhibited a competitive high selectivity (~95%) to 1-pentene. The superior activity was associated with the smaller cluster size, which could provide more surface active sites for the reaction. In addition, it was also found that adding Au atoms into the Pd clusters did not increase cluster activity and selectivity. This can be attributed to the surface oxidation in air, which can drive the Pd atoms to the cluster surface, thus leading to a similar Pd surface as pure Pd clusters.

Finally, a new method to prepare metal colloids from physically deposited clusters was demonstrated, thus extending the potential application of the cluster beam deposition technique to life science etc. The principle of this method is to deposit clusters directly onto soluble polymer films followed by releasing the clusters into suitable solvents, which was demonstrated by generating colloids of different cluster materials (Au and Ag) and different polymers (PVP, PVA and PEG). In addition, the 4-nitrophenol reduction was conducted on a Pd colloid sample made by this method to explore its catalytic performance. However, it was found that the Pd colloids only exhibited a small activity for the reaction, which is attributed to the protecting polymers blocking the active sites. Since this method is at an early stage, a further study controlling the amount of the polymer used in this method, and comparing the activities of the colloids with different protecting polymers, is still needed.

APL MATERIALS 5, 053405 (2017)

A new method to prepare colloids of size-controlled clusters from a matrix assembly cluster source

Rongsheng Cai, Nan Jian, Shane Murphy, Karl Bauer,
and Richard E. Palmer[a]
Nanoscale Physics Research Laboratory, School of Physics and Astronomy,
University of Birmingham, Birmingham B15 2TT, United Kingdom

(Received 14 December 2016; accepted 26 January 2017; published online 1 March 2017)

A new method for the production of colloidal suspensions of physically deposited clusters is demonstrated. A cluster source has been used to deposit size-controlled clusters onto water-soluble polymer films, which are then dissolved to produce colloidal suspensions of clusters encapsulated with polymer molecules. This process has been demonstrated using different cluster materials (Au and Ag) and polymers (polyvinylpyrrolidone, polyvinyl alcohol, and polyethylene glycol). Scanning transmission electron microscopy of the clusters before and after colloidal dispersion confirms that the polymers act as stabilizing agents. We propose that this method is suitable for the production of biocompatible colloids of ultraprecise clusters. © *2017 Author(s). All article content, except where otherwise noted, is licensed under a Creative Commons Attribution (CC BY) license (http://creativecommons.org/licenses/by/4.0/).*
[http://dx.doi.org/10.1063/1.4977204]

There is a burgeoning requirement for colloids of ultraprecise nanoparticles, particularly for life science applications where precise control of nanoparticle size, shape, and composition is critical to delivering safe, consistent, and efficient nanoparticle-based diagnostics and treatments. Colloids are typically produced by batch chemical processes, where it can be difficult to precisely control size and dispersion. Variations between batches of the same product can arise due to small differences in the mixing or heating of the reagents. Moreover, developing new nanomaterials through chemical synthesis routes can be time-consuming and difficult. The physical production of nanoparticles using cluster beam technology offers the possibility to produce nanoparticles in an environmentally benign way (i.e., not involving hazardous chemicals or waste), with unparalleled control over nanoparticle size and allows new nanomaterials to be quickly developed.

In order to provide a storage and delivery solution suitable for life science applications, a means of transferring the cluster beam-deposited nanoparticles into biocompatible colloidal suspensions is required. In this paper, we present a proof-of-principle study of the preparation of colloidal suspensions of cluster beam-deposited size-controlled clusters. This is realised by depositing clusters onto a water-soluble polymer film that is subsequently dissolved to produce a colloidal suspension where the polymer molecules encapsulate the clusters and stabilize them against aggregation. The key feature of this approach is that pre-formed clusters are deposited onto the polymer in solid form before dissolution to produce a liquid. There have been previous attempts to prepare colloids of physically deposited clusters, e.g., by direct deposition into ionic liquids[1] or organic liquids such as castor oil.[2] However, in some of these cases the size control is limited due to the aggregation inside the liquid, while in others the resulting colloids are not biocompatible.

One factor limiting the use of cluster beam technology for colloid production is that it can be difficult to produce nanoparticles in useful quantities. This problem has recently been addressed with the development of the matrix assembly cluster source (MACS), which allows the production of large quantities of size-controlled clusters. The principle of the MACS is illustrated in Figs. 1(a) and 1(b), and has been described in detail elsewhere.[3–5] Briefly, a target matrix comprising metal

---

[a] Author to whom correspondence should be addressed. Electronic mail: r.e.palmer@bham.ac.uk

© Author(s) 2017

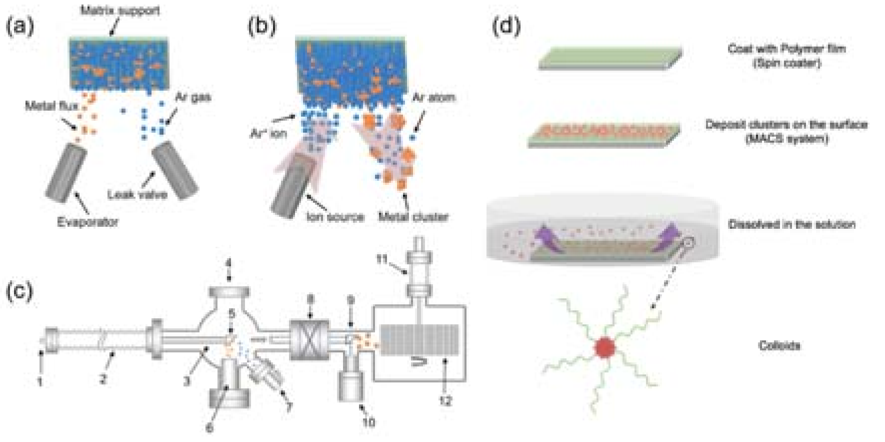

FIG. 1. ((a) and (b)) Principle of operation of the matrix assembly cluster source with (a) formation of matrix by co-condensation of metal and Ar gas onto a cryogenically cooled surface and (b) production of clusters by sputtering of the matrix with (1.5 keV) Ar ions. (c) Schematic diagram of the MACS system with (1) liquid He and electrical feedthrough for coldfinger, (2) linear translator for (3) coldfinger, (4) pumping port for the matrix chamber, (5) matrix support, (6) evaporator, (7) Ar leak valve, (8) gate valve, (9) position of the matrix during sputtering to produce nanoclusters, (10) ion source, (11) linear translator, and rotary drive for (12) the sample carousel. (d) Schematic diagram of the preparation method to prepare colloids from MACS-deposited clusters.

atoms embedded in a noble gas matrix is produced by physical vapour deposition of metal atoms onto a cryogenically cooled support while simultaneously co-condensing the noble gas. The matrix is subsequently sputtered with Ar ions to produce cascades of atomic collisions inside the matrix, causing clusters to nucleate and ripen before eventually being ejected from the matrix. The cluster size is controlled via the metal concentration inside the matrix, the matrix temperature, and the sputter parameters. Size-controlled clusters can be deposited without the need for a subsequent mass-filtering step, which would invariably lead to significant loss of material.

The MACS used for these experiments is shown schematically in Fig. 1(c). It comprises two vacuum chambers that are maintained at a base pressure in the mid 10^{-8} mbar range. In the first chamber the matrix is prepared on an oxygen-free Cu support mounted on a cold finger that is cooled to below 20 K by a continuous flow of liquid He. The matrix is produced by metal deposition onto the support from a thermal evaporator while simultaneously introducing argon gas into the chamber. Once the matrix is generated it is then sputtered by an ion source in the second chamber, which contains a sample carousel designed to hold up to 21 (2.5 cm × 7.5 cm) glass slides. The slides are coated with a polymer film by spin-coating a drop (0.3 ml) of 3.5 μM polymer solution on each slide at 4000 rpm for 10 s. The thickness of the resulting polymer film was determined by a profilometer to be typically between 10 nm and 50 nm. After cluster deposition the glass slides are immersed in deionised water for 5 min to dissolve the polymer film and release the clusters into the suspension. Cluster deposition times are typically selected to result in a cluster coverage between 10% and 20% on each polymer film. Dissolving all 21 polymer films in 10 ml of water results in a colloid with a metal concentration of ~10 μg/ml. The process is outlined schematically in Fig. 1(d).

Scanning transmission electron microscope (STEM) images of the as-deposited clusters were obtained by depositing clusters directly onto Cu TEM grids coated with an amorphous carbon film. Samples of the metal colloids were prepared for STEM by drop-casting a 20 μl drop of solution onto a TEM grid. The size distribution of colloids and as-deposited clusters was characterized by a JEOL JEM-2100F STEM equipped with a Cs corrector (CEOS) and a HAADF detector operating with an inner angle of 62 mrad and an outer angle of 164 mrad at 200 keV.

In order to demonstrate this method, both Au and Ag colloids have been prepared using polyvinylpyrrolidone (PVP, MW ~10 000, Sigma-Aldrich) dissolved in isopropanol (IPA, laboratory grade, Fisher Chemical). PVP was the first polymer tested due to its wide usage as a stabilizing agent in colloids.[6] Figure 2 compares the STEM images and size distributions of the as-deposited

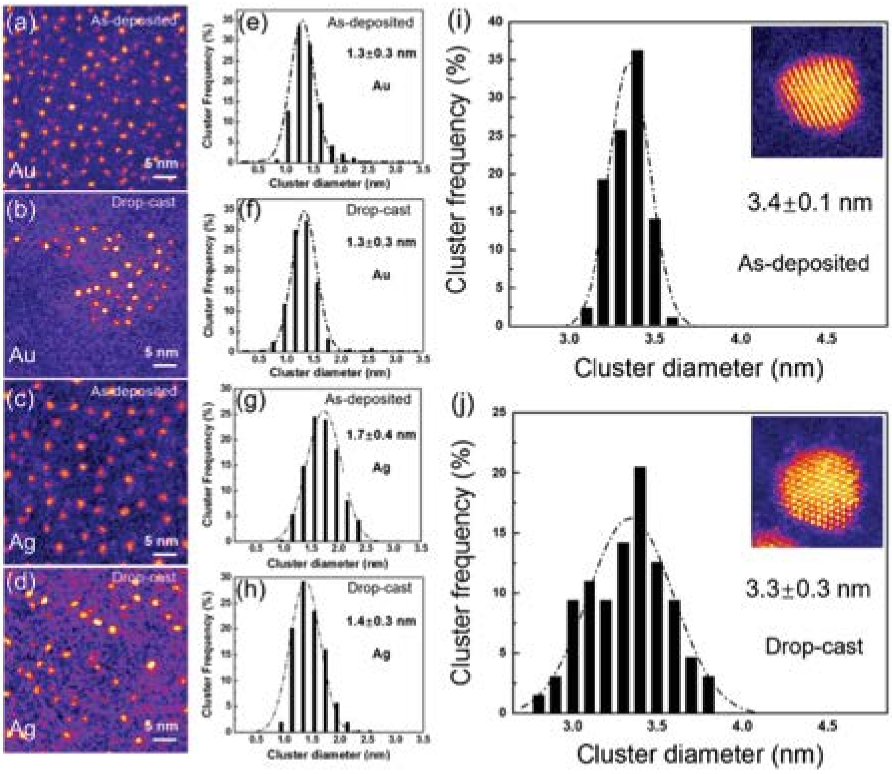

FIG. 2. PVP-stabilised Au and Ag colloidal clusters prepared by MACS deposition onto PVP films followed by dissolution of the cluster/polymer layer in isopropanol. STEM images and size distributions of as-deposited Au clusters ((a) and (e)), drop-cast Au colloidal clusters ((b) and (f)), as-deposited Ag clusters ((c) and (g)), and drop-cast Ag colloidal clusters ((d) and (h)). Panels (i) and (j) show size distributions of size-selected Au_{923} and its corresponding colloid produced with a mass-filtered magnetron sputtering gas condensation cluster source. The insets show the typical STEM images of the as-deposited and colloidal Au_{923} in the mean peak of the size distribution.

Au and Ag clusters with their colloidal counterparts. The as-deposited Au and Ag clusters have been deposited with a mean size of 1.3 nm (equivalent to ∼70 Au atoms) and 1.7 nm (equivalent to ∼150 Ag atoms), respectively. The deposited cluster coverage is low enough to ensure that the clusters are not aggregated prior to encapsulation by the polymer. After dissolving the cluster-coated polymer films in IPA, isolated Au and Ag clusters are still observed in the drop-cast colloid samples shown in Figs. 2(b) and 2(d), confirming that they do not aggregate while inside the polymer solution. This supports the notion that the polymer molecules encapsulate the clusters and keep them apart in the suspension. In the case of the colloidal Au clusters, the cluster diameter remains as 1.3 nm. It can be seen in Fig. 2(b) that the clusters have accumulated in only a part of the area imaged due to drying effect. In the case of the Ag clusters, the cluster size decreases slightly from 1.7 ± 0.4 nm to 1.4 ± 0.3 nm after dispersal into the colloidal suspension. A possible explanation for this is that PVP has a strong interaction with Ag atoms through multiple coordination of the >N-C=O groups[7] and that the O will bind with the metal atoms[8] and etch the Ag clusters to reduce their size. It has been reported that small Ag clusters can be synthesized via etching of large metal nanoparticles by adding excess ligands.[9]

To further investigate the effect of the colloid preparation process on cluster size and microstructure, size-selected clusters were also prepared using a magnetron sputtering gas condensation cluster source equipped with a time-of-flight mass filter.[10] Size-selected Au_{923} clusters[11] were deposited onto a PVP film and then dissolved in IPA. Au_{923} are relatively large in size (3.4 nm) making it easier to resolve their microstructure in the STEM. Figure 2(i) shows the size distribution of the as-deposited Au_{923} clusters. The as-deposited clusters have a narrow size distribution with an average size of

3.4 nm. After dissolving in IPA, the peak size of the clusters does not change, but the distribution becomes broader, which may be due to the influence of the dried polymer solution on the background intensity during analysis of the STEM images. No change in microstructure is observed when comparing the as-deposited clusters with their colloidal counterparts, confirming that the colloid preparation process does not affect the microstructure of the clusters.

In addition to PVP, both polyvinyl alcohol (PVA, MW 9000-10000, Sigma-Aldrich) and polyethylene glycol (PEG, MW ~1500, Sigma-Aldrich) have been tested as stabilizing agents. Figure 3 shows the typical STEM images and size distribution histograms of the as-deposited Au clusters, and the resulting Au colloids using PVA and PEG. The as-deposited clusters were deposited with an average size of 0.9 nm, which is equivalent to ~25 Au atoms. After dissolving the cluster-coated polymer films in de-ionized water the cluster size measured in both cases is larger, being 1.2 nm for Au/PVA clusters and 1.4 nm for Au/PEG clusters. This indicates that some limited aggregation occurs during the dissolving process. This might either be due to the weaker binding of PVA and PEG to the metal clusters compared to PVP, or, as PVA and PEG dissolve slowly in water, some cluster aggregation

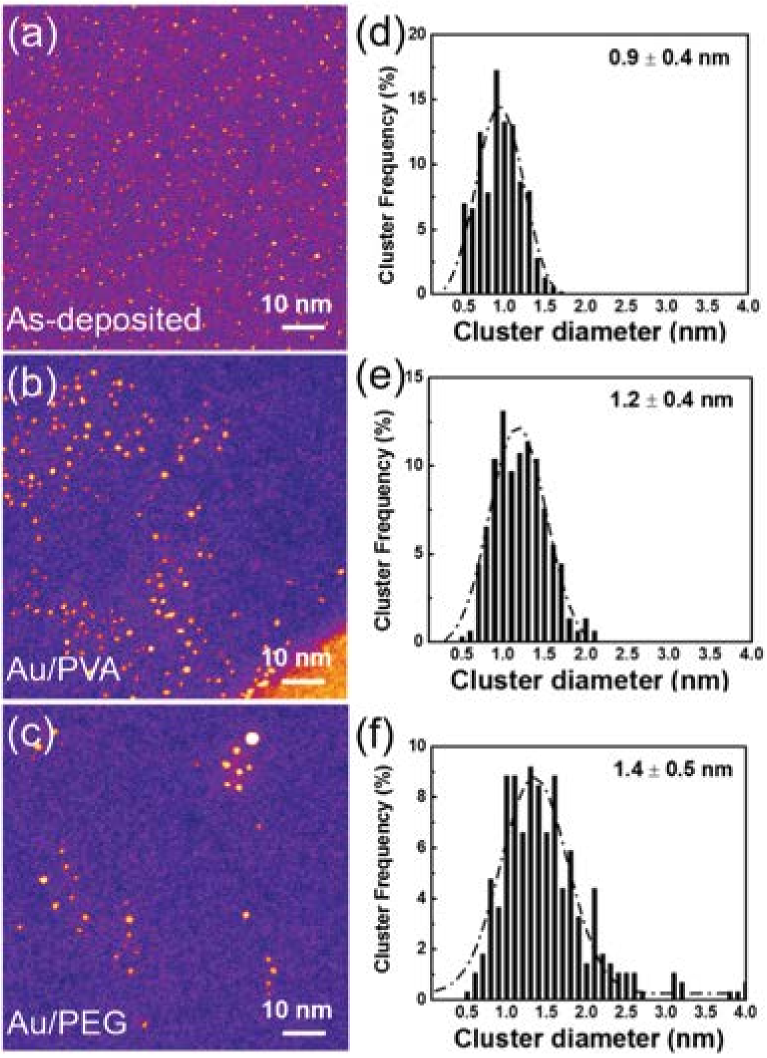

FIG. 3. Au colloids prepared with different polymer protecting layers dissolved in water. STEM images and size distribution histograms of the as-deposited Au clusters, ((a) and (d)), colloidal Au clusters in PVA solution, ((b) and (e)), and colloidal Au in PEG solution, ((c) and (f)).

might occur before the clusters are completely encapsulated. However, once the polymer films have been fully dissolved the clusters are stable against further aggregation.

In summary, we have demonstrated the proof-of-principle of a method for the preparation of colloids of physically deposited clusters. The colloids are prepared by depositing pre-formed size-controlled clusters from a cluster source onto soluble polymer films, followed by dissolution of the cluster-coated polymer films in a solvent. This has been demonstrated using different cluster materials (Au and Ag), polymers (PVP, PVA and PEG), and solvents (IPA and water). STEM measurements of the colloidal clusters revealed limited aggregation, confirming that the polymer molecules encapsulate the clusters and stabilize them against aggregation in suspension. Preliminary measurements indicate that no microstructure changes occur inside the clusters during the colloid preparation. We propose that this method can be used to prepare biocompatible colloids of ultraprecise clusters using cluster beam technology. Furthermore, we anticipate that it will be possible to functionalize the clusters by the addition of suitable agents to the polymer films.

This research has been funded by the EPSRC (Grant Reference No. EP/K006061/1) and by the European Union's Seventh Framework Programme (No. FP7/2007-2013) under Grant Agreement No. 607417 (CATSENSE).

[1] D. C. Engemann, S. Roese, and H. Hövel, J. Phys. Chem. C **120**, 6239 (2016).

[2] H. Wender, L. F. de Oliveira, A. F. Feil, E. Lissner, P. Migowski, M. R. Meneghetti, S. R. Teixeira, and J. Dupont, Chem. Commun. **46**, 7019 (2010).

[3] R. E. Palmer, L. Cao, and F. Yin, Rev. Sci. Instrum. **87**, 046103 (2016).

[4] P. R. Ellis, C. M. Brown, P. T. Bishop, J. Yin, K. Cooke, W. D. Terry, J. Liu, and R. E. Palmer, Faraday Discuss. **188**, 39 (2016).

[5] V. T. A. Oiko, T. Mathieu, L. Cao, J. Liu, and R. E. Palmer, J. Chem. Phys. **145**, 166101 (2016).

[6] B. Santiago González, M. J. Rodríguez, C. Blanco, J. Rivas, M. A. López-Quintela, and J. M. Gaspar Martinho, Nano Lett. **10**, 4217 (2010).

[7] H. Tsunoyama, H. Sakurai, N. Ichikuni, Y. Negishi, and T. Tsukuda, Langmuir **20**, 11293 (2004).

[8] H. Zhang, N. Toshima, K. Takasaki, and M. Okumura, J. Alloys Compd. **586**, 462 (2014).

[9] X. Yuan, Z. Luo, Q. Zhang, X. Zhang, Y. Zheng, J. Y. Lee, and J. Xie, ACS Nano **5**, 8800 (2011).

[10] S. Pratontep, S. J. Carroll, C. Xirouchaki, M. Streun, and R. E. Palmer, Rev. Sci. Instrum. **76**, 045103 (2005).

[11] K. J. Hu, S. R. Plant, P. R. Ellis, C. M. Brown, P. T. Bishop, and R. E. Palmer, Phys. Chem. Chem. Phys. **16**, 26631 (2014).